University of California

Santa Barbara

A novel role for free oligomeric tubulin in cross-linking tau-mediated microtubule bundles: A structural study on protein assembly states

A dissertation submitted in partial satisfaction

of the requirements for the degree

Doctor of Philosophy

In

Biochemistry and Molecular Biology

by

Bretton Jay Fletcher II

Committee in charge:

Professor Cyrus R. Safinya, Chair
Professor Stuart C. Feinstein
Professor Omar Saleh
Professor Herbert Waite

December 2023

The dissertation of Bretton Jay Fletcher II is approved.

_____

Professor Stuart C. Feinstein

_____

Professor Omar Saleh

_____

Professor Herbert Waite

_____

Professor Cyrus R. Safinya, Committee Chair

June 2023

Acknowledgments

I would like to first thank my sister Katie for all of the guidance and support she has offered throughout my life – not least for making me want to attend UCSB – and my parents, Terie, Brett, and Susan, for their unconditional love and support. I would like to especially thank my primary research advisor, Professor Cyrus Safinya, for letting me join his lab as a 19 year old physics undergraduate student. In eleven years of mentoring me, Cyrus always showed me a level of respect that I never felt I deserved. His baseline for interacting with me (and with everyone, really) was always that I was smart enough and capable enough to follow the conversation, perform the responsibilities he entrusted me with, and to just be as good of a person and scientist as he is, and anyone who knows Cyrus knows that it is a compliment to be considered in his company. I have the utmost respect for his character both as a human and mentor and for his intense curiosity about and intuition for how the squishy stuff in our universe all works. He of course provided me with helpful guidance and insight as I navigated my research and general academic career, but it always just felt like a conversation between peers, even as an undergrad and young graduate student. That subtle encouragement helped maybe more than he knows, and I am forever grateful for the opportunities that he has provided me.

The Materials Research Laboratory at UCSB and the family that it fosters also deserve special mention. The MRL became my second home in undergrad, and the relationships I have built here are ones that I will always cherish. From Dotti Pak and

Julie Standish in the outreach programs, to Mary McGuan, Fuzzy Rogers, and Sylvia Vogel in the east wing of the building. To Fyl Pincus and his full-face-licks and Angela Pitenis and Omar Saleh who lovingly put up with Fyl's visit time with Kamiya. To Ram Seshadri and the industrious "hard-materials" folks in the MRL who set the standard for style in scientific presentation. To Amanda Strom and Rachel Behrens for keeping the building together and instruments running. And to all of the graduate students who came through the MRL in my long stint with the family – everyone helped me grow and learn and persevere and I am thankful for that.

Lastly, the biggest acknowledgment must be made to my brilliant and studious and loving life partner, Dr. Becca Best, without whom I most certainly would not have completed this doctoral thesis. Becca's contributions to my research were invaluable from the beginning, when she taught me the fundamentals of biology lab best practices. She also made significant contributions by positively altering the trajectory of the big first paper that will come from this body of work, when she (somehow) convinced Cyrus that our draft manuscript needed major revisions. Not only did she do the convincing, but she also helped guide those changes with useful references and a scientific perspective that was uniquely hers. For that, her name is on the author list for the major planned publications from this work. But I think only here can I say just how much she pushed me to keep going, encouraged me to believe in myself by believing in me first and always, and provided me the much needed conversation partner to spring ideas off of any time that I needed it. Her love and commitment to me provided a foundation for me to write, edit, and finish the work that you see here. And for that I am forever grateful.

Vitae

Bretton Jay Fletcher II

Education

2023 Ph.D. in Biochemistry and Molecular Biology, University of California Santa Barbara
2015 Bachelor of Science in Physics, University of California, Santa Barbara

Professional Employment

2015 – 2023 Teaching Assistant, University of California, Santa Barbara
Molecular, Cellular, and Developmental Biology
108A – General Biochemistry
110 – Principles in Biochemistry
123 – Physical Biochemistry
153 – Developmental Neurobiology
262 – Graduate Student Colloquium
Physics
3L – Basic Physics Laboratory
2015 – 2022 Graduate Student Researcher, University of California, Santa Barbara
2021 Graduate Teaching Associate, University of California, Santa Barbara
Molecular, Cellular, and Developmental Biology
108 – General Biochemistry
2020 – 2021 Undergraduate Intern Coordinator, Materials Research Laboratory
2018 – 2020 Materials Science Ambassador, Materials Research Laboratory

Publications

In preparation "Temperature-induced, reversible phase transitions between bundled microtubule and tubulin assembly states." Fletcher, B.*; Kohl, P.*; Song, C.*; Best, R. L.; Tchounwou, C.; Chung, P. J.; Miller, H. P.; Wilson, L.; Choi, M. C.; Li, Y.; Feinstein, S. C.; Safinya, C. R. (*contributed equally)

Under revision "Complexes of tubulin oligomers and tau form a viscoelastic, intervening network cross-bridging microtubules into bundles." Fletcher, B.*; Kohl, P.*; Song, C.*; Best, R. L.; Tchounwou, C.; Arceo, X. G.; Chung, P. J.; Miller, H. P.; Wilson, L.; Choi, M. C.; Li, Y.; Feinstein, S. C.; Safinya, C. R. (*contributed equally)

2017 "Distinct solubility and cytotoxicity regimes of paclitaxel-loaded cationic liposomes at low and high drug content revealed by kinetic phase behavior and cancer cell viability studies." Steffes, V. M.; Murali, M. M.; Park, Y.; Fletcher, B. J.; Ewert, K. K.; Safinya, C. R. *Biomaterials*, 145, 242-255.

2015 "Nematic director reorientation at solid and liquid interfaces under flow: SAXS studies in a microfluidic device." Silva, B.; Zepeda-Rosales, M.; Venkateswaran, N.; Fletcher, B.; Carter, L.; Matsui, T.; Weiss, T.; Han, J.; Li, Y.; Olsson, U.; Safinya, C. R. *Langmuir*. 31, 4361-4371.

Awards

2020 *Outstanding Mentor Award*, Materials Research Laboratory
2012 – 2015 *Undergraduate Intern*, Research Internships in Science and Engineering
2014 *Undergraduate Intern*, Partnership for Research and Education in Materials

Educational Outreach

2020 – 2021	*Materials Research Laboratory* Undergraduate Intern Coordinator for all summer research internship programs
Summer, 2019	*Summer Institute in Science and Mathematics* Mentor to Marianne Arriola, Jordana Menendez, Stephanie Amujarerat, Sarah Perez Quinoz
2018 – 2019	*Future Leaders in Advanced Materials* Mentor to Jehan Kerval
2016 – 2019	*California Alliance for Minority Participation* Mentor to Ximena Garcia Arceo (2016 – 2019), Jorge Jacinto (2018 – 2019), Anaiancy Ramirez (2016 – 2017) *UC Leadership Excellence through Advanced Degrees* Mentor to Ximena Garcia Arceo (2016 – 2019)
Summer, 2018	*Summer Institute in Science and Mathematics* Mentor to Chloe Lopez, Jaqueline Lamas, Zoe Imansjah, Ashley Tayun
Summer, 2017	*Research Internships in Science and Engineering* Mentor to Justine Paul

Public Presentations

2015 – 2021	Talk, Graduate Student Colloquium, UCSB
2017 – 2020	Poster, Biophysical Society Annual Meeting
2017 – 2018	Poster, Materials Research Outreach Program, UCSB
2014	Poster, American Vacuum Society, Texas Chapter Conference

Professional Affiliations

Biophysical Society

Abstract

A novel role for free tubulin oligomers in cross-linking

tau-mediated microtubule bundles:

A structural study on protein assembly states

by

Bretton Jay Fletcher II

Microtubules are self-assembling cytoskeletal protein structures composed of tubulin dimer subunits and are ubiquitous in mammalian cells, where they serve a multitude of functions such as maintaining cellular shape, providing pathways for intracellular transport, and driving neuronal outgrowth in early development. Their ability to elongate with the addition of tubulin, shorten by peeling away individual or oligomeric subunits, and switch between these two states is called dynamic instability and provides a focal point for cellular regulation of microtubule-driven processes. Indeed, many microtubule-associated proteins (MAPs) are known to bind microtubules and alter dynamic instability by promoting or suppressing either the polymerization or depolymerization of individual microtubules. One heavily studied MAP is tau, an intrinsically disordered protein primarily localized to the axonal compartment of mature neurons. Scientific focus on the properties and function of tau stems from the discovery many decades ago of neurofibrillary tangles as a hallmark of Alzheimer's disease and, later of tau's involvement in those tangles and in several other neurodegenerative diseases. Pathological and physiological roles for tau have been studied extensively. For example, we know that different tau isoforms

are differentially expressed in development and maturity, that tau binds to and modifies microtubule dynamic instability, and that chemical alterations to tau leading to dysfunction are sufficient to induce disease-like pathology in cell cultures, animal studies, and humans.

One poorly understood tau function is its ability to mediate the phase separation and regular spacing of microtubules in string-like arrays or bundles. Such microtubule structures are found at the axon initial segment of mature neurons, where they are referred to as “fascicles,” and have been re-produced with the addition of tau in non-neuronal cell cultures and in cell-free protein experiments involving only tubulin and recombinant human tau. Interestingly, the sorting of tau to the axon has been shown to rely on the structural integrity of the AIS, including microtubules, and is dependent on binding of tau to microtubules, implying a possible link between tau-mediated microtubule bundling and the subcellular localization of tau itself. Thus, imperative to understanding the physiological relevance of tau-mediated microtubule bundling is determining the mechanism by which tau mediates inter-microtubule interactions within bundles.

Several models have been proposed, creating a dogma of tau-tau interactions driving bundling, but are incompatible with polyelectrolyte theory and the structural features of microtubule bundles, namely wall-to-wall distances between neighboring microtubules. To better understand the underlying mechanism of tau-mediated bundling, we sought to monitor the structures of microtubule bundles as a function of time in the presence of several factors or conditions we thought would alter the interactions underlying bundle formation. First, experiments were designed to probe

the electrostatic-component of tau-mediated bundling. Several tau-tau models for microtubule bundling rely on the dipole-like distribution of charge along tau's N-terminal tail, where a relative abundance of acidic residues are followed by an abundance of basic residues, providing a possible mechanism for two opposing tau molecules to overlap and favorably interact to hold adjacent microtubules together. By increasing the ionic strength of the buffers, we sought to weaken such charge-charge interactions, which would predict a decrease in bundling strength or an outright inability of tau to mediate bundle formation in high-salt buffers. Instead, our data show that wall-to-wall distances between microtubules is largely unaffected by increases in monovalent cation species. Interestingly, with the addition of excess divalent cations, Mg^{2+} or Ca^{2+}, an unexpected transformation of the hexagonal bundle lattice was observed. Specifically, we found that above threshold concentrations of either divalent cation, a phase transition is induced as a function of time or increased cation content. The phase transition is marked by the sudden and simultaneous drop in average wall-to-wall spacing, increase in lattice parameter (bundle size, or number of microtubules per bundle), and proliferation of inverted tubulin rings.

Based on these results, we propose and test a model where free tubulin oligomers participate in and are necessary for the bundling of microtubules by tau protein. In our model, tau binds to multiple species of tubulin to join together free (non-lattice-bound) tubulin oligomers and lattice-bound tubulin within microtubules. The multivalent nature of tau's interactions with various tubulin oligomers and microtubules creates a network of tubulin and tau that cross-links microtubules within bundles. Within this model, an absence or depletion of free tubulin should

prevent tau-mediated bundling, while increases to the free tubulin content should enhance bundle properties. Consistent with this model, experiments designed to induce rapid microtubule depolymerization by dropping the sample temperature reproduced the phase transitions observed in the depolymerization events induced by divalent cations. Similarly, samples prepared with increasing GTP content showed resistance to microtubule depolymerization over time, corresponding to the delay and in some cases elimination of the phase transition. Taken together, our results and the model we propose for tau-mediated microtubule bundling represent a novel role for tubulin in the bundling process. We are excited by the prospect of these new findings and their physiological relevance both to the understanding of developmental and mature tau function in human neurons but also to tau dysfunction in neurodegenerative diseases.

Table of Contents

1. Introduction

1.1. Microtubule (MT) polymerization and depolymerization

Microtubules (MTs) are hollow protein nanotubes that make up a core component of the eukaryotic cytoskeleton, performing several functions depending on their cellular and sub-cellular environment. MTs are composed of heterodimers of the globular proteins α- and β-tubulin and are formed via the head-to-tail assembly of $\alpha\beta$-tubulin dimers in the presence of GTP (Fig. 1.1). Longitudinal interactions between tubulin dimers form polar, linear tubulin oligomers and protofilaments (PFs), while lateral interactions between tubulin subunits of parallel protofilaments create protofilament sheets that curl to form cylindrical microtubules[1,2], which typically contain 13 to 15 PFs (Fig. 1.1). In conditions that favor MT growth, the slow addition of tubulin dimers or oligomers to the "growing" β-tubulin end extends the length of the MT. In conditions that favor depolymerization of MTs, constituent PFs will rapidly curl outward away from the MT body and break off into curled, oligomeric tubulin depolymerization products (Fig. 1.1)[3-5]. Depolymerization or "catastrophe" events, can lead to complete MT disassembly or, in the presence of factors promoting microtubule growth, can sometimes be halted and even "rescued" to allow the MT to re-enter a polymerization phase. This phenomenon of stochastic switching between periods of growing and shrinking is referred to as dynamic instability and is tightly regulated by cells in order to carry out specific MT functions.

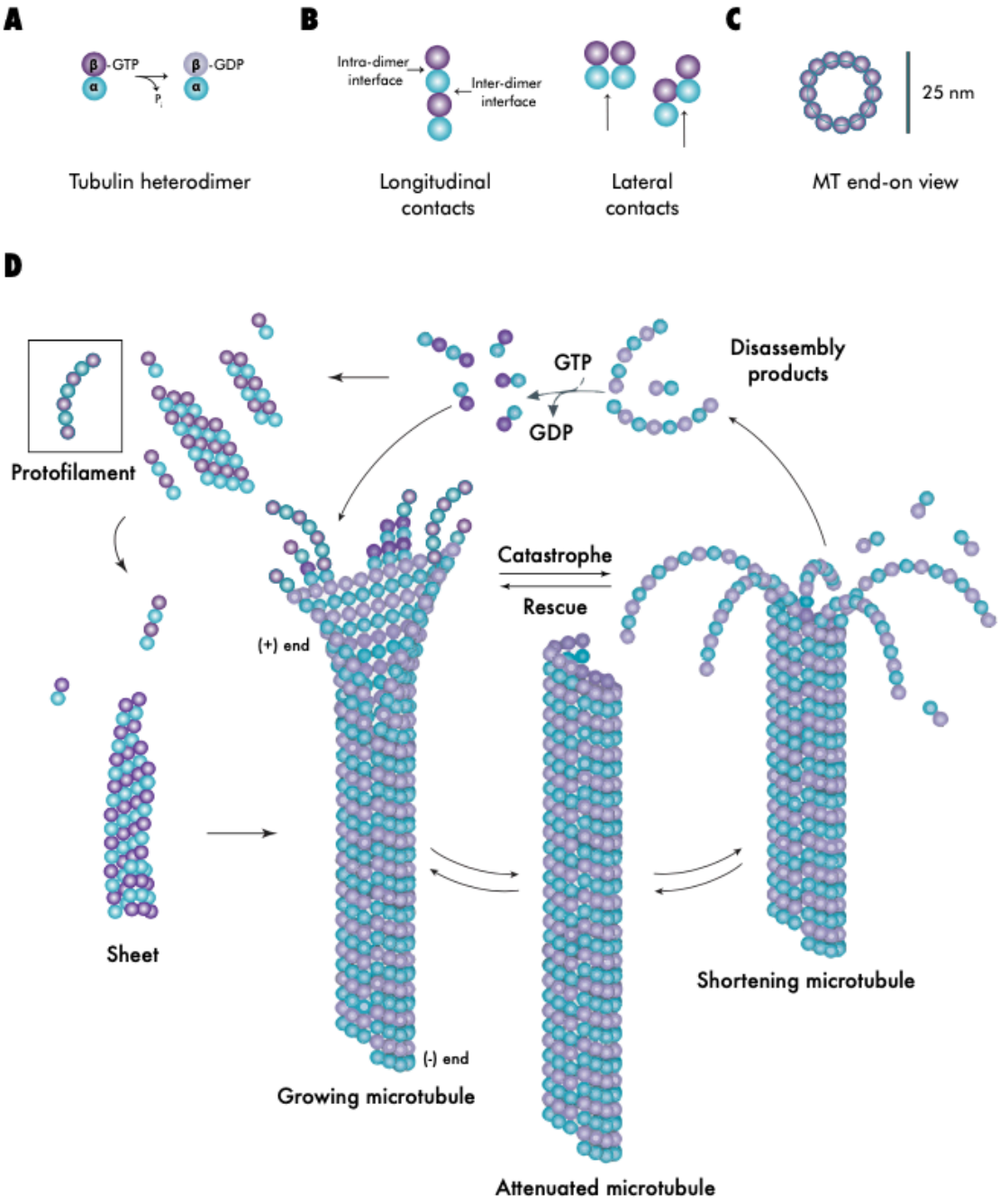

Figure 1.1: **Schematic of microtubule structure and dynamics** (A) Tubulin heterodimers can hydrolyze GTP at the exchangeable nucleotide-binding site of the β–tubulin subunit. (B) Tubulin can form polar, one-dimensional oligomers via longitudinal interactions (left) or lateral contacts between adjacent tubulin dimers can be homo- or heterotypic. (C) Cross-sectional view down the axis of a microtubule. (D) Microtubule dynamic instability and proposed tubulin conformations at each stage. Borrowed with permission from ref 6 and originally adapted from ref 7.

1.1.1. Dynamic instability

In order for MT nucleation and growth to occur[8-10], each of the α- and β-tubulin monomer subunits must be bound to a molecule of guanosine triphosphate, coordinated by a Mg^{2+} ion[11,12]. GTP in the α-tubulin subunit is stable during dynamic instability, but sometime after being incorporated into the microtubule lattice, GTP bound to the β-tubulin subunit can be hydrolyzed to form a GDP-tubulin dimer[13,14]. Free tubulin dimers (not lattice-bound) can exchange the nucleotide at the β-tubulin, typically favoring GTP over GDP in the presence of excess Mg^{2+} ion[15,16]. Thus, the nucleotide state of tubulin can be altered either via hydrolysis of GTP to GDP within the MT lattice or via nucleotide exchange in a free tubulin dimer.

Conformational differences between GTP- and GDP-tubulin are thought to drive dynamic instability[17-19], where PFs composed of GDP-tubulin more strongly favor a curled conformation compared to those of GTP-tubulin. While the specific conformational changes of the αβ-tubulin dimer upon hydrolysis of GTP are difficult to study and have been the subject of debate[5,20], most recent evidence suggests the curling of PFs arises due to bending of the α-tubulin subunit and a compaction of the longitudinal inter-dimer interface upon GTP hydrolysis[5,19,21]. Early models suggested PF curling was simply due to differences in the overall curvature of the αβ-tubulin heterodimer, where GTP- and GDP-tubulin were thought to respectively favor straight and curled conformations and impart that curvature onto the PFs they were part of[4,22,23]. However, recent studies have shown that both GTP and GDP tubulin dimers favor a curled conformation, the latter being only slightly more curled. The current

model suggests that individual PFs favor a curled conformation independent of their tubulin nucleotide state, and PF straightening arises from lateral interactions between GTP-tubulin dimers of neighboring PFs upon MT polymerization. Thus, MT catastrophe is thought to occur when the stabilizing lateral interactions between PFs are made weaker upon GTP hydrolysis, allowing the intrinsic conformational strain of individual PFs to drive the outward curling away from the MT lattice.

1.1.2. Tubulin structures during assembly and disassembly

MT polymerization is initiated with a nucleation stage and subsequently followed by a growth stage[1]. The dynamics of these two stages differ from one another and vary greatly depending on several factors such as the tubulin isoforms involved, temperature, the availability of tubulin and GTP, MT-associated proteins, and chemical agents that affect MT dynamics[9,13,24-26]. MT nucleation requires a critical concentration of GTP-tubulin and can either occur spontaneously by the formation of a new MT seed or can be templated by a pre-formed MT seed or by physiological structures such as axonemes and centrosomes. While templated MT nucleation is most common *in vivo*, many fundamental mechanisms of GTP-driven tubulin assembly and dynamic instability have been discovered by probing both templated- and non-templated nucleation *in vitro*[27].

Most recently, structural studies of tubulin in conditions promoting MT growth have revealed the dependence of nucleation on the nanostructures formed prior to MT-assembly[24,28,29]. In agreement with early work[30], these studies show that MT nucleation only occurs above an inter-dependent critical temperature and critical

tubulin concentration. Above and below critical conditions there is a coexistence of tubulin dimers, small 1-dimensional oligomers, and single rings formed from curled tubulin oligomers. The formation of MTs from these pre-MT tubulin assembly structures occurs by the addition of single tubulin dimers to growing 1-dimensional oligomers, requiring the disassembly of closed oligomer ring structures and strongly dependent on temperature and tubulin nucleotide state. Only above critical conditions is tubulin oligomer formation sufficient to form the two-dimensional sheets required for MT nucleation.

Continued growth following MT nucleation is typically discussed as it relates to the end-to-end addition of tubulin subunits onto the plus ends (terminal β-tubulin subunit) of the constituent PFs, which display more dynamic polymerization and depolymerization activity than the minus ends (terminal α-tubulin subunit)[31]. To better understand the dynamics of MT polymerization, many experiments have focused on the morphology of the growing plus end[2,4,23], where varying structures have been reported, including blunt, sheet-like ends (indicating strong lateral interactions at the ends of growing PFs) with mostly straight PFs of approximately equal length[2,22,32], tapered sheet-like ends with heterogenous PF lengths and curvatures[18,33-36], and, most recently, flared ends with independently growing PFs of individually maintained curvatures[37]. The flared growing end morphologies were observed in several species of cell lines and in cell-free experiments and were structurally indistinguishable from shortening plus-end morphologies, consistent with other reports on the curvature of GTP- and GDP-tubulin structures.

Despite mixed reports on the differences in tubulin dimer conformation in the GDP and GTP states, GDP tubulin incorporated in a MT imparts a strain on the lattice that can lead to catastrophe events[27]. Many reports have been made on high-curvature "rams horn" disassembly structures[4,22,23], consistent with the ability of curved GDP-rich tubulin and curve one-dimensional oligomers to promote the assembly of inverted tubulin rings. These tubulin rings have long been linked to the initial phases of MT polymerization[38,39], requiring ring disassembly for MT assembly, and are thought of as a storage structure for active tubulin subunits[40-42]. Indeed, below critical temperatures for MT assembly, an equilibrium of tubulin states exists that includes tubulin dimers, curled 1-D oligomers, and rings, and above critical temperatures, rings disassemble ahead of MT assembly. In addition to low temperatures, divalent cations, such as Ca^{2+} and Mg^{2+}, are also known to stabilize tubulin rings[41,43,44] and suppress MT growth above critical concentrations[45-47], despite the necessity of Mg^{2+} for GTP-tubulin binding and MT polymerization[48]. In contrast, the MT-stabilizing agent and anti-cancer chemotherapeutic paclitaxel stabilizes the straight protofilament conformation in GTP- and GDP-tubulin structures, even at 4 °C[49-52]. Many other biological and synthetic factors are known to affect the curvature and stability of tubulin structural states, and the impact these structures have on MT function provides a control point for regulation by cells. Indeed, many microtubule-associated proteins are known to alter, recognize, or preferentially bind to specific tubulin structures.

1.2. Microtubule-associated protein tau

1.2.1. Isoforms and physical characteristics of tau

MAP tau is an intrinsically disordered protein localized primarily to the axons of neurons and has been studied extensively for its ability to bind to MTs and alter dynamic instability. Humans express six wild-type isoforms of tau dependent on the splicing of exons 2, 3, and 10 of the MAPT gene[53,54]. Inclusion of either exons 2 and 3 together, exon 2 alone, or neither of the two exons determines the length (long, L; medium, M; and short, S, respectively) of the amino-terminal projection domain (PD) and the number of acidic residues the protein contains[55]. The PD is followed sequentially by a proline-rich region and microtubule binding domain (MTBD) highly enriched in basic residues, then a carboxyl-terminal tail. Inclusion or exclusion of exon 10 leads to a MTBD composed of 4 (4R) or 3 (3R) imperfect repeat sequences, respectively. Despite large anionic regions at the N- and C-termini, all six isoforms of tau exhibit a net cationic charge at physiological pH, which is thought to contribute to tau's binding to negatively charged residues on the MT surface.

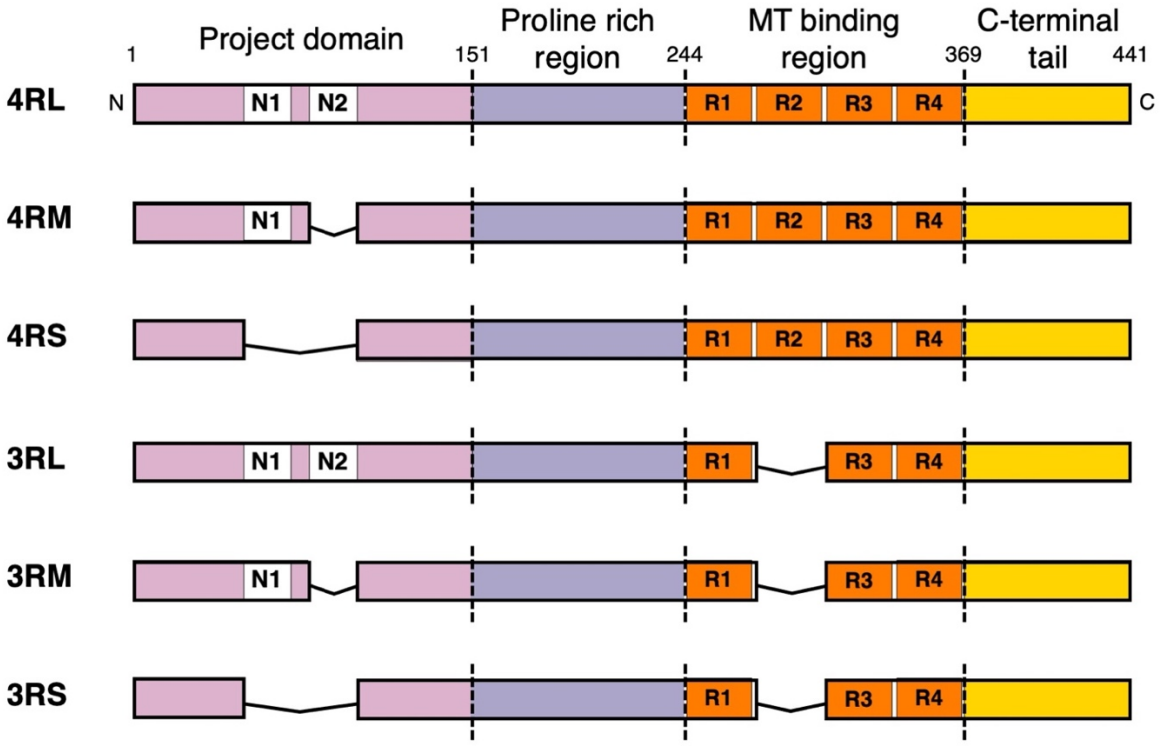

Figure 1.2: **Tau isoforms and sequence domains** The full length 4RL isoform of tau includes inserts N1 and N2 in the projection domain, followed by the proline rich region, the microtubule binding domain with 4 imperfect repeat sequences, and the C-terminal tail. 4R and 3R isoforms differ in their inclusion or exclusion of repeat 2 within the MT binding domain, respectively; whereas long (L), medium (M), and short (S) isoforms vary in their inclusion of inserts N1 and N2.

1.2.2. Regulation of dynamic instability

The historical understanding of tau's action on MTs stems from early cell-free studies of purified tubulin and tau. Tau was demonstrated to affect MT nucleation by lowering the critical concentration of tubulin needed to initiate polymerization[56] and by eliminating the need for excess Mg^{2+} (above 1:1 ion to tubulin dimer). Similarly, steady state experiments showed tau increases MT growth rate[56,57] and prolongs the time spent in a paused/attenuated growth state, thereby decreasing the frequency of catastrophe[56,58-60]. Thus, a canonical role of tau is to stabilize MTs against depolymerization.

Recent studies have called this function into question, showing that tau binds the more labile domain of dynamic microtubules and that the proportion of labile regions shifts largely in favor of stable microtubule domains in cultured rat neurons lacking tau[61]. In agreement with these findings, cell-free experiments with microtubules polymerized with the slowly-hydrolyzable GTP analog GMPCPP show that tau stabilizes distinct intermediate states of tubulin protofilaments on assembling and disassembling microtubule ends[62]. Reconciling these reports with the dogma of tau as a microtubule stabilizer, Best *et al* proposed that tau's role is to stabilize the otherwise unstable intermediate structures during assembly and disassembly by strengthening lateral interactions between adjacent protofilaments in order to help overcome barriers of nucleation, continued polymerization, or rescue from disassembly[62].

1.2.3. Tau-tubulin binding interactions

The specific binding properties between tau and microtubules has been a large focus of research efforts in tau pathology and physiology, including understanding the roles and specificity of tau's microtubule binding repeat sequences, the conformation of tau bound to microtubules, the recognition of specific tubulin structural states by tau, and the effect of chemical alterations to tau on tau-tubulin interactions. Many studies have shown a preference of tau for curved tubulin structures both separate from and part of microtubules[63-66], consistent with the increased presence of curved structures during nucleation and tau's abilities to reduce critical tubulin concentrations needed for microtubule formation and to promote tubulin ring formation from disassembling microtubules[67]. Tau's observed preference for GDP-tubulin within the MT lattice[66,68] and curled GTP-tubulin structures at the ends of microtubules, together with its proposed strengthening of both lateral and longitudinal tubulin-tubulin interactions, strongly support a model where tau stabilizes otherwise transient intermediate states during both MT assembly and disassembly in order to increase the rate of MT assembly, reduce the frequency and duration of catastrophe events, and increase the time spent in an attenuated state.

1.2.4. Involvement in microtubule bundling

In vivo studies have shown tau to be necessary for axonogenesis during development[69,70], cargo transport along the axon[71], and maintenance of neuronal polarity in mature neurons[72,73]. Recent work suggests that tau binding to MTs at the axon initial segment (AIS) plays a role in maintaining a retrograde diffusion barrier keeping tau localized to the axon[74]. These physiological tau functions occur in regions

of the axon where ordered arrays or bundles of MTs are prevalent, such as the distal region near the growth cone during development[75] and the AIS in mature neurons[74,76], where regularly spaced linear "fascicles" of MTs have been reported for decades[77-79]. However, the exact mechanisms of these functions and the role MT bundling may play are important unanswered questions that may provide insight into neurodegenerative diseases linked to tau such as Alzheimer's Disease, where tau is missorted to the soma and dendrites of diseased neurons.

While tau has long been associated with MT bundling[80,81], the role tau plays within MT bundles is controversial with a history of seemingly contradictory results and conclusions[82-84]. Seminal work with human tau and MAP2 independently expressed in insect cells showed that both MAPs induced hexagonal arrays of MTs whose wall-to-wall spacing ($D_{W\text{-}W}$) closely resembled spacings observed in fascicles of the AIS[81]. It was proposed that tau made up the crosslinks observed between bundled MTs in these and similar experiments[85-88]; however, the $D_{W\text{-}W}$ values are inconsistent with current polyelectrolyte brush theory[89] as well as solution scattering measurements of tau's radius of gyration[90].

Many early cell-free studies determined that full-length tau alone was not able to produce MT bundles, leading to the conclusion that tau may act as a repulsive brush between bundled MTs *in vivo*[83,84]. Indeed, small-angle x-ray scattering (SAXS), transmission electron microscopy (TEM), and light microscopy carried out by Choi *et al* showed a distinct lack of bundling of MTs in the presence of each of the six wild-type isoforms of tau[52], and similar experiments performed with added osmotic pressure demonstrated a tau isoform-dependent resistance to bundling below

threshold pressures[91]. Importantly, however, these experiments were performed at a 1:1 ratio of tubulin to paclitaxel, a chemotherapeutic agent that stabilizes MTs against depolymerization. A follow-up study has since shown that paclitaxel acts in a concentration-dependent manner to suppress bundling of tau-decorated MTs[92], and in the absence of paclitaxel, it was unequivocally shown that tau is able to form bundles of out-of-equilibrium, dynamic MTs that were stable for hours at 37 °C with no added osmotic pressure or crowding agents[82]. Taken together, these experiments imply that the abundance of free, unpolymerized tubulin in paclitaxel-free reaction mixtures is essential for the formation of MT bundles.

1.2.5. Tau pathology in neurodegeneration

The importance of understanding tau's roles in regulating microtubule dynamic instability and bundling stems in large part from tau's involvement in neurodegenerative diseases such as Alzheimer's. Aberrant tau function is directly related to the pathology of many dementia-related diseases, collectively referred to as tauopathies[93]. Many models have been proposed for tau's roles in these pathological pathways, including loss of function due to mutations, chemical alterations to, or differential isoform expression of tau[94,95], as well as toxic gain of function from self-aggregating tau and the formation of neurofibrillary tangles (a hallmark of Alzheimer's disease)[96,97]. While evidence exists to support both models, specific mechanisms remain elusive in part due to a fundamental lack of understanding in tau's specific roles in physiological neuronal functions. Insights into the sorting mechanism of tau[74,98], including tau-dependent binding to microtubules

at the AIS, and the role of pathological tau missorting[99] provide a hopeful pathway for connecting the results of current tau-mediated microtubule bundling experiments and future tau-based therapies.

1.3. References

1 Desai, A. & Mitchison, T. J. Microtubule polymerization dynamics. *Annu Rev Cell Dev Biol* **13**, 83-117 (1997).

2 Chretien, D., Fuller, S. D. & Karsenti, E. Structure of growing microtubule ends: two-dimensional sheets close into tubes at variable rates. *J Cell Biol* **129**, 1311-1328 (1995).

3 Hyman, A. A., Chretien, D., Arnal, I. & Wade, R. H. Structural changes accompanying GTP hydrolysis in microtubules: information from a slowly hydrolyzable analogue guanylyl-(alpha,beta)-methylene-diphosphonate. *J Cell Biol* **128**, 117-125 (1995).

4 Muller-Reichert, T., Chretien, D., Severin, F. & Hyman, A. A. Structural changes at microtubule ends accompanying GTP hydrolysis: information from a slowly hydrolyzable analogue of GTP, guanylyl (alpha,beta)methylenediphosphonate. *Proc Natl Acad Sci U S A* **95**, 3661-3666 (1998).

5 Alushin, G. M. *et al.* High-resolution microtubule structures reveal the structural transitions in alphabeta-tubulin upon GTP hydrolysis. *Cell* **157**, 1117-1129 (2014). https://doi.org:10.1016/j.cell.2014.03.053

6 Best, R. L. *Mechanistic insights into the regulation of microtubule assembly and dynamic instability by tau and MMAE*, UC Santa Barbara, (2020).

7 Conde, C. & Caceres, A. Microtubule assembly, organization and dynamics in axons and dendrites. *Nat Rev Neurosci* **10**, 319-332 (2009). https://doi.org:10.1038/nrn2631

8 Melki, R., Carlier, M. F. & Pantaloni, D. Oscillations in microtubule polymerization: the rate of GTP regeneration on tubulin controls the period. *EMBO J* **7**, 2653-2659 (1988).

9 O'Brien, E. T., Voter, W. A. & Erickson, H. P. GTP hydrolysis during microtubule assembly. *Biochemistry* **26**, 4148-4156 (1987). https://doi.org:10.1021/bi00387a061

10 Jameson, L. & Caplow, M. Effect of guanosine diphosphate on microtubule assembly and stability. *J Biol Chem* **255**, 2284-2292 (1980).

11 Weisenberg, R. C., Borisy, G. G. & Taylor, E. W. The colchicine-binding protein of mammalian brain and its relation to microtubules. *Biochemistry* **7**, 4466-4479 (1968).

12 Nogales, E., Wolf, S. G. & Downing, K. H. Structure of the alpha beta tubulin dimer by electron crystallography. *Nature* **391**, 199-203 (1998).

13 Carlier, M. F., Didry, D. & Pantaloni, D. Hydrolysis of GTP associated with the formation of tubulin oligomers is involved in microtubule nucleation. *Biophys J* **73**, 418-427 (1997). https://doi.org:10.1016/S0006-3495(97)78081-0

14 Brouhard, G. J. & Rice, L. M. Microtubule dynamics: an interplay of biochemistry and mechanics. *Nature Reviews Molecular Cell Biology* **19**, 451-463 (2018). https://doi.org:10.1038/s41580-018-0009-y

15 Zeeberg, B. & Caplow, M. Determination of free and bound microtubular protein and guanine nucleotide under equilibrium conditions. *Biochemistry* **18**, 3880-3886 (1979). https://doi.org:10.1021/bi00585a007

16 Correia, J. J., Baty, L. T. & Williams, R. C. Mg2+ dependence of guanine nucleotide binding to tubulin. *J Biol Chem* **262**, 17278-17284 (1987).

17 Coombes, C. E., Yamamoto, A., Kenzie, M. R., Odde, D. J. & Gardner, M. K. Evolving tip structures can explain age-dependent microtubule catastrophe. *Curr Biol* **23**, 1342-1348 (2013). https://doi.org:10.1016/j.cub.2013.05.059

18 VanBuren, V., Cassimeris, L. & Odde, D. J. Mechanochemical model of microtubule structure and self-assembly kinetics. *Biophys J* **89**, 2911-2926 (2005). https://doi.org:10.1529/biophysj.105.060913

19 Zhang, R., Alushin, G. M., Brown, A. & Nogales, E. Mechanistic Origin of Microtubule Dynamic Instability and Its Modulation by EB Proteins. *Cell* **162**, 849-859 (2015). https://doi.org:10.1016/j.cell.2015.07.012

20 Ayukawa, R. *et al.* GTP-dependent formation of straight tubulin oligomers leads to microtubule nucleation. *J Cell Biol* **220** (2021). https://doi.org:10.1083/jcb.202007033

21 Zhang, R., LaFrance, B. & Nogales, E. Separating the effects of nucleotide and EB binding on microtubule structure. *Proc Natl Acad Sci U S A* **115**, E6191-e6200 (2018). https://doi.org:10.1073/pnas.1802637115

22 Mandelkow, E. M., Mandelkow, E. & Milligan, R. A. Microtubule dynamics and microtubule caps: a time-resolved cryo-electron microscopy study. *J Cell Biol* **114**, 977-991 (1991).

23 Simon, J. R. & Salmon, E. D. The structure of microtubule ends during the elongation and shortening phases of dynamic instability examined by negative-stain electron microscopy. *Journal of Cell Science* **96**, 571-582 (1990).

24 Shemesh, A. *et al.* Mechanism of the Initial Tubulin Nucleation Phase. *J Phys Chem Lett* **13**, 9725-9735 (2022). https://doi.org:10.1021/acs.jpclett.2c02619

25 Campanacci, V. *et al.* Insight into microtubule nucleation from tubulin-capping proteins. *Proc Natl Acad Sci U S A* **116**, 9859-9864 (2019). https://doi.org:10.1073/pnas.1813559116

26 Brugués, J., Nuzzo, V., Mazur, E. & Needleman, D. J. Nucleation and transport organize microtubules in metaphase spindles. *Cell* **149**, 554-564 (2012). https://doi.org:10.1016/j.cell.2012.03.027

27 Voter, W. A. & Erickson, H. P. The kinetics of microtubule assembly. Evidence for a two-stage nucleation mechanism. *J Biol Chem* **259**, 10430-10438 (1984).

28 Shemesh, A., Ginsburg, A., Levi-Kalisman, Y., Ringel, I. & Raviv, U. Structure, Assembly, and Disassembly of Tubulin Single Rings. *Biochemistry* **57**, 6153-6165 (2018). https://doi.org:10.1021/acs.biochem.8b00560

29 Shemesh, A. *et al.* Structure and Energetics of GTP- and GDP-Tubulin Isodesmic Self-Association. *ACS Chem Biol* **16**, 2212-2227 (2021). https://doi.org:10.1021/acschembio.1c00369

30 Fygenson, D. K., Braun, E. & Libchaber, A. Phase diagram of microtubules. *Phys Rev E Stat Phys Plasmas Fluids Relat Interdiscip Topics* **50**, 1579-1588 (1994).

31 Atherton, J. *et al.* A structural model for microtubule minus-end recognition and protection by CAMSAP proteins. *Nature Structural & Molecular Biology* **24**, 931-943 (2017). https://doi.org:10.1038/nsmb.3483

32 Erickson, H. P. Assembly of microtubules from preformed, ring-shaped protofilaments and 6-S tubulin. *J Supramol Struct* **2**, 393-411 (1974). https://doi.org:10.1002/jss.400020228

33 Janosi, I. M., Chretien, D. & Flyvbjerg, H. Modeling elastic properties of microtubule tips and walls. *Eur Biophys J* **27**, 501-513 (1998). https://doi.org:10.1007/s002490050160

34 Guesdon, A. *et al.* EB1 interacts with outwardly curved and straight regions of the microtubule lattice. *Nat Cell Biol* **18**, 1102-1108 (2016). https://doi.org:10.1038/ncb3412

35 Wang, H. W., Long, S., Finley, K. R. & Nogales, E. Assembly of GMPCPP-bound tubulin into helical ribbons and tubes and effect of colchicine. *Cell Cycle* **4**, 1157-1160 (2005). https://doi.org:10.4161/cc.4.9.2042

36 Gardner, M. K. *et al.* Rapid microtubule self-assembly kinetics. *Cell* **146**, 582-592 (2011). https://doi.org:10.1016/j.cell.2011.06.053

37 McIntosh, J. R. *et al.* Microtubules grow by the addition of bent guanosine triphosphate tubulin to the tips of curved protofilaments. *Journal of Cell Biology* **217**, 2691-2708 (2018). https://doi.org:10.1083/jcb.201802138

38 Diaz, J. F., Andreu, J. M., Diakun, G., Towns-Andrews, E. & Bordas, J. Structural intermediates in the assembly of taxoid-induced microtubules and GDP-tubulin double rings: time-resolved X-ray scattering. *Biophys J* **70**, 2408-2420 (1996). https://doi.org:10.1016/S0006-3495(96)79809-0

39 Spann, U., Renner, W., Mandelkow, E. M., Bordas, J. & Mandelkow, E. Tubulin oligomers and microtubule assembly studied by time-resolved X-ray scattering: separation of prenucleation and nucleation events. *Biochemistry* **26**, 1123-1132 (1987). https://doi.org:10.1021/bi00378a021

40 Nogales, E., Wang, H.-W. & Niederstrasser, H. Tubulin rings: which way do they curve? *Current Opinion in Structural Biology* **13**, 256-261 (2003). https://doi.org:https://doi.org/10.1016/S0959-440X(03)00029-0

41 Howard, W. D. & Timasheff, S. N. GDP state of tubulin: stabilization of double rings. *Biochemistry* **25**, 8292-8300 (1986). https://doi.org:10.1021/bi00373a025

42 Weisenberg, R. C., Deery, W. J. & Dickinson, P. J. Tubulin-nucleotide interactions during the polymerization and depolymerization of microtubules. *Biochemistry* **15**, 4248-4254 (1976). https://doi.org:10.1021/bi00664a018

43 Nicholson, W. V., Lee, M., Downing, K. H. & Nogales, E. Cryo-electron microscopy of GDP-tubulin rings. *Cell Biochem Biophys* **31**, 175-183 (1999). https://doi.org:10.1007/bf02738171

44 Borisy, G. G. & Olmsted, J. B. Nucleated assembly of microtubules in porcine brain extracts. *Science* **177**, 1196-1197 (1972). https://doi.org:10.1126/science.177.4055.1196

45 Weisenberg, R. C. Microtubule formation in vitro in solutions containing low calcium concentrations. *Science* **177**, 1104-1105 (1972). https://doi.org:10.1126/science.177.4054.1104

46 Gal, V., Martin, S. & Bayley, P. Fast disassembly of microtubules induced by Mg2+ or Ca2+. *Biochem Biophys Res Commun* **155**, 1464-1470 (1988). https://doi.org:10.1016/s0006-291x(88)81306-8

47 O'Brien, E. T., Salmon, E. D., Walker, R. A. & Erickson, H. P. Effects of magnesium on the dynamic instability of individual microtubules. *Biochemistry* **29**, 6648-6656 (1990). https://doi.org:10.1021/bi00480a014

48 Frigon, R. P. & Timasheff, S. N. Magnesium-induced self-association of calf brain tubulin. I. Stoichiometry. *Biochemistry* **14**, 4559-4566 (1975). https://doi.org:10.1021/bi00692a001

49 Nogales, E., Wolf, S. G., Khan, I. A., Luduena, R. F. & Downing, K. H. Structure of tubulin at 6.5 A and location of the taxol-binding site. *Nature* **375**, 424-427 (1995).

50 Jordan, M. A. & Wilson, L. Microtubules as a target for anticancer drugs. *Nat Rev Cancer* **4**, 253-265 (2004).

51 Elie-Caille, C. *et al.* Straight GDP-Tubulin Protofilaments Form in the Presence of Taxol. *Current Biology* **17**, 1765-1770 (2007). https://doi.org:10.1016/j.cub.2007.08.063

52 Choi, M. C. *et al.* Human microtubule-associated-protein tau regulates the number of protofilaments in microtubules: a synchrotron x-ray scattering study. *Biophys J* **97**, 519-527 (2009). https://doi.org:S0006-3495(09)00953-9 [pii] 10.1016/j.bpj.2009.04.047

53 Goedert, M., Spillantini, M. G., Jakes, R., Rutherford, D. & Crowther, R. A. Multiple isoforms of human microtubule-associated protein tau: sequences and localization in neurofibrillary tangles of Alzheimer's disease. *Neuron* **3**, 519-526 (1989).

54 Himmler, A. Structure of the bovine tau gene: alternatively spliced transcripts generate a protein family. *Mol Cell Biol* **9**, 1389-1396 (1989).

55 Goedert, M. & Jakes, R. Expression of separate isoforms of human tau protein: correlation with the tau pattern in brain and effects on tubulin polymerization. *Embo J* **9**, 4225-4230 (1990).

56 Panda, D., Samuel, J. C., Massie, M., Feinstein, S. C. & Wilson, L. Differential regulation of microtubule dynamics by three- and four-repeat tau: implications for the onset of neurodegenerative disease. *Proc Natl Acad Sci U S A* **100**, 9548-9553 (2003). https://doi.org:10.1073/pnas.1633508100

57 Drechsel, D. N., Hyman, A. A., Cobb, M. H. & Kirschner, M. W. Modulation of the dynamic instability of tubulin assembly by the microtubule-associated protein tau. *Mol Biol Cell* **3**, 1141-1154 (1992).

58 Panda, D., Goode, B. L., Feinstein, S. C. & Wilson, L. Kinetic stabilization of microtubule dynamics at steady state by tau and microtubule-binding domains of tau. *Biochemistry* **34**, 11117-11127 (1995).

59 Bunker, J. M., Wilson, L., Jordan, M. A. & Feinstein, S. C. Modulation of microtubule dynamics by tau in living cells: implications for development and neurodegeneration. *Mol Biol Cell* **15**, 2720-2728 (2004).

60 Trinczek, B., Biernat, J., Baumann, K., Mandelkow, E. M. & Mandelkow, E. Domains of tau protein, differential phosphorylation, and dynamic instability of microtubules. *Mol Biol Cell* **6**, 1887-1902 (1995).

61 Qiang, L. *et al.* Tau Does Not Stabilize Axonal Microtubules but Rather Enables Them to Have Long Labile Domains. *Current Biology* **28**, 2181-2189.e2184 (2018). https://doi.org:https://doi.org/10.1016/j.cub.2018.05.045

62 Best, R. L. *et al.* Tau isoform-specific stabilization of intermediate states during microtubule assembly and disassembly. *J Biol Chem* **294**, 12265-12280 (2019). https://doi.org:10.1074/jbc.RA119.009124

63 Samsonov. Tau interaction with microtubules in vivo. *Journal of Cell Science* (2004).

64 Breuzard, G. *et al.* Molecular mechanisms of Tau binding to microtubules and its role in microtubule dynamics in live cells. *J Cell Sci* **126**, 2810-2819 (2013). https://doi.org:10.1242/jcs.120832
65 Tan, R. *et al.* Microtubules gate tau condensation to spatially regulate microtubule functions. *Nat Cell Biol* **21**, 1078-1085 (2019). https://doi.org:10.1038/s41556-019-0375-5
66 Duan, A. R. *et al.* Interactions between Tau and Different Conformations of Tubulin: Implications for Tau Function and Mechanism. *J Mol Biol* **429**, 1424-1438 (2017). https://doi.org:10.1016/j.jmb.2017.03.018
67 Kirschner, M. W., Williams, R. C., Weingarten, M. & Gerhart, J. C. Microtubules from mammalian brain: some properties of their depolymerization products and a proposed mechanism of assembly and disassembly. *Proc Natl Acad Sci U S A* **71**, 1159-1163 (1974).
68 Castle, B. T., McKibben, K. M., Rhoades, E. & Odde, D. J. Tau avoids the GTP cap at growing microtubule plus ends. *bioRxiv*, 2019.2012.2031.891234 (2020). https://doi.org:10.1101/2019.12.31.891234
69 Drubin, D. G., Feinstein, S. C., Shooter, E. M. & Kirschner, M. W. Nerve growth factor-induced neurite outgrowth in PC12 cells involves the coordinate induction of microtubule assembly and assembly-promoting factors. *J Cell Biol* **101**, 1799-1807 (1985).
70 Drubin, D., Kobayashi, S. & Kirschner, M. Association of tau protein with microtubules in living cells. *Ann N Y Acad Sci* **466**, 257-268 (1986).
71 Sato-Harada, R., Okabe, S., Umeyama, T., Kanai, Y. & Hirokawa, N. Microtubule-associated proteins regulate microtubule function as the track for intracellular membrane organelle transports. *Cell Struct Funct* **21**, 283-295 (1996).
72 Caceres, A. & Kosik, K. S. Inhibition of neurite polarity by tau antisense oligonucleotides in primary cerebellar neurons. *Nature* **343**, 461-463 (1990).
73 Caceres, A., Potrebic, S. & Kosik, K. S. The effect of tau antisense oligonucleotides on neurite formation of cultured cerebellar macroneurons. *J Neurosci* **11**, 1515-1523 (1991).
74 Li, X. *et al.* Novel diffusion barrier for axonal retention of Tau in neurons and its failure in neurodegeneration. *EMBO J* **30**, 4825-4837 (2011). https://doi.org:10.1038/emboj.2011.376
75 Kempf, M., Clement, A., Faissner, A., Lee, G. & Brandt, R. Tau binds to the distal axon early in development of polarity in a microtubule- and microfilament-dependent manner. *J Neurosci* **16**, 5583-5592 (1996).
76 Xia, D., Gutmann, J. M. & Götz, J. Mobility and subcellular localization of endogenous, gene-edited Tau differs from that of over-expressed human wild-type and P301L mutant Tau. *Sci Rep* **6**, 29074 (2016). https://doi.org:10.1038/srep29074
77 Palay, S. L., Sotelo, C., Peters, A. & Orkand, P. M. The axon hillock and the initial segment. *J Cell Biol* **38**, 193-201 (1968). https://doi.org:10.1083/jcb.38.1.193

78 Peters, A., Palay, S. L. & Webster, H. d. F. (Oxford University Press, 1991).
79 Rasband, M. N. The axon initial segment and the maintenance of neuronal polarity. *Nat Rev Neurosci* **11**, 552-562 (2010). https://doi.org:10.1038/nrn2852
80 Frappier, T. F., Georgieff, I. S., Brown, K. & Shelanski, M. L. tau Regulation of microtubule-microtubule spacing and bundling. *J Neurochem* **63**, 2288-2294 (1994).
81 Chen, J., Kanai, Y., Cowan, N. J. & Hirokawa, N. Projection domains of MAP2 and tau determine spacings between microtubules in dendrites and axons. *Nature* **360**, 674-677 (1992). https://doi.org:10.1038/360674a0
82 Chung, P. J. *et al.* Tau mediates microtubule bundle architectures mimicking fascicles of microtubules found in the axon initial segment. *Nat Commun* **7**, 12278 (2016). https://doi.org:10.1038/ncomms12278
83 Gustke, N., Trinczek, B., Biernat, J., Mandelkow, E. M. & Mandelkow, E. Domains of Tau-Protein and Interactions with Microtubules. *Biochemistry* **33**, 9511-9522 (1994).
84 Brandt, R. & Lee, G. Orientation, assembly, and stability of microtubule bundles induced by a fragment of tau protein. *Cell Motil Cytoskeleton* **28**, 143-154 (1994).
85 Hirokawa, N., Hisanaga, S. & Shiomura, Y. MAP2 is a component of crossbridges between microtubules and neurofilaments in the neuronal cytoskeleton: quick-freeze, deep-etch immunoelectron microscopy and reconstitution studies. *J Neurosci* **8**, 2769-2779 (1988).
86 Rosenberg, K. J., Ross, J. L., Feinstein, H. E., Feinstein, S. C. & Israelachvili, J. Complementary dimerization of microtubule-associated tau protein: Implications for microtubule bundling and tau-mediated pathogenesis. *Proc Natl Acad Sci U S A* **105**, 7445-7450 (2008). https://doi.org:10.1073/pnas.0802036105
87 Harada, A. *et al.* Altered microtubule organization in small-calibre axons of mice lacking tau protein. *Nature* **369**, 488-491 (1994).
88 Kanai, Y., Chen, J. & Hirokawa, N. Microtubule bundling by tau proteins in vivo: analysis of functional domains. *Embo J* **11**, 3953-3961 (1992).
89 Rubinstein, M. & Colby, R. H. *Polymer physics*. Vol. 23 (Oxford university press New York, 2003).
90 Mylonas, E. *et al.* Domain conformation of tau protein studied by solution small-angle X-ray scattering. *Biochemistry* **47**, 10345-10353 (2008). https://doi.org:10.1021/bi800900d
91 Chung, P. J. *et al.* Direct force measurements reveal that protein Tau confers short-range attractions and isoform-dependent steric stabilization to microtubules. *Proc Natl Acad Sci U S A* **112**, E6416-6425 (2015). https://doi.org:10.1073/pnas.1513172112
92 Choi, M. C. *et al.* Paclitaxel suppresses Tau-mediated microtubule bundling in a concentration-dependent manner. *Biochim Biophys Acta Gen Subj* **1861**, 3456-3463 (2017). https://doi.org:10.1016/j.bbagen.2016.09.011

93 Lee, V. M., Goedert, M. & Trojanowski, J. Q. Neurodegenerative tauopathies. *Annual Review of Neuroscience* **24**, 1121-1159 (2001).
94 Brunden, K. R., Trojanowski, J. Q. & Lee, V. M. Advances in tau-focused drug discovery for Alzheimer's disease and related tauopathies. *Nature Reviews Drug Discovery* **8**, 783-793 (2009). https://doi.org:nrd2959 [pii] 10.1038/nrd2959
95 Brunden, K. R. *et al.* Epothilone D improves microtubule density, axonal integrity, and cognition in a transgenic mouse model of tauopathy. *J Neurosci* **30**, 13861-13866 (2010). https://doi.org:10.1523/jneurosci.3059-10.2010
96 Vossel, K. A. *et al.* Tau reduction prevents Abeta-induced defects in axonal transport. *Science* **330**, 198 (2010). https://doi.org:10.1126/science.1194653
97 Vossel, K. A. *et al.* Tau reduction prevents Abeta-induced axonal transport deficits by blocking activation of GSK3beta. *J Cell Biol* **209**, 419-433 (2015). https://doi.org:10.1083/jcb.201407065
98 Zempel, H. & Mandelkow, E. Mechanisms of Axonal Sorting of Tau and Influence of the Axon Initial Segment on Tau Cell Polarity. *Adv Exp Med Biol* **1184**, 69-77 (2019). https://doi.org:10.1007/978-981-32-9358-8_6
99 Zempel, H. & Mandelkow, E. Lost after translation: missorting of Tau protein and consequences for Alzheimer disease. *Trends Neurosci* **37**, 721-732 (2014). https://doi.org:10.1016/j.tins.2014.08.004

2. Experimental Procedures

2.1. Expression and isolation of recombinant tau

2.1.1. Permission and attributions

The content of chapter 2 is intended to act as a resource for anyone who would wish to replicate or build upon the work presented in this thesis. Credit must be given to the scientists who came before me to develop these techniques, which have now been used, published, and iterated on by many labs. Specific credit for developing our tau purification method belongs to members of the labs of Professors Stu Feinstein and Les Wilson, including Dr. Nikki LaPointe, April Savage, Dr. Sarah Benbow, and Dr. Becca Best, as well as Dr. Peter Chung of Professor Cyrus Safinya's lab. I learned tau purification from them and from Dr. Chaeyeon Song, of Cyrus's group, and the complete protocol appears in the ref [100]. I reproduce it hear as the general procedure that I followed after taking notes and learning from those I have already mentioned.

2.1.2. Isolation of untagged tau protein

To summarize, tau is expressed in BL21(DE3) E. coli cells by transforming them with a cDNA plasmid containing the desired human tau isoform, a lac operator, ampicillin resistance (AmpR), and a T7 promoter. Agar plates containing Luria Broth (LB) and ampicillin (Amp) sodium salt are streaked on one half of the plate with transformed cells and on the other half with control cells (lacking AmpR) transformed with pUC19 plasmid. A single cell colony is selected and transferred to a flask

containing LB and Amp, which is incubated for 18 hours in a shaker at 37 °C. Following incubation, the 18-hour culture media is divided evenly into six flasks of auto-induction media (AIM) containing Amp and lactose (to induce plasmid expression), and the bacteria are incubated in a shaker at 37 °C for 24 hours.

Auto-induced bacteria are harvested by transferring AIM cultures into six centrifuge tubes, collecting two flasks at a time, and pelleting the bacteria in a RC-5 centrifuge at 4 °C for 15 minutes. Supernatants are discarded and the process is repeated for the remaining flasks. Once all bacteria are pelleted, they are resuspended and pooled together in ice-cold BRB80 buffer containing the reducing agent B-mercaptoethanol (BME) and the protease inhibitor 4-(2-Aminoethyl)benzenesulfonyl fluoride hydrochloride (AEBSF).

Resuspended bacteria pellets are subsequently lysed by French Press by loading them into the sample chamber of the pre-chilled pressure cell and pressed through while maintaining a steady flow and pressure (around 1200 psi). This process is repeated three times to generate the cell lysate, and the lysate is subsequently incubated in a water bath at 90 °C for 10 minutes in order to denature heat-labile proteins. Following heat-treatment, the cell lysate is transferred to centrifuge tubes and unwanted cell debris is pelleted at 20,200 x g for 40 minutes at 4 °C. The supernatant is collected into conical tubes, and pellets are discarded.

A phosphocellulose column is prepared for ion-exchange chromatography by adding dry phosphocellulose resin to a glass beaker, cycling the pH, and pouring the resin into a clean column. To cycle the pH of the resin, NaOH is poured into the beaker and mixed thoroughly. Waiting five minutes for the resin to settle, NaOH and

any fines of the phosphocellulose resin remaining in suspension are gently poured off. The resin is then mixed with sodium phosphate buffer, and the fines are poured off again by repeating the same rinse process. The mix and rinse process is repeated again, once with HCl, twice more with sequential rinses of sodium phosphate buffer, and then twice more with sequential rinses of BRB80. Once equilibrated with BRB80, the phosphocellulose resin is mixed with the post-boil, post-spin, tau-containing supernatant and transferred to conical centrifuge tubes. BME and AEBSF are added to the mixture, the conical tubes are placed onto a rotator for 30 minutes to mix, allowing tau to bind to the phosphocellulose resin.

The tau-resin mixture is then gently added into an empty glass column and allowed to settle for one hour. Once the column bed is settled, the column is allowed to run via peristaltic pump into a collection reservoir. The column is sequentially run by flowing through BRB80 containing (1) no added ammonium sulfate (two column volumes), (2) 50 mM ammonium sulfate (two column volumes), (3) 150 mM ammonium sulfate (four column volumes), and (4) 250 mM ammonium sulfate (two column volumes). Fractions are collected in half-column volumes, and fractions containing tau are found via SDS-PAGE.

Tau-containing fractions are subsequently pooled and brought to 1.1 M ammonium sulfate, then loaded at a rate of 1 mL per minute onto a hydrophobic-interaction column (HIC, HiTrap Phenyl HP, 5 mL column from General Electric, now Cytiva) equilibrated to 1.1 M ammonium sulfate in BRB80 (Buffer A, high salt). Using the same flow rate throughout, the column is subsequently washed with ten column volumes of Buffer A, and a program is run on the FPLC to increase the content of

BRB80 (low salt) from 0 to 60 % over 100 minutes and then from 60 to 100 % over 10 minutes, collecting fractions every 90 seconds. Fractions containing purified tau are found by SDS-PAGE, then pooled, concentrated, and buffer exchanged into BRB80 by centrifuging at 3,300 x g at 4 °C, using conical centrifuge concentrators with 10,000 molecular-weight filters (Amicon Ultra 10,000 MWCO). The total dilution factor for ammonium sulfate is kept at > 10,000 and requires several rounds of centrifugation, with gentle mixing of tau in the concentrator between each step. Finally, tau is collected from the concentrators by adding BRB80 to the concentrator for a final volume of 500 μL or less, then rinsing the filter walls to resuspend the protein and transferring the total volume to a sterile tube for storage at – 80 °C.

2.1.3. Determination of Tau concentration

Due to inconsistencies in quantifying tau protein using Bradford analysis and light absorption at 280 nm, likely due to the lack of hydrophobic and aromatic residues in tau's amino acid sequence, respectively, a quantitative SDS-PAGE method has been adopted. The quantification method relies on a comparison of the purified protein solution of unknown concentration to a standard tau solution of known concentration. Side-by-side dilution series of the two protein solutions are created and run together via SDS-PAGE, stained using Coomassie Brilliant Blue R, de-stained overnight, and then scanned using the 700 nm channel of an infrared scanner.

The intensity of each protein band on the gel is determined by measuring the total intensity inside a box drawn large enough to fit the largest protein band. The

total intensity measurements of the standard protein solution are used to generate a standard curve of intensity versus mass of protein added to each lane in the gel. The total intensity measurements of the unknown protein solution are then used to interpolate the mass of protein added to each lane of unknown protein, and the starting concentration is then back-calculated using the dilution volumes for each lane.

Once the concentration is determined for the protein solution, a new dilution series is created to match the dilution series of the standard protein solution, and a new gel is run and quantified as described to confirm the back-calculated concentration.

2.2. Sample preparation

2.2.1. Reaction mixtures

Due to the long duration of most experiments presented here, reaction mixtures were typically prepared in batches of about 14 samples each and tested together. Each batch of samples is therefore internally consistent in terms of the batch and purification date proteins used, the final concentrations of tubulin and tau, the downtime between steps, and any other external factors that were out of our control. Additionally, we tried to control for these factors for each set of experiments, which could include several batches of samples, and any result that we compare to another comes from the same set of experiments or is explicitly discussed for the possibility of batch-dependent variations.

It is important to address the potential confusion surrounding divalent cation content in these experiments for two reasons. The first is that both BRB80 and PEM50 contain 1.0 mM Mg^{2+} ions in the form of $MgSO_4$ and $MgCl_2$, respectively. The second is that both buffers also contain the Ca^{2+} ion chelating agent, EGTA. The labeling of divalent cation concentration does not account for either the standard Mg^{2+} ion content or the standard chelating agent concentration but instead only describes the amount of ion added in addition to the standard content of the buffer. In other words, a sample prepared with 1.0 mM $MgCl_2$ added to the buffer contains 1.0 mM Mg^{2+} ion from the standard buffer, another 1.0 mM Mg^{2+} ion added (total 2.0 mM Mg^{2+} ion), as well as the 1.0 mM EGTA. The same is true for samples prepared with Ca^{2+} ion content added.

Reaction mixtures were prepared on ice by diluting a small volume of purified tubulin into PIPES polymerization buffer (PEM50), homogenizing the solution by gently stirring and triturating, and then sequentially adding small volumes of GTP in PEM50, purified tau (in BRB80), and (in a sample-specific manner) excess divalent cation dissolved in PEM50. Final reaction mixtures contained approximately 4.0 mg/mL tubulin protein in 50 μL of buffer and were exactly consistent within any set of samples created. Reaction mixtures were transferred from ice to a 37 °C water and allowed to incubate at 37 °C for 30 minutes in order to reach a steady state of microtubule dynamic instability before prepared for experimentation (Fig. 2.1, steps 1 and 2).

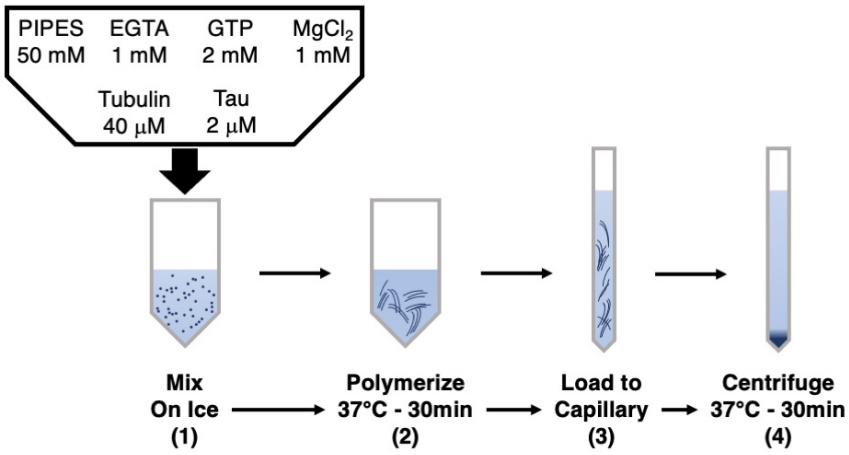

Figure 2.1 **Sample preparation schematic** Graphical outline of steps in the preparation of samples for SAXS, including buffer components and protein concentrations in standard conditions.

2.2.2. Small-angle x-ray scattering (SAXS)

In order to form protein-dense pellets suitable for high-resolution SAXS, polymerized reaction mixtures were directly loaded into 1.5 mm diameter quartz capillaries via micropipette (Fig. 2.1, step 3). The sample volume was forced to the bottom of the capillary by quickly "flicking" the capillary in a circular motion. The wide-mouth tops of the capillaries were then cut with a ceramic blade and discarded, and the remaining sample-containing capillary was loaded into a pre-warmed capillary rotor and centrifuged for 30 minutes at 9,500 x g at 37 °C (Fig. 2.1, step 4). Pelleted capillaries were sealed using a 5-minute epoxy resin and transferred into a custom made capillary holder pre-incubated at 37 °C. The capillary holder was inserted into a custom-made temperature-controlled oven with high x-ray transmittance windows made of Kapton.

2.2.3. Whole mount transmission electron microscopy (TEM)

In order to visualize the microscopic landscape of our protein reaction mixtures using real-space imaging techniques, we apply the contents of our reaction mixtures directly onto highly stable Formvar carbon-coated copper grids for whole-mount transmission electron microscopy. The protein density in the reaction mixtures we tailored for SAXS is too high to produce useful fields of view in whole mount TEM, though, so we dilute the reaction mixtures into warm buffer from roughly 4.0 mg/mL to 0.2 mg/mL of tubulin. Diluted reaction mixtures are then pipetted directly onto the copper grids and allowed to settle for two minutes before excess buffer is wicked off using filter paper. 1 % uranyl acetate in water is then added to stain the sample and subsequently wicked off after twenty seconds,

followed by rinsing excess stain and sample off by several rounds of adding and removing filtered water from the grids. Grids dried at room temperature at least overnight before imaging.

2.2.4. Plastic-embedded TEM

TEM can also be used on thin sections of fixed and stained reaction mixtures to provide cross-sectional angles in addition to the top-down visualizations provided by whole-mount techniques. To fix our samples in a state most similar to what is probed using SAXS, reaction mixtures are centrifuged at 9,500 x g at 37 °C for 30 minutes, directly following the 30-minute polymerization period. The supernatant is removed and replaced with PEM50 containing 2 % glutaraldehyde and 0.3 % tannic acid, which react with the proteins overnight to crosslink and fix the protein structures and prime the sample for subsequent staining. Cross-linked are then stained with 0.8 % osmium tetroxide in PEM50 buffer after decanting the glutaraldehyde-tannic acid solution and gently rinsing the samples with PEM50 to remove excess fixing agent. The osmium tetroxide solution is allowed to react with the fixed sample pellet for one hour, then subsequently decanted and followed by PEM50 rinse again. The sample is then stained in a similar manner by adding 1 % uranyl acetate in water for one hour and followed by a rinse step with water. Fixed and stained sample pellets are then dehydrated using acetone by successively incubating in 25, 50, and 75 % acetone solutions in water for 15 minutes each, then followed by three similar incubations in 100 % acetone.

The epoxy-based low viscosity embedding media is created by mixing 5 g of ERL 4221 (3,4 Epoxy Cyclohexyl Methyl 3,4 epoxy Cyclohexyl Carboxylate), 4 g of

D.E.R. 736 (diglycidyl ether of propylene glycol), 13 g of NSA (nonenyl succinic anhydride), 0.2 g of EASE (PolyCute-Ease), and 0.2 g of DMAE (dimethylaminoethanol). ERL 4221 is used as the primary epoxy resin, D.E.R. is a flexibilizer, NSA is a hardener, DMAE accelerates the curing time, and EASE is an anti-friction additive used to improve the sectioning of the final embedded sample. Once these components are all mixed and homogenized to make a 100 % plastic solution, 33 % and 66 % dilutions are made in acetone and used to accelerate plastic infiltration of the pellets. Following acetone decantation from the newly stained pellets, 33 % plastic solution is added to the sample tubes and allowed to mix for one hour on a tabletop shaker. The 33 % plastic solution is decanted and replaced with 66 % plastic and allowed to mix on the shaker for another hour. The 66 % plastic is then replaced with 100 % plastic, and samples are allowed to mix again for an hour while shaking, followed by a final 100 % mixture being added and allowed to shake overnight. Following the overnight plastic infiltration step, the plastic solution is decanted from the sample tube and the fixed, stained, dehydrated, and plastic-infiltrated pellet is gently scraped into flat embedding mould templates containing 100 % plastic solution and allowed to cure at 65 °C for 48 hours. Cured plastic-embedded samples are cooled overnight prior to sectioning, subsequently cut to ~ 50 nm sections with a microtome, and transferred to Formvar carbon-coated copper grids.

2.3. SAXS analysis

Solution small-angle x-ray scattering is ideal for studying the structures and phase behavior of bundled microtubules due to its ability to nonintrusively probe structural features of biological macromolecules, including the MT wall-to-wall spacing, MT diameter, and MT wall thickness, with angstrom-level resolution *in situ*. As described above, reaction mixtures are prepared and loaded into quartz capillary tubes designed to minimize scattering from the tube itself. Capillaries are placed in a sample holder between an x-ray source and a two-dimensional detector, and x-ray photons passing through our sample are able to elastically scatter off electrons within our system, creating a two-dimensional scattering pattern on our detector. The scattering intensity detector image is subsequently reduced to a 1-dimensional scattering intensity profile, plotted as a function of the scattering vector, q, which is the difference between the initial momentum of the incident wave vector and the final momentum of the scattered wave vector, as depicted in Fig. 2.2.

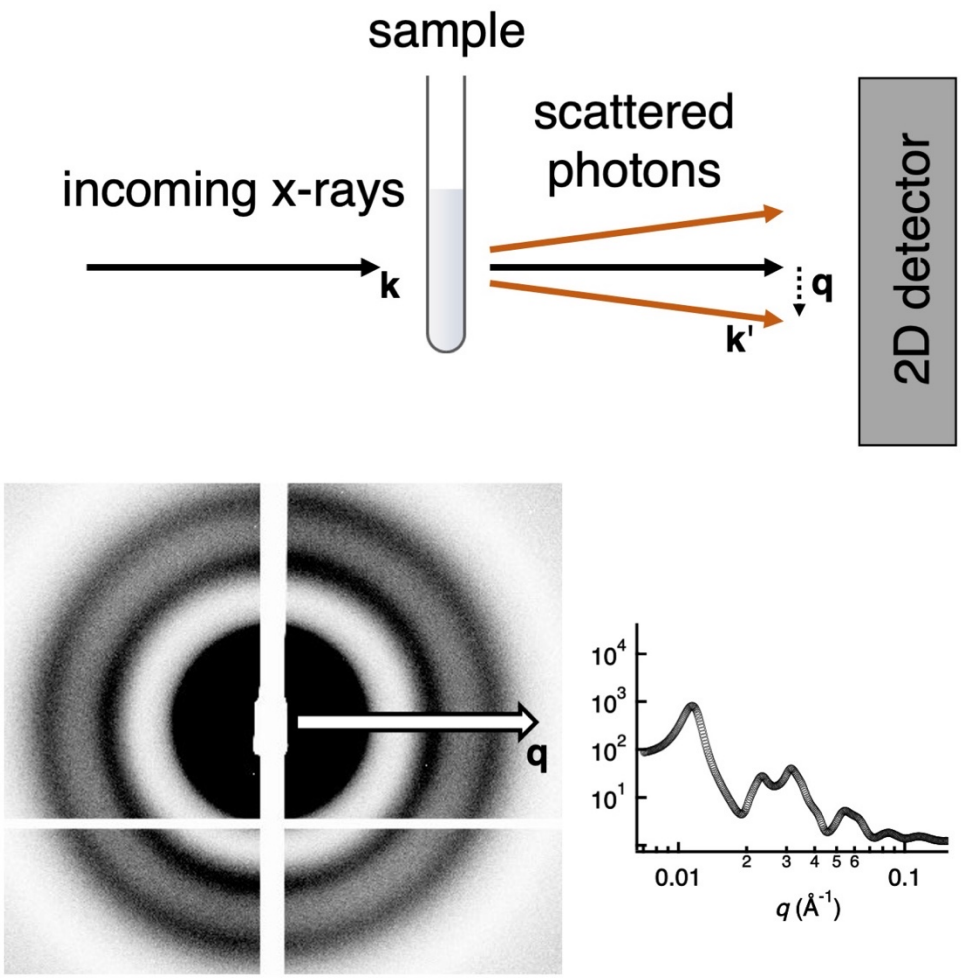

Figure 2.2: **X-ray scattering schematic and intensity profile** (Top) Incoming x-ray photons with momentum **k** pass through a sample and exit with momentum **k'**. Scattered data is collected on a 2-dimensional x-ray detector. (Bottom) 2-D scattering patterns (left) are azimuthally averaged and plotted as 1-D dimensional scattering profiles (right) as a function of the absolute value of the scattering vector **q**. Adapted with permission from Emily Wonder.

2.3.1. Scattering form factor and structure factor

The scattering intensity profile for a sample is determined by the shape of the scattering objects (the form factor) and the ordered arrangement (structure factor) of scattering objects within the sample. The intensity of scattered light contributed by the shape of the scattering object is a result of the form factor, F(Q) for that scattering object, which is mathematically determined by the Fourier transform of the electron density $\rho(r)$ for the object. For a collection of independent objects, such as a dilute solution of MTs, scattering intensity, I, is a function of the scattering vector, Q: $I(Q) = F(Q)F(Q)^* = |F(Q)|^2$. This relationship allows us to compare experimental scattering intensity to theoretical intensity curves for a given shape or set of shapes, iteratively refine the model we use, and determine precise structural information about our experimental scattering objects, such as dimensions of the cylindrical MTs. Following previous work[82,91,101-103], the microtubule structure is approximated as a long (L_{MT} > 1,000 nm, beyond the resolution of SAXS), hollow cylinder with a wall thickness, w, equal to the width of a single protofilament, uniform electron density ρ_0, and variable inner radius r_{in}, that is used as a fit parameter. To account for the presence of tubulin rings in our samples, a similar model of a hollow cylinder with the same electron density and wall thickness, and variable inner radius is used; however, the cylinder length, L_{Ring}, is reduced to the width of one tubulin dimer. Thus, the form factor for microtubules (F_{MT}) and rings (F_{Ring}) are written as follows:

$$|F_{MT}|^2 \propto \left| \left[(\sin(q_z L_{MT}/2)/q_r q_z)\right]\left[(r_{in}+w)J_1\left(q_r(r_{in}+w)\right) - r_{in}J_1(q_r r_{in})\right] \right|^2 \quad (\mathbf{1})$$

$$\left|F_{Ring}\right|^2 = \left| A_{ring}[(\sin(q_z L_{Ring}/2)/q_r q_z)]\left[(r_{in}+w)J_1\left(q_r(r_{in}+w)\right) - r_{in}J_1(q_r r_{in})\right]\right|^2$$

(**2**)

q_z and q_r are the wavevectors parallel and perpendicular to the cylinder axis, J_1 is the Bessel function of order 1, and A_{Ring} is a fit parameter for the scattering amplitude from tubulin rings.

The arrangement of microtubules in a regular pattern within bundles gives rise to another source of modulation to the scattering intensity at the detector, the structure factor. The structure factor is defined by the scattering object positions within the lattice. In our case, the cylindrical microtubules are typically arranged in a 2D hexagonal or distorted pseudo-hexagonal lattice. SAXS work on microtubule-tau reaction mixtures in the absence of added forces, such as depletion and osmotic pressure, typically show that the bundled lattice structures fit well to the structure factor of a 2D hexagonal lattice[82], where peak positions in orientationally averaged systems should appear at reciprocal lattice vectors, q_{hk}, defined by the magnitude of the reciprocal lattice, **G**:

$$|\boldsymbol{G}| = \frac{4\pi}{\sqrt{3}d}\sqrt{h^2+k^2+hk} \qquad (\mathbf{3})$$

3. Complexes of tubulin oligomers and tau form a viscoelastic intervening network cross-bridging microtubules into bundles

3.1. Permissions and Attributions

The content of chapter 3 is the result of a collaboration with Phillip Kohl, Chaeyeon Song, Rebecca Best, Christine Tchounwou, Ximena Garcia Arceo, Peter Chung, Herbert Miller, Leslie Wilson, Myung Chul Choi, Youli Li, Stuart Feinstein, and Cyrus Safinya. My contributions were in: experiment conceptualization and development of methodology, data curation, experimental investigation, data visualization, writing the original manuscript draft, subsequent writing-review and editing.

A version of this work is currently published as a preprint on *bioRxiv* (https://doi.org/10.1101/2022.07.18.500499) and is undergoing revisions after submission to *Nature Communications*.

3.2. Abstract

The axon-initial-segment (AIS) of mature neurons contains microtubule (MT) fascicles (linear bundles) that are implicated as retrograde diffusion barriers in the retention of MT-associated protein (MAP) tau inside axons. While the role of tau in MT bundling is poorly understood, tau dysfunction and leakage outside of the axon is associated with neurodegeneration. We report on the structure of steady-state MT bundles in response to varying concentrations of divalent cations (Mg^{2+} or Ca^{2+}) in dissipative reaction mixtures containing -tubulin, full-length tau, and GTP at 37°C. A

concentration-time kinetic phase diagram generated by synchrotron small-angle X-ray scattering (SAXS) reveals a wide-spacing MT bundle phase (B_{ws}), a transient intermediate MT bundle phase (B_{int}), and a tubulin ring phase. Remarkably, SAXS analysis combined with TEM of plastic embedded samples provides direct evidence of an intervening network (IN) of complexes of tubulin oligomers and tau (≈5 nm wide filaments), which stabilize MT bundles. In this model, αβ-tubulin oligomers in the IN are crosslinked by tau's MT binding repeats, which also link αβ-tubulin oligomers to αβ-tubulin within the MT lattice. The finding of a new role for tubulin revises current dogma where cross-bridging of MTs is attributed entirely to interactions between MAPs. The tubulin-tau complexes of the IN should enhance the barrier properties of MT fascicles in preventing tau missorting to the somatodendritic compartment as happens during neurodegeneration. Furthermore, tubulin-tau complexes in the IN or bound to isolated MTs are potential sites for enzymatic modification of tau promoting nucleation and growth of tau fibrils in tauopathies.

3.3. Introduction

Microtubules (MTs) are hollow protein nanotubes resulting from GTP-mediated assembly of αβ-tubulin heterodimers, which stack to form GTP-tubulin oligomers and protofilaments (PFs). Linear PFs interact laterally to form the MT wall[1], with these interactions hypothesized to stabilize their straight conformation[2,3]. Once incorporated in a MT wall, GTP at the β-tubulin subunit can hydrolyze, forming GDP-tubulin PFs that tend to adopt a higher curvature conformation often leading to MT

disassembly[4]. These distinct PF conformations underlie MT dynamic instability (DI) and enable the stochastic switching between periods of slow growth (polymerization) and rapid depolymerization[2-6], regulated in part by the relative abundance of GTP- and GDP- tubulin. In cells, MT-associated proteins (MAPs) can also regulate DI and are implicated in the formation of MT bundles[7-11], which are involved in numerous cellular functions[8,12,13]. Linear MT bundles (fascicles, Supp. Fig. 1) with large wall-to-wall spacing are found in the central core of the axon initial segment (AIS) of mature neurons[14-16] and form a retrograde diffusion barrier for MAP tau, compartmentalizing tau in the axon[17].

In our study, we focused on mixtures of $\alpha\beta$-tubulin and the canonical, full length isoform (4RL) of MAP tau, an intrinsically disordered protein which binds to MTs, partially suppresses DI, and facilitates the transport of cargo along MTs in axons[8,18-23]. Tau dysfunction is implicated in neurodegenerative "tauopathies", which include Alzheimer's disease[24], FTDP-17[25], and chronic traumatic encephalopathy[26]. Humans express six wild-type tau isoforms resulting from alternative splicing of exons 2, 3, and 10 of the MAPT gene (Fig. 1A)[27]. The N-terminal projection domain (PD) and the C-terminal tail of tau protrude radially outward when bound to MTs, while tau's proline-rich region and MT binding region (MTBR) are enriched with cationic residues thought to interact with negatively charged residues at the carboxyl terminal end of $\alpha\beta$-tubulin[28-30].

In-vitro experiments of paclitaxel-stabilized MTs in the absence of tau show that divalent cations induce ion-specific MT bundling[31] and depolymerization[32]. In follow-up studies excluding paclitaxel, tau-stabilized MTs reproduced linear bundles

mimicking MT fascicles found in the AIS[33]. Building on those results, the current study seeks to elucidate ion-specific effects on the structure and stability of tau-stabilized MT bundles by adding Mg^{2+} or Ca^{2+} to minimal dissipative reaction mixtures at 37°C containing $\alpha\beta$-tubulin, 4RL-tau, and GTP in standard PIPES buffer at pH 6.8[34]. The mixtures contained a 1/20 tau/tubulin-dimer molar ratio, which corresponds to sub-monolayer coverage of tau on MTs in the mushroom regime[35]. Divalent cation concentrations were in the millimolar range, approximating average cellular Mg^{2+} content[36]. Thus, a motivation for the study was to reveal ion-specific effects between metal ions at physiological Mg^{2+} concentrations in a minimal, cell-free model of MT fascicles of the AIS.

Time-dependent synchrotron small-angle X-ray scattering (SAXS) was used to monitor samples over 33 hours, *in the presence of excess GTP*, revealing three distinct tubulin structural states. Kinetic phase diagrams generated from this data show that the tau-tubulin structural state is a function of both time and Mg^{2+} or Ca^{2+} concentration (added to the PIPES buffer, Methods). Phase diagrams guided the selection of specific time points for parallel transmission electron microscopy (TEM) of plastic embedded samples, providing real-space images for comparison to reciprocal-space SAXS data. In agreement with previous measurements by Chung et al.[33], widely-spaced MT bundles (labeled B_{ws} with MT wall-to-wall spacing $d_{w\text{-}w} \approx 40$ to 45 nm), were stable below critical lower divalent cation concentrations $c = c_{lower}$ (≈ 0.8 mM $CaCl_2$ and ≈ 1.6 mM $MgCl_2$). Furthermore, MT bundled structures remained stable against added monovalent cations (up to 150 mM KCl).

Over a narrow range of added Ca^{2+} or Mg^{2+} concentrations ($c_{lower}<c<c_{upper}$ c_{upper} ≈ 1.4 mM $CaCl_2$ and ≈ 2.4 mM $MgCl_2$), the B_{ws} state undergoes a novel, complex structural evolution over a period of hours. The onset of this structural evolution is signaled by the depolymerization of a fraction of MTs, which leads to a sudden increase in the formation of tubulin rings and curved tubulin oligomers (observed in SAXS). During this time period, remaining bundled MTs enter a transient intermediate bundle state (B_{int}), with a more ordered lattice and smaller $d_{w\text{-}w}$ (≈ 30-35 nm). In agreement with these SAXS findings, TEM images of MTs fixed in the B_{int} state show more tightly packed bundles and significantly more cross-bridges between MTs (observed in both states as ≈ 5 nm wide flexible filaments and rings), suggesting that increased tubulin depolymerization products directly participate in the structural rearrangement of MT bundles by increasing the number of MT-MT cross-links.

Taken together, SAXS and TEM data are consistent with MTs in both the B_{ws} and B_{int} states bundled by an intervening network of tubulin oligomers complexed with tau. This represents a significant revision to current dogma where cross-bridges between MTs were attributed solely to MAPs [7-12,37]. In our model, MT bundle formation is due to "coded assembly" by tau's MT binding repeats (orange sections in Fig. 1A and 1B) acting as the glue linking αβ-tubulin oligomers in the viscoelastic intervening network. In this role, tau links αβ-tubulin oligomers within the intervening network to one another *and* to αβ-tubulin within the MT lattice (Fig. 1B). Large MT wall-to-wall spacings observed in both bundled states (much larger than the size of tau's PD) are set by the average radius of curvature of tau-coated, curved tubulin oligomers and rings.

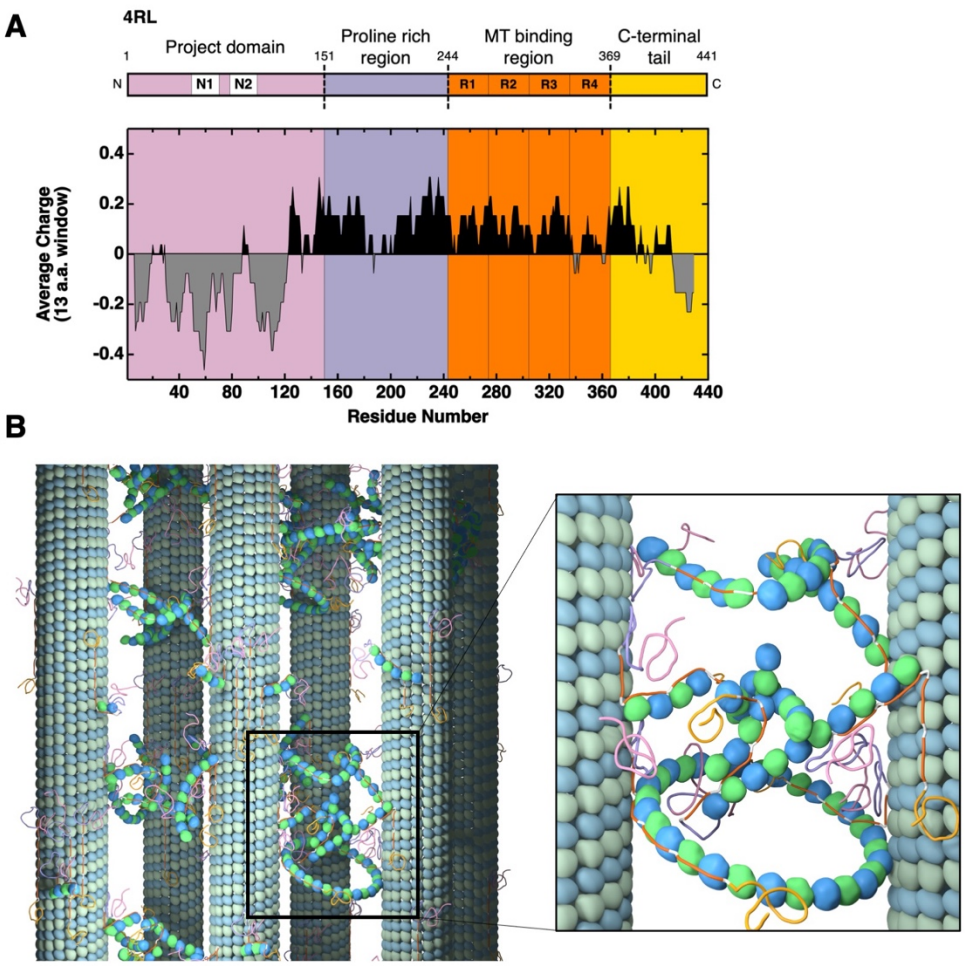

Figure 3.1: Tau charge distribution and tau-tubulin network stabilizing bundled MTs (**A**) Schematic and average charge profile of full length 4RL tau with major features labeled, including inserts 1 and 2, encoded by exons 2 and 3, respectively, and all four MT-binding repeats (R1-R4). 4RL tau is depicted with labeled domains: N-terminal tail consisting of the projection domain (PD) and proline rich region, the microtubule (MT) binding region (MTBR), and the C-terminal tail [28-30]. The charge distribution is calculated using a rolling sum over thirteen residues. Despite anionic regions at the N- and C-termini, tau isoforms have a net cationic charge, which contributes to tau's binding (via MTBR) to negatively charged residues of $\alpha\beta$-tubulin. Data are from the National Center for Biotechnology Information Protein Database (accession number NP_005901.2). (**B**) Cartoon of a microtubule bundle (left) with blow-up (right) showing an intervening network of complexes of tubulin oligomers (curved short protofilaments and rings) and tau, which stabilizes MT bundles in the B_{ws} and B_{int} phases. The cationic MT binding repeats of tau (orange sections) link $\alpha\beta$-

tubulin oligomers both to other free tubulin oligomers and to $\alpha\beta$-tubulin dimers within the MT lattice, creating the intervening network that cross-bridges neighboring MTs. Tau is depicted to bind either side of curved tubulin oligomers and rings consistent with studies that show tau may bind (via the MT binding repeats) either the outside surface or lumen of the MT[38,69,70].

3.4. Results

3.4.1. Time-dependent SAXS generates kinetic phase diagrams revealing three distinct assembly structures for αβ-tubulin/tau/divalent cation/GTP mixtures at 37 °C

To understand how divalent cation content modulates the stability and structural features of tau-mediated MT bundles, time-dependent synchrotron SAXS measurements were performed on tubulin reaction mixtures (40 μM) containing 2 mM GTP, co-assembled at 37 °C with 4RL-tau (tau to tubulin-dimer molar ratio, Φ_{4RL} = 0.05) at varying $CaCl_2$ or $MgCl_2$ concentrations (0 to 5 mM added to standard PIPES buffer containing 1 mM of Mg^{2+} (Methods)). Analysis of all azimuthally averaged SAXS profiles reveals three distinct concentration-dependent tau-tubulin structural phases outlined in Fig. 2A.

At initial timepoint t_0, all samples below a threshold divalent concentration of 1.4 mM added Ca^{2+} or 2.4 mM added Mg^{2+} exhibited MT bundling characteristics indistinguishable from controls with no added divalent cations (Supp. Fig. 2). A typical SAXS profile representing the B_{ws} phase is plotted in Fig. 2A and displays scattering characteristics indicative of strong MT polymerization and registers Bragg peaks consistent with 2D hexagonal packing of MTs (q_{10}, $q_{11}=3^{1/2}q_{10}$, $q_{20}=2q_{10}$, $q_{21}=7^{1/2}q_{10}$, $q_{30}=3q_{10}$, $q_{22}=12^{1/2}q_{10}$). Wall-to-wall distances ($d_{w\text{-}w}$, Fig. 2B) calculated from the location of q_{10} (Methods) ranged between $d_{w\text{-}w}$ = 29.5 and 33.1 nm for all samples, consistent with values of the widely-spaced MT bundle state reported previously [33].

Above threshold concentrations tau-tubulin reaction mixtures produced scattering profiles at initial timepoints that were markedly different from the B_{ws} phase and are indicative of a new intermediate bundled state (B_{int}) (Fig. 2A, profiles at 1.5

mM and 1.6 mM Ca^{2+}). One major difference between the two states is the characteristic shift in location of all Bragg peaks to higher *q* values, implying that the wall-to-wall distance is smaller in the B_{int} than in the B_{ws} phase ($d^{int}_{w\text{-}w}$ = 24.5 to 26.7 nm). The Bragg peaks are also sharper in the B_{int} state (Fig. 2A, full-width at half maximum (FWHM) for q_{10}, vertical lines at 1.2 mM and 1.6 mM Ca^{2+}), indicating that the coherent domain size of the MT lattice is much larger, despite having a smaller lattice parameter and decreased scattering from bundled MTs (Fig. 2A, scattering intensity of (1,0) peak diminishes with increased Ca^{2+}). Unlike the B_{ws} phase, this scattering data shows that, within the B_{int} phase, Ca^{2+} and Mg^{2+} severely inhibit MT polymerization and increase the prevalence of depolymerized tubulin products in a concentration dependent manner, indicated by the decrease in bundled MT scattering and the increase in scattering at the first local minimum (Fig. 2A, arrows), respectively.

At higher Ca^{2+} and Mg^{2+} concentrations (1.9 - 3.0 mM Ca^{2+} or 2.6 - 3.0 mM Mg^{2+}) MT polymerization was substantially inhibited, and scattering was dominated by single tubulin rings (Fig. 2A, broad oscillations at 2.5 mM Ca^{2+}) and curved tubulin oligomers. As previously reported for free tubulin heterodimers and oligomers [38-40] and for tubulin spiral structures under non-assembly promoting conditions [41], we expect these curved tubulin structures to be coated with tau. SAXS signatures of the tubulin ring state dominated and remained unchanged with increased divalent concentrations.

Mg^{2+}- or Ca^{2+}-induced structural changes (smaller lattice size, larger bundle domain size, increased depolymerization) also occur as a function of time for samples

with intermediate concentrations of added Ca^{2+} or Mg^{2+} ($c_{lower} \approx 0.8$ to $c_{upper} \approx 1.4$ mM Ca^{2+} or $c_{lower} \approx 1.2$ to $c_{upper} \approx 2.2$ mM Mg^{2+}). As shown for 1.2 mM Ca^{2+} (Fig. 2C), each of these samples originates in the B_{ws} state but abruptly transitions to the B_{int} state after several hours. This transition is accompanied by increased scattering intensity at the first local minimum over time due to the rapid increase in MT depolymerization rate and tubulin ring proliferation, despite excess GTP remaining in the system up to 72 hours (Supp. Fig. 2). Depolymerization of nearly all MTs and the structural evolution to the ring state is typically observed between 6 to 9 hours after the B_{ws} to B_{int} transition. Fig. 2C (1.2 mM Ca^{2+}) shows a typical example, where the B_{ws} phase is observed at t_0 +6 hrs and t_0 +12 hrs, the B_{int} phase at t_0 +18 hrs and t_0 +21 hrs, and the ring state at t_0 +30 hrs.

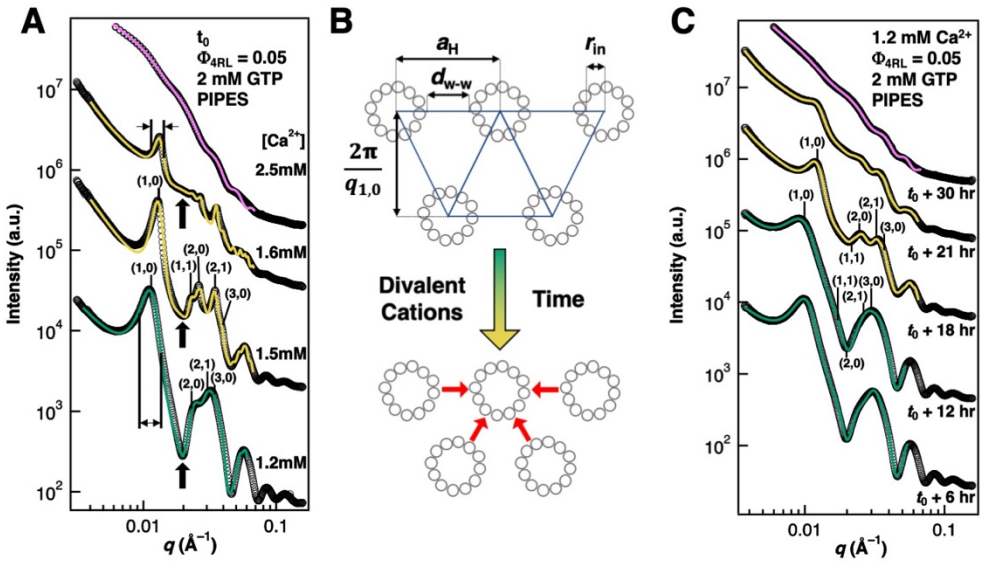

Figre 3.2: Time-dependent synchrotron SAXS data with increasing divalent cations in PIPES buffer at pH 6.8 reveals an intermediate bundled (B_{int}) microtubule state between the bundled wide-spacing (B_{ws}) and the tubulin ring states (**A**) SAXS data (open circles) and corresponding fits (solid lines) for increased Ca^{2+} concentrations at t_0, where t_0 is the time of the first measurement. Indexing for three lower profiles is for 2D hexagonal lattice of MTs. The intermediate bundle state (B_{int}, profiles at 1.5mM and 1.6mM Ca^{2+}) is differentiated from the widely-spaced bundle state (B_{ws}, profile at 1.2 mM Ca^{2+}) by peaks shifted to larger q (i.e. smaller lattice spacing), decreased peak widths (compare 1,0 peak positions for 1.6mM and 1.2mM Ca^{2+}), and increased scattering intensity at local minima of the MT form factor (solid arrows at 1.2mM, 1.5mM, and 1.6mM Ca^{2+}). At 2.5 mM Ca^{2+} the SAXS is dominated by tubulin rings and curved oligomers. (**B**) Cartoon of hexagonal MT bundles in the B_{ws} (top) and B_{int}, (bottom) states highlights changes in MT-MT spacing. (**C**) SAXS data (open circles) and corresponding fits (solid lines) with increasing time at 1.2 mM Ca^{2+}. Evolution of SAXS profiles show that phase transitions occur from B_{ws} to B_{int} (between t_0 +12 and t_0 +18 hrs) and from B_{int} to the tubulin ring state (between t_0 +18 and t_0 +30 hrs).

Kinetic phase diagrams for Ca^{2+} (Fig. 3A) and Mg^{2+} (Fig. 3B) summarize the SAXS data and visualize distinct regions where the B_{ws} (green), B_{int} (yellow), and (tau-coated) tubulin rings (magenta) are dominant. This data reveals a clear decrease in the lifetime of the B_{ws} with increased divalent cation content, that is likely related to a similar effect by tetra-valent spermine on paclitaxel-stabilized MTs[42], although on longer time scales of order days at room temperature (due to the larger stabilizing effect of paclitaxel on MTs compared to tau). This effect was not observed with increased monovalent cations added to standard buffer, instead showing that d_{w-w} remained constant over the tested range of added KCl (up to 150mM KCl added to the PIPES buffer, Fig. 4).

While the MT bundles and curled tubulin oligomers are the dominant structures of the B_{ws} and ring state, respectively, we note that the B_{int} state is a two-phase system of bundled MTs and tubulin rings, where scattering contributions from both bundled MTs and tubulin rings can be resolved. Therefore, the ring state describes SAXS profiles where the q_{10} peak of the B_{int} phase can no longer be resolved.

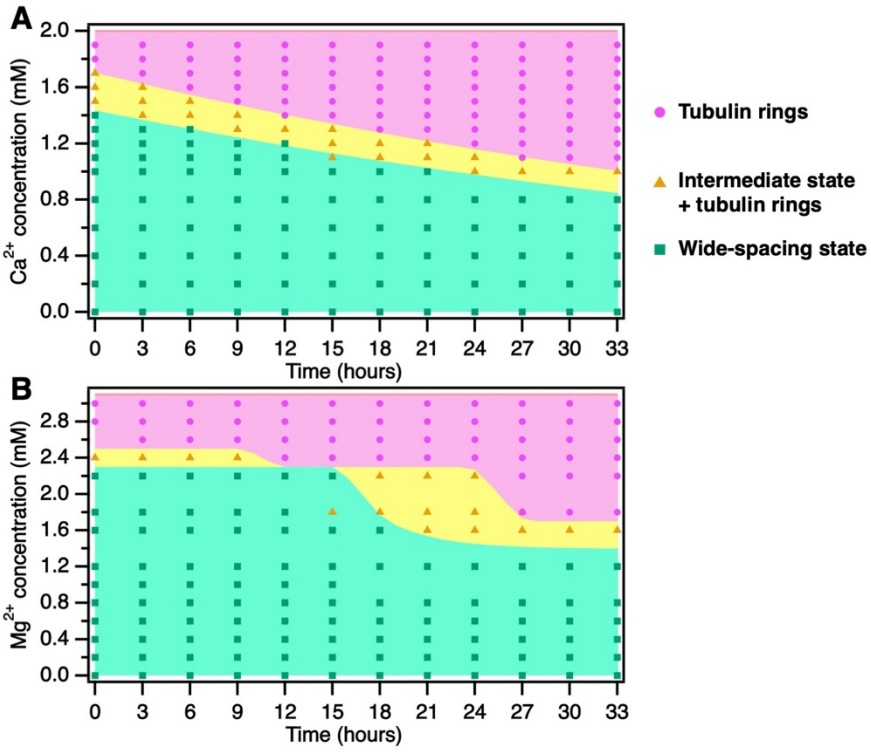

Figure 3.3: Kinetic phase diagrams of tau/tubulin mixtures as a function of Ca^{2+} or Mg^{2+} concentration and time All samples contained 0 to 5 mM Ca^{2+} or Mg^{2+} in addition to the 1 mM Mg^{2+} of the standard PIPES buffer (see Methods). Distinct B_{ws}, B_{int}, and (tau-coated) tubulin ring states are observed. Markers denoting different phases are color-coded with the SAXS fits plotted in Fig. 2.

While these phase transitions coincide with increased MT depolymerization, it is important to note that depolymerization is not occurring due to GTP depletion but is an effect of the added divalent cations. GTPase activity at the β-tubulin subunit occurs only for tubulin incorporated in a MT lattice[43-46], limiting the rate of GTP hydrolysis proportional to the ratio of lattice-bound tubulin to GTP. SAXS data indicates this ratio is highest (most GTPase activity) at low divalent cation concentrations, due to the prevalence of scattering from MTs. SAXS line-shape analysis of samples with low divalent cation concentrations (below 1.2 mM Mg^{2+} and 0.8 mM Ca^{2+}) indicates that MTs are stable at late time points (up to 72 hours, Supp. Fig.1), despite high tubulin:GTP ratios, implying that GTP is present well beyond experimental timeframes, even when the rate of hydrolysis is maximal. Thus, reaction mixtures with higher divalent cation content – where the B_{int} state and the ring state are observed – must also contain excess GTP, even as MT depolymerization occurs.

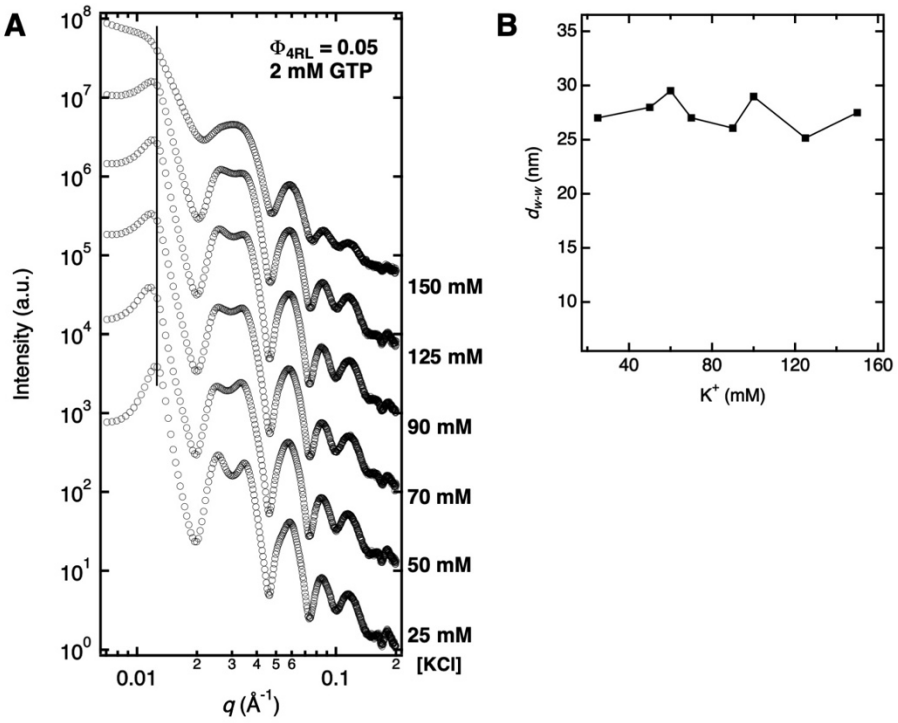

Figure 3.4: Synchrotron SAXS data reveals the wall-to-wall distance of bundled microtubules is not dependent on KCl concentration (**A**) SAXS data of tubulin/tau/GTP mixtures at 37°C and 4RL-tau to tubulin-dimer molar ratio Φ_{4RL} = 0.05 with increasing KCl concentration. SAXS scans are offset for clarity. (**B**) Plot of the fitted wall-to-wall distance (d_{w-w}) from SAXS data in (A) highlights the lack of change in d_{w-w} with increasing KCl concentration. Samples contained the stated KCl concentrations added to PIPES buffer at pH 6.8, which includes 1 mM of Mg^{2+}.

3.4.2. Plastic-embedded TEM images are consistent with SAXS data and reveal distinct structural features in the B_{ws} and B_{int} phases

To better understand structural differences between the two bundled states, TEM experiments were performed on plastic-embedded tau/tubulin/2mM GTP reaction mixtures in standard buffer containing 1.8 mM of added Mg^{2+} at 37 °C (Methods). Based on the phase diagram above, samples were individually prepared and fixed 3 (Fig. 5 A-C) and 18 hours (Fig. 5 D-F) after polymerization to capture the B_{ws} and B_{int} state, respectively. Consistent with SAXS line-shape analysis, cross-sectional images at lower (Fig. 5 A,D) and higher (Fig. 5 B,E) magnification show distinct phase-separated bundled domains at both time points. Larger domain sizes (bundle widths) are seen at 18 hours (Fig. 5 D,E) compared to 3 hours (Fig. 5 A,B in B_{ws} state), and measurements from higher magnification images also reveal an average interaxial spacing (a_H) between bundled MTs that is 7.1 nm larger in the B_{ws} phase (Fig. 5B) compared to the B_{int} phase (Fig. 5E), comparable to values measured via SAXS (Δa_H = 6.7 nm). Similarly, TEM reveals MT pairs at 18 hours have more cross-linkages and lower heterogeneity of wall-to-wall distances compared to those at 3 hours, which coincides with narrower SAXS peak widths (i.e. larger coherent domain sizes) observed for the B_{int} phase. Additionally, low-magnification TEM images (Fig. 5C and F) reveal structural features on length scales beyond the resolution of SAXS, showing that MT bundles in the intermediate state form larger extended arrays than in the wide-spacing state.

In agreement with plastic-embedded TEM measurements of Chung et al.[33] (with no added Mg^{2+} to the buffer), few well-defined hexagonal arrays are observed,

especially in the wide-spacing state. Instead, there is an apparent preference for MTs to form linear, string-like bundles (Fig. 5 A,B,D,E white boxes) reminiscent of fascicles found within the axon-initial-segment (Supp. Fig. 1). Even within regions of high microtubule density (Fig. 5D), where the probability of MT-MT interactions is higher, stacks of linear arrays or branched chains of MTs are more abundant than true hexagonal bundles. This apparent preference for 1-dimensional MT bundling, despite close lateral proximity of the linear arrays, may be due to broken cylindrical symmetry with tau distributed non-uniformly on the MT surface, consistent with reports that tau forms phase-separated complexes on the surface of MTs[47-49].

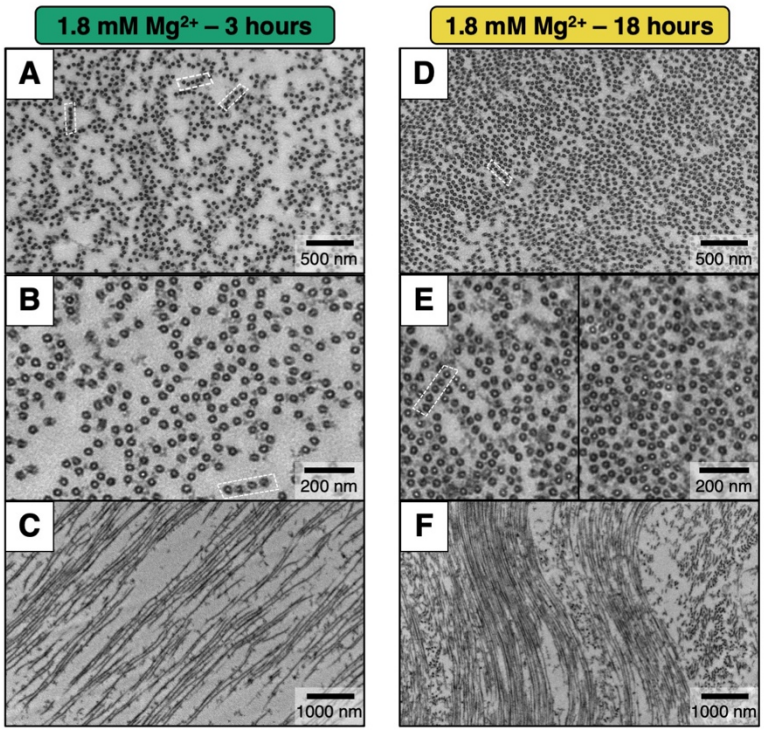

Figure 3.5: Plastic-embedded TEM confirms the existence of the B_{ws} and B_{int} bundled phases Electron microscopy of microtubule assemblies prepared at 37 °C with mixtures of tau, tubulin, and 2 mM GTP in PIPES buffer at pH 6.8 with 1.8 mM added Mg^{2+} and fixed after 3 hours (A-C) and 18 hours (D-E). Time points for sample fixation were selected based on SAXS data for samples prepared with identical conditions, where the wide-spacing B_{ws} and the intermediate B_{int} bundled phases were present at 3 and 18 hours, respectively. **(A, D)** Top panels depicting cross-sections at low magnification show the extent of MT bundling for both phases (B_{ws} state in A and B_{int} state in B). The images further show the propensity for MT bundles to arrange in linear arrays (dashed white boxes). **(B, E)** Higher magnification cross-sections at 3-hour and 18-hour timepoints highlight the larger MT-MT spacing in the B_{ws} compared to B_{int} phase and the larger number of MT-MT bonds per MT (and larger average number of neighbors for each MT) in the B_{int} compared to the B_{ws} phase. **(C, F)** Low magnification side views at 3-hour and 18-hour timepoints show that the width of the MT bundles (i.e. bundle size) is much larger in the B_{int} compared to the B_{ws} phase, and the spacing between MTs is smaller in the B_{int} compared to the B_{ws} phase, consistent with trends observed in SAXS data. All samples contained the stated Mg^{2+} concentrations added to standard PIPES buffer at pH 6.8, which includes 1 mM of Mg^{2+} (see Methods).

3.4.3. Distinct types of unpolymerized tubulin oligomers in the B_{ws} and B_{int} bundled phases

To quantify the spike in MT depolymerization corresponding to the B_{ws} to B_{int} transition observed via SAXS (i.e. filling in of local minima, Fig. 2A,C), scattering data was fit to a model profile, *I*(q) (Methods), which consists of three separate terms modeling hexagonally bundled microtubules[31,33,42], tubulin rings, and background scattering[50] to account for a constant background level and for scattering from unpolymerized tubulin oligomers (i.e. oligomers not in the MT lattice) with average curvature much less than that of the closed rings. Separating into these three terms allowed us to measure the relative abundance of depolymerized tubulin in the ring configuration compared to lower-curvature configurations (Methods). Comparing fit data from all of our samples revealed that the proportion of tubulin mass in the ring state is much higher in the B_{int} compared to the B_{ws} state.

Fits to the time-dependent SAXS data of reaction mixtures polymerized with 0.6 and 1.8 mM added Mg^{2+} (Fig. 6, A–D) highlight the differences in scattering from unpolymerized tubulin oligomers between the B_{ws} and B_{int} states, similar to behavior found for Ca^{2+} samples (Fig. 2 A, C). Solid lines through the SAXS profiles in Fig. 6(A,C) are fits of the data to *I*(q) (Methods). For 0.6 mM Mg^{2+} (below $c_{lower} \approx 1.6$ mM Mg^{2+}) the B_{ws} state is stable for the duration of the experiment, despite indications of gradual MT depolymerization due to ongoing partially suppressed dynamic instability. Overlapping the SAXS profiles without offset shows a slight increase in scattering intensity at the first local minimum over time (Fig. 6B, solid arrows), but not at all other minima, indicating that tubulin rings were not formed (Methods). This

phenomenon is reproduced for all samples that do not enter the B_{int} state, indicating that tubulin rings are not produced over time in the B_{ws} state (even up to 72 hours with no added divalent cations, Supp. Fig. 2). Instead, only low-curvature tubulin oligomers are produced.

For Mg^{2+} concentrations between c_{lower} and c_{upper} (≈ 1.6 to ≈ 2.4 mM Mg^{2+}), the B_{ws} state is stable for many hours with characteristically little tubulin ring formation (Fig. 6C-D, < 15 hours). However, transitioning to the intermediate bundled state coincides with a sudden spike in scattering intensity at all form factor minima (Fig. 6D, solid arrows). This distinct change in scattering (between 12 and 15 hours for 1.8 mM Mg^{2+}) is well described by an increase in scattering from tubulin rings (Methods). Plots of the raw scattering data for 1.8 mM Mg^{2+} without offset (Fig. 6D) show remarkable overlap of scattering intensity around the local minima at t_0 +18 and t_0 +30 hrs, with oscillations in SAXS at t_0 +30 hrs well described by the theoretical scattering profile of a single tubulin ring (r_{in} = 16.3 nm, Methods). Whole-mount TEM images prepared at 18 hours (Fig. 6E) confirm this observation made with SAXS, showing a relative abundance of individual and aggregated tubulin rings (Fig. 6E). Together, our SAXS and TEM data indicates that changes to the bundled MT lattice only occur upon the proliferation of tubulin rings.

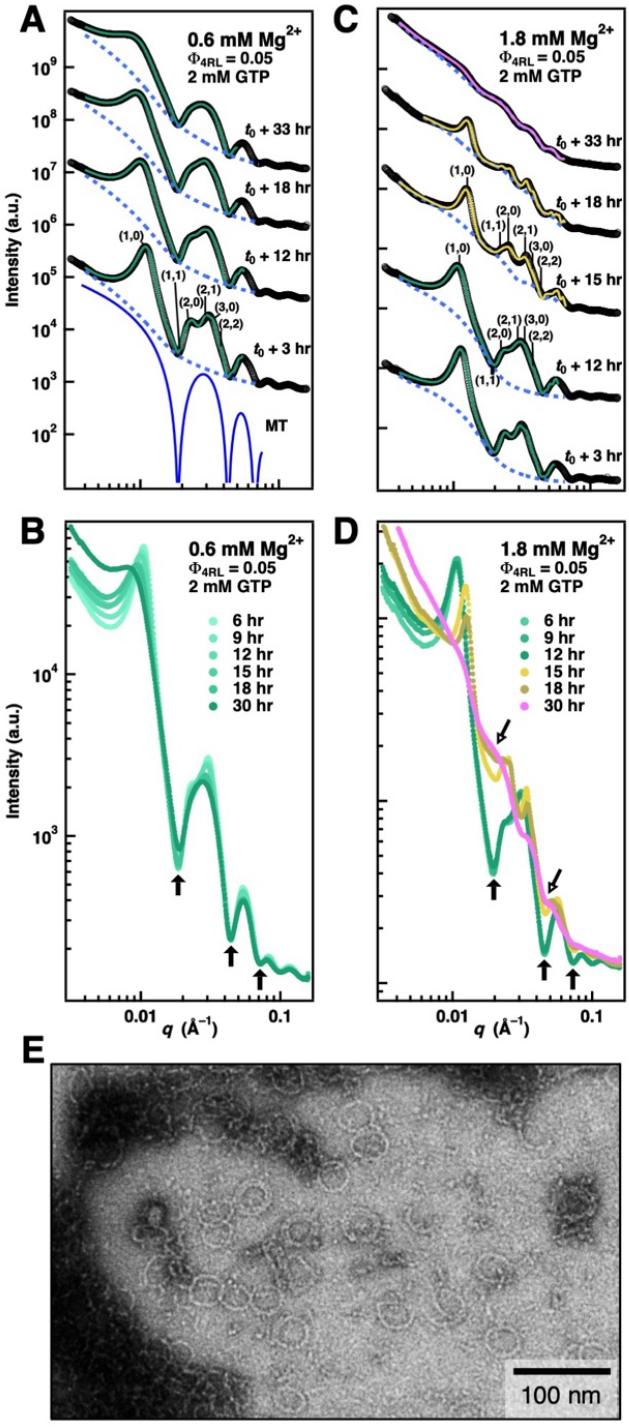
A
0.6 mM Mg2+
Φ4RL = 0.05
2 mM GTP
t0 + 33 hr
t0 + 18 hr
t0 + 12 hr
t0 + 3 hr
MT
(1,0)
(1,1)
(2,0)
(2,1)
(3,0)
(2,2)
Intensity (a.u.)
C
1.8 mM Mg2+
Φ4RL = 0.05
2 mM GTP
t0 + 33 hr
t0 + 18 hr
t0 + 15 hr
t0 + 12 hr
t0 + 3 hr
B
0.6 mM Mg2+
Φ4RL = 0.05
2 mM GTP
6 hr
9 hr
12 hr
15 hr
18 hr
30 hr
q (Å−1)
D
1.8 mM Mg2+
Φ4RL = 0.05
2 mM GTP
E
100 nm

Figure 3.6

Figure 3.6: Time-dependent synchrotron SAXS data at 0.6 and 1.8 mM Mg^{2+} in the wide-spacing (B_{ws}) and intermediate (B_{int}) microtubule (MT) bundle states reveal prevalence of rings in the B_{int} state (**A**) SAXS data (open circles, profiles offset for clarity) and corresponding fits (solid lines) of a sample at 0.6 mM Mg^{2+} (below c_{lower} ≈1.6 mM Mg^{2+}) in the B_{ws} state (2D Hexagonal peaks indexed for profile at t_0 +3 hrs). Bottom profile (solid blue curve) depicts the form factor of a MT. (**B**) Data from (A) plotted without offset. Solid arrows point to MT form factor minima, highlighting nominal change in non-MT scattering over time. (**C**) SAXS data (open circles, profiles offset for clarity) and corresponding fits (solid lines) at 1.8 mM Mg^{2+} (between c_{lower} ≈1.6 mM Mg^{2+} and c_{upper} ≈ 2.4 mM Mg^{2+}) show a transition with increasing time from the B_{ws} (profiles at t_0 +3 hrs and t_0 +12 hrs) to the B_{int} (profiles at t_0 +15 hrs and t_0 +18 hrs) and to the tubulin ring state (profile at t_0 +33 hrs). Dashed lines are non-MT scattering contribution obtained from fits. 2D Hexagonal peaks indexed for profiles at t_0 +12 hrs (B_{ws}) and t_0 +15 hrs (B_{int}). (**D**) Data from C without offset. An abrupt increase in tubulin ring scattering fills in the minima of the MT Form Factor (open arrows) at the transition between t_0 +12 and t_0 +15 hours. The fit lines in A-D are color-coded (green, yellow, and magenta represent the B_{ws}, B_{int}, and tubulin ring states, respectively). (**E**) Parallel whole-mount TEM image taken at t_0 + 18 hrs of a sample prepared with 1.8 mM Mg2+ added, showing abundance of single tubulin rings. Samples contained the stated Mg^{2+} concentrations added to PIPES buffer at pH 6.8, which includes 1 mM of Mg^{2+}.

3.4.4. Abrupt proliferation of tubulin rings occurs at the same time as the decrease in microtubule wall-to-wall spacing, signaling the B_{ws} to B_{int} transition.

Figure 7 summarizes the results obtained from fitting SAXS data to $I(q)$. Within the B_{ws} state (Fig. 7, arrows indicate the last time point where B_{ws} was observed), $d_{w\text{-}w}$ increased rapidly at early time points due to a relaxation from sample centrifugation (Methods) and more slowly thereafter, reaching values up to $d_{w\text{-}w} \approx 49$ nm at 33 hours (Fig. 7A,C). Unlike in the B_{ws} state, $d_{w\text{-}w}$ spacings are comparatively stable in the B_{int} state. The average stabilized wall-to-wall distance in the B_{int} state for samples that transitioned during the experiment was 29.8 nm and was independent of $d_{w\text{-}w}$ prior to the time of transition. Similarly, samples initially observed in the intermediate B_{int} state at t_0 (yellow regions at time = 0, Fig. 3A,B,) show no relaxation or increase in $d_{w\text{-}w}$ over time (unlike the B_{ws} state), instead converging to average spacing $d_{w\text{-}w}$ = 30.4 nm for Mg^{2+} and 26.4 nm for Ca^{2+}.

The stability of $d_{w\text{-}w}$ values measured in the B_{int} state relative to those in the B_{ws} state implies that stronger interactions dictate MT-spacing in the B_{int} compared to the B_{ws} state. This implication is further substantiated by the co-occurrence of the drop in $d_{w\text{-}w}$ and the increase in coherent domain size (≈ 41 percent growth in the 6 hours following the transition Supp. Fig. 3) upon transitioning to the B_{int} state (i.e. time between data collected at the arrows in Fig. 7A,C and the next data point).

For each sample, comparing $d_{w\text{-}w}$ to the amplitude of scattering from tubulin rings (A_{ring}, Fig. 7B,D) highlights the striking synchronization between the proliferation of tubulin rings and abrupt drop in $d_{w\text{-}w}$. This reduced MT-MT spacing, together with

the increase in MT bundle domain size, precisely when increasing amounts of rings and curved tubulin oligomers begin proliferating, suggests that tubulin oligomers directly affect the bundling of MTs and drive the B_{ws} to B_{int} transition observed through SAXS and TEM.

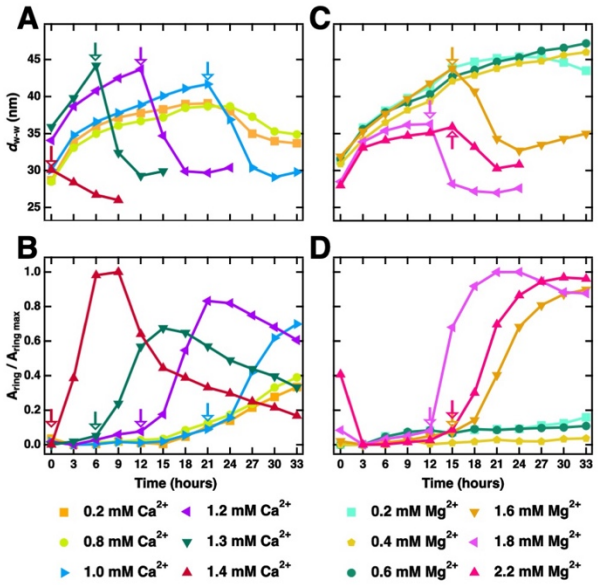

Figure 3.7: Change in the microtubule (MT) wall-to-wall spacing, upon transitioning from the wide-spacing (B_{ws}) to the intermediate (B_{int}) MT bundle state, correlates with tubulin ring proliferation. (**A** and **C**) Wall-to-wall spacings ($d_{w\text{-}w} = a_h - 2[r_{in} + w]$) plotted as a function of time for the series of Ca^{2+} (A) and Mg^{2+} (C) samples (SAXS data shown in Figures 2 and 6, respectively). Some data points omitted for clarity. Arrows indicate the latest time point at which the B_{ws} state is observed before the sample transitions to the B_{int} state. (**B** and **D**) Fitted tubulin ring scattering amplitude plotted as a function of time for the same series of Ca^{2+} (B) and Mg^{2+} (D) samples. Amplitudes are normalized by the maximum ring scattering measured. Arrows indicate the latest time point at which the bundled wide-spacing (B_{ws}) state is observed before the sample transitions to the bundled intermediate (B_{int}) state, with increases in the tubulin ring scattering amplitude observed after. Comparisons between (A) and (B) for the Ca^{2+} series and between (C) and (D) for the Mg^{2+} series show that the onset of tubulin ring proliferation occurs concurrently with the transition from the B_{ws} to the B_{int} state. Time "0" on the x-axis corresponds to t_0, as defined in Fig. 2. All samples contained the stated Mg^{2+} or Ca^{2+} concentrations added to standard PIPES buffer at pH 6.8, which includes 1 mM of Mg^{2+} (see Methods).

3.4.5. Increasing unpolymerized tubulin oligomer content induces the transition from B_{ws} to B_{int}

To directly test the effect of enhancing unpolymerized tubulin oligomer content on MT bundling, time-dependent SAXS experiments were devised to modulate dynamic instability. Protofilaments (tubulin oligomers) in excess GTP are known to adopt a higher curvature conformation at low temperature[51,52]. Therefore, lowering the temperature of the sample environment below a critical temperature for polymerization pushes the tubulin dynamic equilibrium toward depolymerization, effectively increasing the tubulin oligomer content in solution. Monitoring a control sample (i.e. with no added divalent cations) while the temperature was quickly dropped from 37 °C to 5 °C revealed that the otherwise stable wide-spacing state (which consists of MT bundles co-existing with tubulin oligomers from ongoing suppressed dynamic instability) was stable down to temperature readings of 19 °C, with no increase in scattering from depolymerized tubulin (Fig. 8, bottom two profiles). However, below 19 °C, signs of the B_{int} state abruptly appear, including the characteristic shift in hexagonal Bragg peaks to higher q, coinciding with a sudden increase in tubulin scattering at 13.8 °C and at 5.8 °C (evidenced as the filling in of the minima in Fig. 8 at these temperatures compared to 34.5 °C and 19.0 °C). At these lower temperatures, $d_{w\text{-}w}$ decreased to a minimum value of 26.1 nm (change in wall-to-wall distance, $\Delta d_{w\text{-}w}$ = 8.8 nm), and scattering from tubulin rings was dominant below 5.8 °C (Fig. 8, 4.9 °C). This result further demonstrates the correlation between increased free tubulin oligomer content and MT bundle rearrangement as the system transitions from the B_{ws} to the B_{int} state. Additionally, it shows that $d_{w\text{-}w}$ can be altered

independent of any ionic changes to the buffer and only requires a change in free tubulin content, regardless of tubulin's nucleotide state.

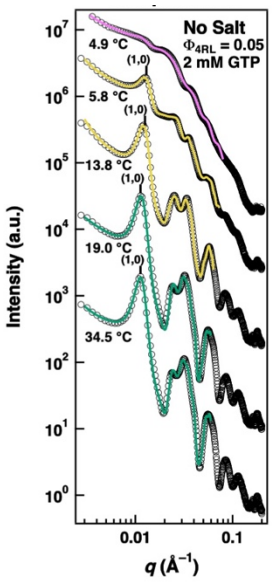

Figure 3.8: Synchrotron SAXS data reveal the stability of the bundled wide-spacing state depends on temperature (**A**) SAXS data (open circles) and corresponding fits (solid lines) for a control sample prepared with no added divalent cations while the temperature of the sample holder enclosure was rapidly dropped from 37 °C to below 5 °C. Temperatures were recorded simultaneously with each SAXS exposure and are displayed next to each scattering profile. Profiles represent the first and last time point at which the bundled wide-spacing (34.5 and 19.0 °C, respectively), the bundled intermediate (13.8 °C and 5.8 °C, respectively), and the tubulin ring state (4.9 °C) were observed. The fit lines are color-coded (green, yellow, and magenta represent the B_{ws}, B_{int}, and tubulin ring states, respectively).

3.4.6. Complexes of tubulin oligomers and tau act to cross-bridge microtubules and stabilize microtubule bundles.

Plastic embedded TEM side-views along the MT length provide potential insight to the structural components cross-bridging neighboring MTs and reveal a possible explanation for the B_{int} phase observed through SAXS. Close inspection of bundles in the B_{ws} phase at 3 hours at lower (Fig. 9 A,B) and higher (Fig. 9 C-E) magnifications reveals an extended intervening network of crosslinked proteins connecting MTs (Fig. 9 C-E). Remarkably, cross-bridges are seen not only connecting MTs within bundles (Fig. 9 C-E, solid black arrows), but also connecting neighboring bundles to one another (Fig. 9 C-E, dashed black arrows). Evidence of these tethers are also seen within the high magnification cross-sectional views shown in Fig. 4, with more crosslinks present in the B_{int} state (Fig. 5E) compared to the B_{ws} state (Fig. 5B).

While cross-bridges between bundled MTs in cells have been previously reported but attributed only to tau[7,8,53], intrinsically disordered proteins such as tau (≈ 0.5 nm in width) are too thin to be visualized by TEM in our plastic embedded preparations, implying that tau alone cannot make up the MT cross-bridge. In contrast, the morphology and dimension of the cross-bridges observed in TEM are consistent with tubulin oligomers, existing both as semi-flexible filaments (black solid and dashed arrows in Fig. 8 C-E) and as tubulin ring structures (white arrows in Fig. 8 C-E). Thus, TEM data provides direct evidence that tubulin oligomers (which may include tubulin rings) are a central component of the observed intervening network

between MTs and suggests that tau's role in MT bundling is to act as the "glue" (through the binding repeats) which connects tubulin oligomers.

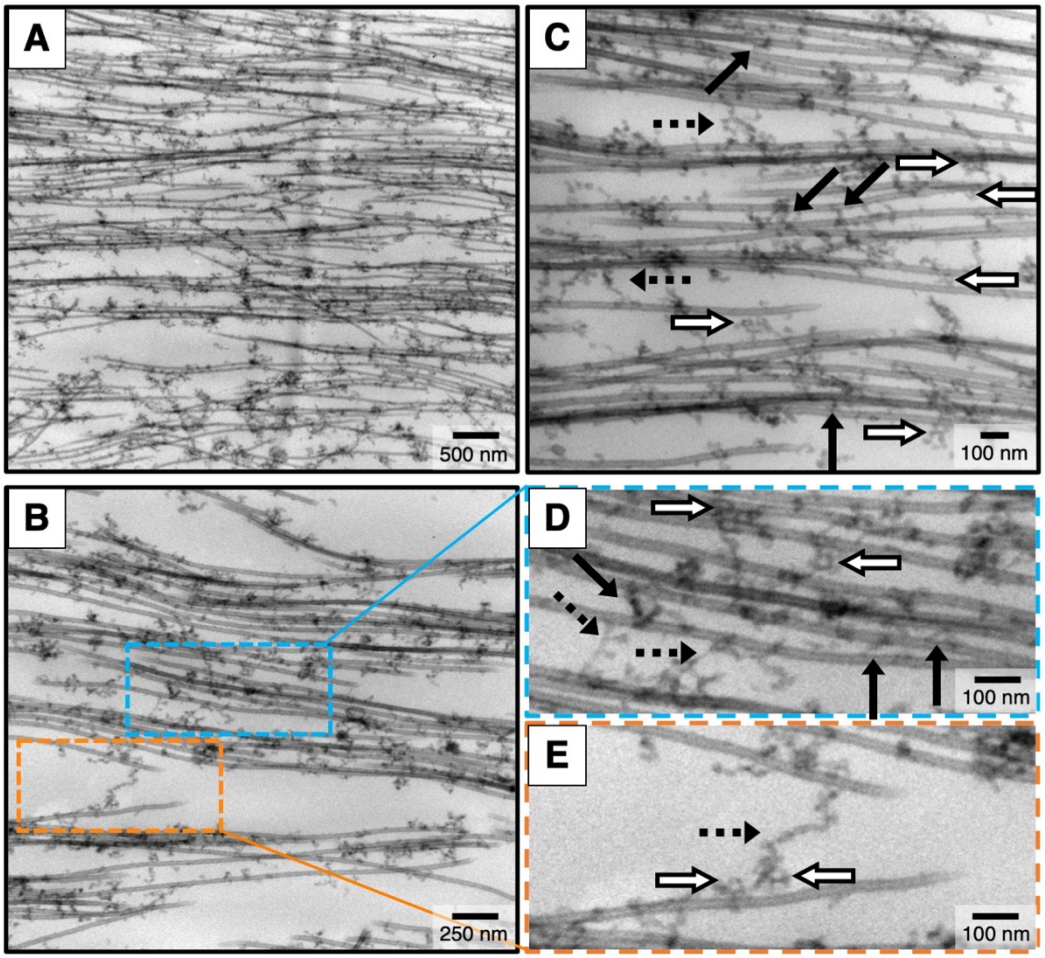

Figure 3.9: Plastic-embedded TEM provides evidence that complexes of tubulin oligomers and tau cross-bridge bundled microtubules Electron microscopy with increasing magnification of microtubule assemblies prepared from mixtures of tau, tubulin, and 2 mM GTP in standard buffer with 1.8 mM added Mg^{2+} at 37 °C and fixed after 3 hours. **(A, B)** At low and intermediate magnification, TEM images provide evidence that a network of filamentous proteins between bundled MTs is the linking medium that stabilizes MT bundles. **(C-E)** At higher magnifications the filamentous proteins of the network are seen to form MT-MT cross-bridges both within (black arrows) and between (black dashed arrows) bundled domains. The morphology of these cross-bridges is consistent with ≈ 5 nm wide semi-flexible tubulin oligomers. Tubulin ring structures (white arrows) are also present within the protein network. (D, E are expanded views of sections in B with blue and orange outlines.) Complexes of tubulin oligomers and tau are also observed coating MTs but not forming MT-MT

cross-bridges. All samples contained 1.8 mM Mg^{2+} added to standard PIPES buffer at pH 6.8, which includes 1 mM of Mg^{2+} (see Methods).

3.5. Discussion

Our combined SAXS and TEM data lead us to propose a model where complexes of tubulin oligomers and tau form a viscoelastic intervening network that cross-bridge MTs into bundles. We propose that bundling occurs due to *coded-assembly* where tau's MT binding repeats link together $\alpha\beta$-tubulin oligomers in the intervening network and also $\alpha\beta$-tubulin oligomers near the MT surface to $\alpha\beta$-tubulin in the MT lattice (Fig. 1B). The model presents an important revision to current dogma where cross-bridging between MTs is attributed entirely to tau[7,8,11,33,53-55].

Our model is consistent with SAXS data for both the B_{ws} and B_{int} GTP-stabilized MT bundled states and the transition between them. The abrupt influx of (tau coated) tubulin rings and curved tubulin oligomers (due to Mg^{2+} or Ca^{2+} mediated MT depolymerization of a fraction of MTs, either isolated or at the periphery of bundles where fewer cross-bridges to neighboring MTs exist) drives the transition from B_{ws} to B_{int} by increasing the average number of tubulin-tau cross-bridges (seen in TEM) in remaining transiently stable B_{int} bundles. Enhanced cross-bridging simultaneously decreases $d_{w\text{-}w}$ while increasing the bundle domain size in the B_{int} state.

The model reconciles years of contradicting reports regarding tau's role in bundling. While numerous early publications pointed to MT bundling as one of many roles of tau[7,8,11,53], recent studies show that the MT-stabilizing drug paclitaxel, which severely reduces free tubulin oligomers (at paclitaxel/tubulin-dimer molar ratios of

$\Lambda_{paclitaxel}$=1/1), suppresses MT bundling by all six tau isoforms[56]. Follow-up SAXS and TEM experiments showed that reducing paclitaxel below $\Lambda_{paclitaxel} \approx$ 1/8, restores free tubulin and tau-mediated MT bundles[57]. These findings are consistent with our central discovery that bundling of MTs by tau requires free tubulin oligomers.

In order to account for the average large $d_{w\text{-}w}$ observed via SAXS, current tau-only models for MT bundling require a highly extended conformation for the projection domain (PD) of tau (Fig. 1A). Proposals of short-range charge-charge interactions between weakly penetrating tau PDs and electrostatic zippers based on the dipolar nature of tau's PD require extensions of the PD by factors of two and four, respectively, (Methods). Such extensions of tau's PD are inconsistent with traditional polyelectrolyte theories[58] for chain stretching in the mushroom regime (at low tau/tubulin dimer molar ratio) and would require *sequence-specific* theories of highly stretched polypeptide chains at physiological salt concentrations (≈ 150 mM 1:1 salt). Previous SAXS experiments with tau-mediated MT bundles in the absence of the stabilizing agent paclitaxel[31,33,42] demonstrated that the wide spacing state is stable against increased osmotic pressure. In contrast, tau-coated paclitaxel-stabilized MTs at $\Lambda_{paclitaxel}$ = 1/1, do not form bundles below critical osmotic pressures[35] – likely due to the lack of sufficient free tubulin – but at high pressures form tightly packed bundles with $d_{w\text{-}w}$ spacings in the range of ≈ 3.5 - 4 nm, close to the radius of gyration of tau's PD and consistent with polyelectrolyte theory.

In our model, the wall-to-wall spacing is largely set by the average radius of curvature of tau-coated curved tubulin oligomers and tubulin rings (outer diameter ≈ 40 nm). Because the binding interactions between tau and tubulin oligomers are

specifically encoded by the MT binding repeats of tau, MT bundling is expected to be only weakly dependent on added monovalent salts. Indeed, $d_{w\text{-}w}$ is found to be essentially constant over a wide range of salt concentrations up to ≈ 150 mM KCl added to the buffer, which already contains ≈ 100 mM of a 1:1 salt (Fig. 4). Additionally, SAXS experiments designed to test the effect of tau coverage on MT wall-to-wall spacing, showed only small differences in $d_{w\text{-}w}$ between samples (Supp. Fig. 4), despite tau-tubulin dimer molar ratios ranging from Φ_{4RL} = 1/100 (mushroom regime) to Φ_{4RL} = 1/5 (brush regime), consistent with our model. In contrast, a tau-alone model would predict an increase in $d_{w\text{-}w}$ upon surpassing the mushroom-to-brush threshold $\Phi_{4RL} \approx 1/10$[35] and reduced bundling at tau tubulin ratio Φ_{4RL} = 1/100.

Together our results draw attention to the essential role of unpolymerized tubulin on MT bundling and highlight the necessity of operating within physiologically relevant experimental conditions as even minor differences in buffer conditions or temperature may have significant repercussions when drawing conclusions on tau's bundling function. Our finding that divalent cations near average physiological Mg^{2+} concentrations can destabilize dynamic, steady-state MT bundles at 37 °C, despite the presence of tau and excess GTP, is unexpected. In particular, at concentrations above a critical divalent concentration c_{lower} (≈ 1.6 mM Mg^{2+}), MT bundles undergoing suppressed dynamic instability abruptly become unstable, favoring the formation of tau-coated tubulin rings and effectively halting DI. This suggests a mechanism where MT growth and stability can be modulated within cells through fluctuations in local divalent cation concentrations, with potential consequences for cargo transport in

axons. Additionally, we expect the value of c_{lower} to be modulated by disease-relevant post-translational modifications and truncations of tau.

We expect tau's role in MT bundling to be synergistic with other proteins that promote MT bundle formation in neurons, such as TRIM46 that localizes to the proximal axon region promoting parallel MT bundles oriented with their plus end out[59-61]. Other members of the vertebrate family of MAPs with similar MT binding regions[62], interact with tubulin in a similar manner to tau. For example, the spacing between bundled MTs formed in cells expressing MAP2 is wider than those with tau[7,8,53,54]. MAP2 has a significantly longer projection domain (with a correspondingly much larger negative electrostatic charge) compared to tau, and the larger spacing may be due to a lower average curvature of tubulin oligomers complexed with MAP2 in the intervening network. It would be important to address the precise nature of MT bundling due to MAP2 in cell-free studies of minimal reaction mixtures similar to what we have done for tau.

The implications of our discovery of an intervening network of complexes of tubulin oligomer and tau should spur further studies. For example, one major function for bundled MT fascicles at the axon-initial-segment (AIS) is as a filter for MT-based cargo trafficked between the soma and axon. An intervening tubulin-tau network stabilizing MT fascicles should lead to a more efficient retrograde diffusion barrier that captures and prevents tau leakage outside of the axon. Biochemical alterations to tau (as happens in Alzheimer's disease and other tauopathies) could further modulate the barrier properties in the AIS, with significant implications for missorting of tau to the somatodendritic compartment and neurodegeneration. Finally,

complexes of tubulin oligomers and tau of the intervening network, or those bound to MTs not in bundles, may represent an important site of chemical modification or fragmentation of tau by enzymes leading to aberrant tau behavior and nucleation and growth of tau fibrils in tauopathies.

3.6. Methods

Tubulin and Tau Purification Tubulin was purified from bovine brain, filtered into PEM 50 buffer containing 50 mM PIPES, 1 mM $MgSO_4$, 1 mM EGTA, and 0.1 mM GTP, pH 6.8 with ≈ 75 mM NaOH, and drop frozen into liquid nitrogen, as described previously[34]. Briefly, crude brain extract was subjected to two cycles of glycerol-free polymerization and depolymerization with centrifugation washes between each step. Resultant MAP-rich microtubules were separated into MAPs and tubulin through a phosphocellulose cationic exchange column. Purified bovine tubulin was purified in PEM50 with protein concentration between 7 and 14 mg/mL as measured by Braford assay using BSA as a standard.

Following standard procedures[63], Tau was expressed in BL21(DE3) pLacI cells (Invitrogen) with 18 hour incubation in 250 mL of LB media (10 g of tryptone, 5 g of yeast extract, and 10 g of NaCl per liter of DI water) followed by 24 hour incubation in 6 L of auto-induction media (10 g of tryptone, 5 g of yeast extract, 0.5 g of dextrose, 2 g of α-D-lactose and 5 mL of glycerol per liter of 25mM $NaHPO_4$, 25 mM KH_2PO_4, 50 mM NH_4Cl, 5 mM Na_2SO_4 in DI water). Bacteria were harvested by centrifugation in a Sorvall RC-5B Plus centrifuge at 5000 RPM for 10 minutes maintained between 4 °C and 10 °C. Bacteria resuspended in BRB80 buffer (80 mM PIPES, 1 mM EGTA

and 1 mM $MgSO_4$) pH 6.8 with ≈ 120 mM NaOH, total 1:1 ion equivalent of 160 mM, Debye length, λ_D ≈ 7.6 Å [64]) were lysed by passing through a French pressure cell three times at >900 PSI, subsequently boiled for 10 min, and then centrifuged at 10,000 RPM for 10 minutes. The supernatant was collected and passed over a phosphocellulose anionic exchange column and eluted with increasing concentration of $(NH_4)_2SO_4$ (up to 1 M) in BRB80. Tau-containing fractions were subsequently pooled and brought to 1.25 M $(NH_4)_2SO_4$, then further purified using hydrophobic interaction column chromatography (HisTrap Phenyl HP, GE Healthcare), eluted with decreasing concentration of $(NH_4)_2SO_4$ in BRB80. Fractions containing pure tau were pooled, then concentrated and buffer-exchanged into BRB80 by successive centrifugation cycles using Amicon Ultra-15 Centrifugal Units with MWCO = 10,000 (EMD Millipore, Darmstadt, Germany). Final tau stocks were stored at -80 °C until needed for experiments. Concentration was determined by SDS-PAGE comparison with a tau mass standard, the concentration of which had been established by protein mass spectrometry and stored at – 80 °C in BRB80 (80 mM PIPES, 1 mM EGTA, 1 mM $MgCl_2$, pH 6.8 with ≈ 120 mM NaOH, total 1:1 ion equivalent of 160 mM, Debye length, λ_D ≈ 7.6 Å [64]).

Sample Preparation Reaction mixtures were prepared on ice in the following way. Purified tubulin (92 uM stock) was thawed, diluted into PEM50 (50 mM PIPES, 1 mM EGTA, 1 mM $MgCl_2$, pH 6.8 with ≈ 75 mM NaOH, λ_D ≈ 9.6 Å), and mixed with solutions of GTP in PEM50 (100 mM stock), tau (37 uM stock in BRB80), and PEM50 buffer with additional $MgCl_2$ or $CaCl_2$ content (5 – 50 mM stocks). Final reaction mixtures

contained 4.0 mg/mL tubulin in 50 uL of buffer ($\lambda_D \approx 9.5$ Å). Sample tubes containing reaction mixtures were placed in a 37 °C water bath for 30 minutes of polymerization to reach dynamic equilibrium. The MT-tau reaction mixtures were then prepared for experiments as follows.

For SAXS, reaction mixtures were directly loaded into 1.5-mm diameter quartz mark capillaries (Hilgenberg GmbH, Malsfeld, Germany) after polymerization. Capillaries were subsequently spun in a capillary rotor in a Universal 320R centrifuge (Hettich, Kirchlengern, Germany) at 9,500 x *g* and 37 °C for 30 minutes to form protein-dense pellets suitable for SAXS. Pelleted capillaries were then sealed and held at 37 °C in a custom-made, temperature-controlled sample holder for data acquisition.

Sample preparations for whole-mount and plastic embedded TEM were described previously[31,33,42] with minor changes. Briefly, for whole-mount TEM, reaction mixtures were diluted into warm buffer to 0.2 mg/mL tubulin and loaded onto highly stable Formvar carbon-coated copper grids (Ted Pella, Redding, CA), with excess solution wicked with Whatmann paper after 2 minutes. 1% uranyl acetate was added to the grid for 20 seconds and wicked off. Then, five drops of Milipore H_2O (18.2 MΩ) were added and wicked off. Grids were allowed to dry for 24 hours at room temperature before imaging. For plastic-embedded TEM, reaction mixtures were centrifuged to a pellet in microcentrifuge tubes at 9,500 x *g* at 37 °C for 30 min. Supernatant was removed, and pellets were fixed with 2% glutaraldehyde and 4% tannic acid overnight. Pellets were stained with 0.8% OsO_4 in PEM50 buffer for 1 hour and subsequently rinsed four times with PEM50. Another stain of 1% uranyl

acetate stain was applied for 1 hour and rinsed with DI water. Fixed and stained pellets were subsequently dehydrated with 25/50/75/100% solutions of acetone in DI water for 15 minutes each. Pellets were then embedded in resin, with resin poured into flat embedding moulds and held at 65 °C for 48 hours and cooled overnight. Plastic-embedded samples were then cut to ~ 50-nm slices with a microtome (Ted Pella, Redding, CA) and transferred to Formvar carbon-coated copper EM grids.

X-Ray Scattering and Analysis SAXS experiments were performed at beamline 4-2 of the Stanford Synchrotron Radiation Lightsource at 9 keV using a custom-made temperature-controlled sample holder. Experiments were performed at 37 °C unless otherwise noted. For the temperature ramp down experiment, initial data was taken at 37 °C. Then the temperature controller was set to 5 °C, which was reached over the course of <7 minutes. A needle temperature probe was inserted into a water-filled quartz capillary placed in the sample holder for instantaneous temperature recordings during the ramp down, approximating the apparent temperature for the samples.

Data from 2D scattering images was obtained with a Pilatus3 X 1M 2D-detector and azimuthally averaged to create 1D scattering profiles. Quantitative line-shape analysis was performed by fitting 1D scattering data to a model profile, I(q):

$$I(q) = \iint S(q_r)|F_{MT}(q_r, q_z)|^2 + \iint |F_{Ring}(q_r, q_z)|^2 + BG(q) \quad (1)$$

The first term in *I*(q) consists of the structure factor $S(q_r)$ of the bundled MT lattice multiplied by the form factor of a MT ($|F_{MT}(q_z,q_r)|^2$) and is averaged over all orientations in q-space (q_r, q_z are wavevectors perpendicular and parallel to the MT cylinder axis).

The structure factor of the bundled MT state was modeled as the sum of square Lorentzians at every 2D reciprocal lattice vector $q_{hk} = q_{10}(h^2+k^2+hk)^{1/2}$ with amplitude A_{hk} and peak width κ_{hk}:

$$S(q_r) = \sum_{h,k}[A_{hk}/(\kappa_{hk} + (q_r - q_{10}\sqrt{h^2 + k^2 + hk})^2)]^2 \quad (2)$$

The first three Bragg peaks (q_{10}, $q_{11}=3^{1/2}q_{10}$, $q_{20}=2q_{10}$) were individually fit, while all other peaks were thereafter fit simultaneously. To limit the number of fitting parameters, all simultaneously fit peaks were assumed to have the same peak width as κ_{20} (the highest-order peak that was individually fit). The center-to-center distance between microtubules is given by $a_h = 4\pi/(q_{10}\sqrt{3})$, and the coherent domain size of the MT lattice (i.e. the hexagonal bundle width) is inversely related to the width of the structure factor peaks and is given by $L_{lattice} = 2(\pi \ln 4)^{1/2}/\kappa_{10}$ [42].

The form factors (F) of both MTs and tubulin rings were calculated by modeling them each as hollow cylinders with uniform electron density [35,56], wall width set to w = 49 Å[65], and lengths fixed at L_{MT} = 20,000 Å (larger than the resolution of our wavevector) and L_{ring} = 49 Å (consistent with electron microscopy data for single tubulin rings)[56].

$$|F_{MT}|^2 \propto |[(\sin(q_z L_{MT}/2)/q_r q_z)]\left[(r_{in}+w)J_1\left(q_r(r_{in}+w)\right) - r_{in}J_1(q_r r_{in})\right]|^2 \quad (3)$$

$$\left|F_{Ring}\right|^2 = |A_{ring}[(\sin(q_z L_{Ring}/2)/q_r q_z)]\left[(r_{in}+w)J_1\left(q_r(r_{in}+w)\right) - r_{in}J_1(q_r r_{in})\right]|^2 \quad (4)$$

Here, J_1 is the Bessel function of order 1, r_{in} is the ensemble-averaged inner radius of the MT or tubulin ring in Eq. (3) and Eq. (4), respectively, and A_{ring} is the scattering amplitude of the ring state. The MT cylinder's inner radius, r_{in}, was the only fit parameter in the MT form factor. The tubulin ring inner radius and the scattering

amplitude from the tubulin ring state were the only two fit parameters for the tubulin ring form factor.

Since the first order Bessel functions of the MT form factor (J_1 terms in Eq. (3)) equal 0 for distinct values of q_r (given r_{in}), the scattering contribution from MTs (both bundled and unbundled) to the total raw scattering profile will also approach zero at these points, resulting in the deep local minima observed in the theoretical scattering from a single MT (Fig. 6A, bottom blue curve). Therefore, since scattering from all tubulin within the MT lattice is suppressed at these distinct values of q_r, the measured intensity at these points within the raw data must be almost entirely due to the scattering from unpolymerized tubulin oligomers plus the q-independent background ($|F_{Ring}|^2$ and BG(q), Eq. 1). Because of this, an approximation for the concentration of tubulin rings can be made as any increase in the concentration of tubulin rings would require the intensity of all Bessel function minima to increase by a linear amount.

The third term in Eq. (1), BG(q), was modeled simply as a two layer, unified fit function [50] at the Bessel function minima for samples at initial timepoints (t_0):

$$BG(q) = G\exp\left(\frac{-q^2R_g^2}{3}\right) + B_1\left[\frac{erf\left(\frac{qR_g}{\sqrt{6}}\right)^3}{q}\right]^{-P_1} + \exp\left(\frac{-q^2R_g^2}{3}\right)B_2q^{-P_2} + BG_0 \qquad (\mathbf{5})$$

The first term, G, is Guiner's law, the second and third terms, B_1 and B_2, are power-law scattering terms which describe the scattering at lengths where $qR_g >> 1$ and $qR_g << 1$, respectively, and the fourth term, BG_0, is a flat scattering term independent of q. Scattering from the third and fourth term in the equation above dominate the total scattering profile (I(q), Eq. 1) at very low-q (<0.005 Å^{-1}) and high-q (>0.15 Å^{-1}) respectively, and thus were individually fit within these two domains.

Fitting bounds for R_g were determined by fits of the unified scattering function to unpolymerized tau tubulin samples (with scattering contributions from minimal tubulin rings) and were fit simultaneously with the first Bragg peak, as its scattering was most prominent at this length scale (R_g = 15-20 nm). Lastly, the fitting parameters of the second term dominate the BG scattering signal for our samples between q = 0.03 - 0.09 $Å^{-1}$, and were thus determined by fitting it to the set of points measured at time t_0 where the scattering contribution of the bundled MT state to the raw data was approximately zero (i.e. at the Bessel function minima).

Transmission Electron Microscopy All data were taken at 80 kV using the JEM 1230 (JEOL) Transmission Electron Microscope at the University of California, Santa Barbara.

Calculation of R_G and Projection Domain Extensions Previously, the radius of gyration (R_G) of wild-type tau in solution was found[66,67] to scale as an unstructured protein with random coil behavior, with $R_G = 0.1927N^{0.588}$ nm, which was subsequently used to calculate $R_G^{PD} \approx$ 3.7 nm and the physical diameter $D_{Phys} = 2R_{Phys} = 2(5/3)^{1/2}R_g \approx 9.5$ nm [68] for the PD of 4RL tau. For the weakly penetrating tau-tau interaction model, D_{Phys} is doubled to account for each opposing tau PD, giving a predicted d_{w-w} of 19 nm, roughly half the d_{w-w} we observed via SAXS. Similarly, for the electrostatic zipper model that proposes complete overlap of two opposing tau molecules, the predicted d_{w-w} would just be D_{Phys}, requiring signficant extensions beyond previously reported R_G values.

3.7. References

1. A. Desai, T. J. Mitchison, Microtubule polymerization dynamics. *Annu Rev Cell Dev Biol* **13**, 83-117 (1997).
2. T. Muller-Reichert, D. Chretien, F. Severin, A. A. Hyman, Structural changes at microtubule ends accompanying GTP hydrolysis: information from a slowly hydrolyzable analogue of GTP, guanylyl (alpha,beta)methylenediphosphonate. *Proc Natl Acad Sci U S A* **95**, 3661-3666 (1998).
3. G. M. Alushin *et al.*, High-resolution microtubule structures reveal the structural transitions in alphabeta-tubulin upon GTP hydrolysis. *Cell* **157**, 1117-1129 (2014).
4. A. A. Hyman, D. Chretien, I. Arnal, R. H. Wade, Structural changes accompanying GTP hydrolysis in microtubules: information from a slowly hydrolyzable analogue guanylyl-(alpha,beta)-methylene-diphosphonate. *J Cell Biol* **128**, 117-125 (1995).
5. D. Chretien, S. D. Fuller, E. Karsenti, Structure of growing microtubule ends: two-dimensional sheets close into tubes at variable rates. *J Cell Biol* **129**, 1311-1328 (1995).
6. L. M. Rice, E. A. Montabana, D. A. Agard, The lattice as allosteric effector: structural studies of alphabeta- and gamma-tubulin clarify the role of GTP in microtubule assembly. *Proc Natl Acad Sci U S A* **105**, 5378-5383 (2008).
7. D. Bray, *Cell movements: from molecules to motility*. (Garland Science, 2000).
8. J. Chen, Y. Kanai, N. J. Cowan, N. Hirokawa, Projection domains of MAP2 and tau determine spacings between microtubules in dendrites and axons. *Nature* **360**, 674-677 (1992).
9. T. D. Pollard, W. C. Earnshaw, J. Lippincott-Schwartz, G. Johnson, *Cell biology E-book*. (Elsevier Health Sciences, 2016).
10. N. Hirokawa, S. Hisanaga, Y. Shiomura, MAP2 is a component of crossbridges between microtubules and neurofilaments in the neuronal cytoskeleton: quick-

freeze, deep-etch immunoelectron microscopy and reconstitution studies. *J Neurosci* **8**, 2769-2779 (1988).

11. M. Takeuchi, S. Hisanaga, T. Umeyama, N. Hirokawa, The 72-kDa microtubule-associated protein from porcine brain. *J Neurochem* **58**, 1510-1516 (1992).
12. C. Conde, A. Caceres, Microtubule assembly, organization and dynamics in axons and dendrites. *Nat Rev Neurosci* **10**, 319-332 (2009).
13. D. G. Drubin, S. C. Feinstein, E. M. Shooter, M. W. Kirschner, Nerve growth factor-induced neurite outgrowth in PC12 cells involves the coordinate induction of microtubule assembly and assembly-promoting factors. *J Cell Biol* **101**, 1799-1807 (1985).
14. D. G. Drubin, M. W. Kirschner, Tau protein function in living cells. *J Cell Biol* **103**, 2739-2746 (1986).
15. A. Peters, S. L. Palay, H. d. F. Webster. (Oxford University Press, 1991).
16. S. L. Palay, C. Sotelo, A. Peters, P. M. Orkand, The axon hillock and the initial segment. *J Cell Biol* **38**, 193-201 (1968).
17. M. N. Rasband, The axon initial segment and the maintenance of neuronal polarity. *Nat Rev Neurosci* **11**, 552-562 (2010).
18. X. Li *et al.*, Novel diffusion barrier for axonal retention of Tau in neurons and its failure in neurodegeneration. *EMBO J* **30**, 4825-4837 (2011).
19. D. N. Drechsel, A. A. Hyman, M. H. Cobb, M. W. Kirschner, Modulation of the dynamic instability of tubulin assembly by the microtubule-associated protein tau. *Mol Biol Cell* **3**, 1141-1154 (1992).
20. N. Gustke, B. Trinczek, J. Biernat, E. M. Mandelkow, E. Mandelkow, Domains of Tau-Protein and Interactions with Microtubules. *Biochemistry* **33**, 9511-9522 (1994).
21. D. Panda, B. L. Goode, S. C. Feinstein, L. Wilson, Kinetic stabilization of microtubule dynamics at steady state by tau and microtubule-binding domains of tau. *Biochemistry* **34**, 11117-11127 (1995).

22. B. Trinczek, J. Biernat, K. Baumann, E. M. Mandelkow, E. Mandelkow, Domains of tau protein, differential phosphorylation, and dynamic instability of microtubules. *Mol Biol Cell* **6**, 1887-1902 (1995).
23. D. Panda, J. C. Samuel, M. Massie, S. C. Feinstein, L. Wilson, Differential regulation of microtubule dynamics by three- and four-repeat tau: implications for the onset of neurodegenerative disease. *Proc Natl Acad Sci U S A* **100**, 9548-9553 (2003).
24. D. W. Cleveland, S.-Y. Hwo, M. W. Kirschner, Purification of tau, a microtubule-associated protein that induces assembly of microtubules from purified tubulin. *Journal of Molecular Biology* **116**, 207-225 (1977).
25. K. S. Kosik, C. L. Joachim, D. J. Selkoe, Microtubule-associated protein tau (tau) is a major antigenic component of paired helical filaments in Alzheimer disease. *Proc Natl Acad Sci U S A* **83**, 4044-4048 (1986).
26. M. Hutton *et al.*, Association of missense and 5'-splice-site mutations in tau with the inherited dementia FTDP-17. *Nature* **393**, 702-705 (1998).
27. A. C. McKee *et al.*, Chronic traumatic encephalopathy in athletes: progressive tauopathy after repetitive head injury. *J Neuropathol Exp Neurol* **68**, 709-735 (2009).
28. A. Himmler, D. Drechsel, M. W. Kirschner, D. W. Martin, Jr., Tau consists of a set of proteins with repeated C-terminal microtubule-binding domains and variable N-terminal domains. *Mol Cell Biol* **9**, 1381-1388 (1989).
29. K. A. Butner, M. W. Kirschner, Tau protein binds to microtubules through a flexible array of distributed weak sites. *Journal of Cell Biology* **115**, 717-730 (1991).
30. G. Lee, R. L. Neve, K. S. Kosik, The Microtubule Binding Domain of Tau-Protein. *Neuron* **2**, 1615-1624 (1989).
31. B. L. Goode, S. C. Feinstein, Identification of a novel microtubule binding and assembly domain in the developmentally regulated inter-repeat region of tau. *J Cell Biol* **124**, 769-782 (1994).

32. H. P. Miller, L. Wilson, in *Methods in Cell Biology,* L. C. J. J. Wilson, Ed. (Elsevier Inc., 2010), vol. 95, pp. 3-15.
33. P. J. Chung *et al.*, Direct force measurements reveal that protein Tau confers short-range attractions and isoform-dependent steric stabilization to microtubules. *Proc Natl Acad Sci U S A* **112**, E6416-6425 (2015).
34. R. Milo, R. Phillips, *Cell biology by the numbers*. (Garland Science, 2015).
35. P. J. Chung *et al.*, Tau mediates microtubule bundle architectures mimicking fascicles of microtubules found in the axon initial segment. *Nat Commun* **7**, 12278 (2016).
36. Y. Kanai, J. Chen, N. Hirokawa, Microtubule bundling by tau proteins in vivo: analysis of functional domains. *Embo J* **11**, 3953-3961 (1992).
37. E. H. Kellogg *et al.*, Near-atomic model of microtubule-tau interactions. *Science* **360**, 1242-1246 (2018).
38. X. H. Li, J. A. Culver, E. Rhoades, Tau Binds to Multiple Tubulin Dimers with Helical Structure. *J Am Chem Soc* **137**, 9218-9221 (2015).
39. X. H. Li, E. Rhoades, Heterogeneous Tau-Tubulin Complexes Accelerate Microtubule Polymerization. *Biophys J* **112**, 2567-2574 (2017).
40. R. L. Best *et al.*, Tau isoform-specific stabilization of intermediate states during microtubule assembly and disassembly. **294**, 12265-12280 (2019).
41. M. A. Ojeda-Lopez *et al.*, Transformation of taxol-stabilized microtubules into inverted tubulin tubules triggered by a tubulin conformation switch. *Nat Mater* **13**, 195-203 (2014).
42. M. T. Gyparaki *et al.*, Tau forms oligomeric complexes on microtubules that are distinct from tau aggregates. *Proc Natl Acad Sci U S A* **118**, (2021).
43. R. Tan *et al.*, Microtubules gate tau condensation to spatially regulate microtubule functions. *Nat Cell Biol* **21**, 1078-1085 (2019).
44. V. Siahaan *et al.*, Kinetically distinct phases of tau on microtubules regulate kinesin motors and severing enzymes. *Nat Cell Biol* **21**, 1086-1092 (2019).

45. D. J. Needleman *et al.*, Higher-order assembly of microtubules by counterions: from hexagonal bundles to living necklaces. *Proc Natl Acad Sci U S A* **101**, 16099-16103 (2004).
46. G. Beaucage, Approximations Leading to a Unified Exponential/Power-Law Approach to Small-Angle Scattering. *Journal of applied crystallography* **28**, 717-728 (1995).
47. M. C. Choi *et al.*, Human microtubule-associated-protein tau regulates the number of protofilaments in microtubules: a synchrotron x-ray scattering study. *Biophys J* **97**, 519-527 (2009).
48. J. M. Andreu *et al.*, Low resolution structure of microtubules in solution. Synchrotron X-ray scattering and electron microscopy of taxol-induced microtubules assembled from purified tubulin in comparison with glycerol and MAP-induced microtubules. *J Mol Biol* **226**, 169-184 (1992).
49. H. P. Erickson, W. A. Voter, Polycation-induced assembly of purified tubulin. *Proc Natl Acad Sci U S A* **73**, 2813-2817 (1976).
50. A. Shemesh, A. Ginsburg, Y. Levi-Kalisman, I. Ringel, U. Raviv, Structure, Assembly, and Disassembly of Tubulin Single Rings. *Biochemistry* **57**, 6153-6165 (2018).
51. A. Harada *et al.*, Altered microtubule organization in small-calibre axons of mice lacking tau protein. *Nature* **369**, 488-491 (1994).
52. P. H. S. George-Hyslop, Piecing together Alzheimer's. *Scientific American* **283**, 76-83 (2000).
53. K. J. Rosenberg, J. L. Ross, H. E. Feinstein, S. C. Feinstein, J. Israelachvili, Complementary dimerization of microtubule-associated tau protein: Implications for microtubule bundling and tau-mediated pathogenesis. *Proc Natl Acad Sci U S A* **105**, 7445-7450 (2008).
54. M. C. Choi *et al.*, Paclitaxel suppresses Tau-mediated microtubule bundling in a concentration-dependent manner. *Biochim Biophys Acta Gen Subj* **1861**, 3456-3463 (2017).

55. G. Fagherazzi, Small angle X-ray scattering edited by O. Glatter and O. Kratky. *Acta Crystallographica Section A: Foundations of Crystallography* **39**, 500-500 (1983).
56. E. Mylonas *et al.*, Domain conformation of tau protein studied by solution small-angle X-ray scattering. *Biochemistry* **47**, 10345-10353 (2008).
57. J. E. Kohn *et al.*, Random-coil behavior and the dimensions of chemically unfolded proteins. *Proc Natl Acad Sci U S A* **101**, 12491-12496 (2004).
58. M. Rubinstein, R. H. Colby, *Polymer physics*. (Oxford university press New York, 2003), vol. 23.
59. L. Dehmelt, S. Halpain, The MAP2/Tau family of microtubule-associated proteins. *Genome Biol* **6**, 204 (2005).
60. S. F. B. van Beuningen *et al.*, TRIM46 Controls Neuronal Polarity and Axon Specification by Driving the Formation of Parallel Microtubule Arrays. *Neuron* **88**, 1208-1226 (2015).
61. M. Curcio, F. Bradke, Microtubule Organization in the Axon: TRIM46 Determines the Orientation. *Neuron* **88**, 1072-1074 (2015).
62. M. Harterink *et al.*, TRIM46 Organizes Microtubule Fasciculation in the Axon Initial Segment. *J Neurosci* **39**, 4864-4873 (2019).
63. R. L. Best *et al.*, Expression and isolation of recombinant tau. *Methods Cell Biol* **141**, 3-26 (2017).
64. S. Kar, J. Fan, M. J. Smith, M. Goedert, L. A. Amos, Repeat motifs of tau bind to the insides of microtubules in the absence of taxol. *EMBO J* **22**, 70-77 (2003).
65. V. Makrides, M. R. Massie, S. C. Feinstein, J. Lew, Evidence for two distinct binding sites for tau on microtubules. *Proc Natl Acad Sci U S A* **101**, 6746-6751 (2004).

4. Temperature-induced reversible phase transitions between bundled MT and tubulin assembly states

4.1. Introduction

Microtubules are hierarchically assembled cytoskeletal protein superstructures composed of alpha-beta tubulin heterodimers. Head-to-tail stacking of tubulin dimer subunits creates polar oligomers and longer protofilaments (PFs), while parallel PFs interact laterally to form the hollow cylindrical structure of a MT[1]. The polarity and dynamics of MT assembly and disassembly provide a mechanism for functional diversification in cells that may require MTs with specific orientation, length, or stability. For example, rapid switching between MT growth and shrinkage during mitosis enables chromosome segregation[104], highly active MT remodeling in growth cones enables axon elongation[105,106], and stable MTs correctly oriented in mature axons are required for cargo transport by kinesins and dyneins[7,107]. Additional functionality is imparted on MTs by their ability to interact with one another in densely packed arrays in order to resist compressive forces on the cell or to maintain cell polarity, as in the axon initial segment of mature neurons[7]. While individual MT dynamics have been studied extensively, our understanding of bundled MTs functioning collectively is less well understood in part by a lack of fundamental knowledge on the mechanisms underlying bundle formation.

Many microtubule-associated proteins have been linked to the formation of bundled MT assemblies, but the neuronal MAP tau is of particular interest for its

involvement in neurodegenerative diseases such as Alzheimer's. Several physiological roles for tau have been reported and studied, including MT bundle formation, regulation of dynamic instability, axonal transport along MTs, and axon elongation during neuronal development. Localization of tau to the axonal compartment is essential for healthy neurons and is maintained in part by a retrograde diffusion barrier at the AIS, implicating a possible connection between the organized microtubule arrays of the AIS and the physiological role of tau. Further substantiating this model is tau's known ability to mediate inter-microtubule interactions in the formation and stabilization of microtubule bundles.

Despite a history of a contradicting reports on tau's role in mediating microtubule bundles, recent work with cell-free tau-tubulin reaction mixtures has reconciled many inconsistent findings. Specifically, the cancer chemotherapy agent paclitaxel was frequently used to stabilize microtubules against depolymerization, thus severely suppressing free tubulin content and preveningt microtubule bundle formation. Similarly, results discussed by Kohl *et al* provide a model for paclitaxel's suppression of tau-mediated bundle formation, whereby tau itself is not sufficient to bundle microtubules but relies on free tubulin (not within the MT lattice) to form a protein network that permeates the microtubule ensemble, cross-linking neighboring MTs. This work showed that increasing the free tubulin content within reaction mixtures by depolymerizing MTs, either with excess divalent cations or by reducing temperatures, was sufficient to increase the average bundle domain size and decrease the spacing between bundled MTs, despite rapid MT depolymerization. Increased bundle domain size coincided with a change to the MT depolymerization

products from the slow formation of low-curvature tubulin oligomers to the sudden onset of rapid inverted tubulin ring formation. They describe this cation- and temperature-driven phenomenon as phase transition from the previously reported widely spaced microtubule bundle state to the inverted tubulin ring state, mediated by a transient bundled microtubule state, which coexists with tubulin rings before completely depolymerizing.

Building on these experiments, we show here that the previously described temperature-driven phase transition occurs below critical temperatures, and that critical temperature increases with increased Ca^{2+} ion content. To eliminate the potential effect of time-dependent GTP hydrolysis in our reaction mixtures, experiments were designed to rapidly reduce temperature and test the phase stability over a range of Mg^{2+} and Ca^{2+} concentrations and with several isoforms of tau. These experiments reproduce the finding that Ca^{2+} enhances susceptibility of bundled MTs to temperature-driven phase transition, and, moreover, demonstrate the complete reversibility of the phase transition across all Mg^{2+} concentrations tested.

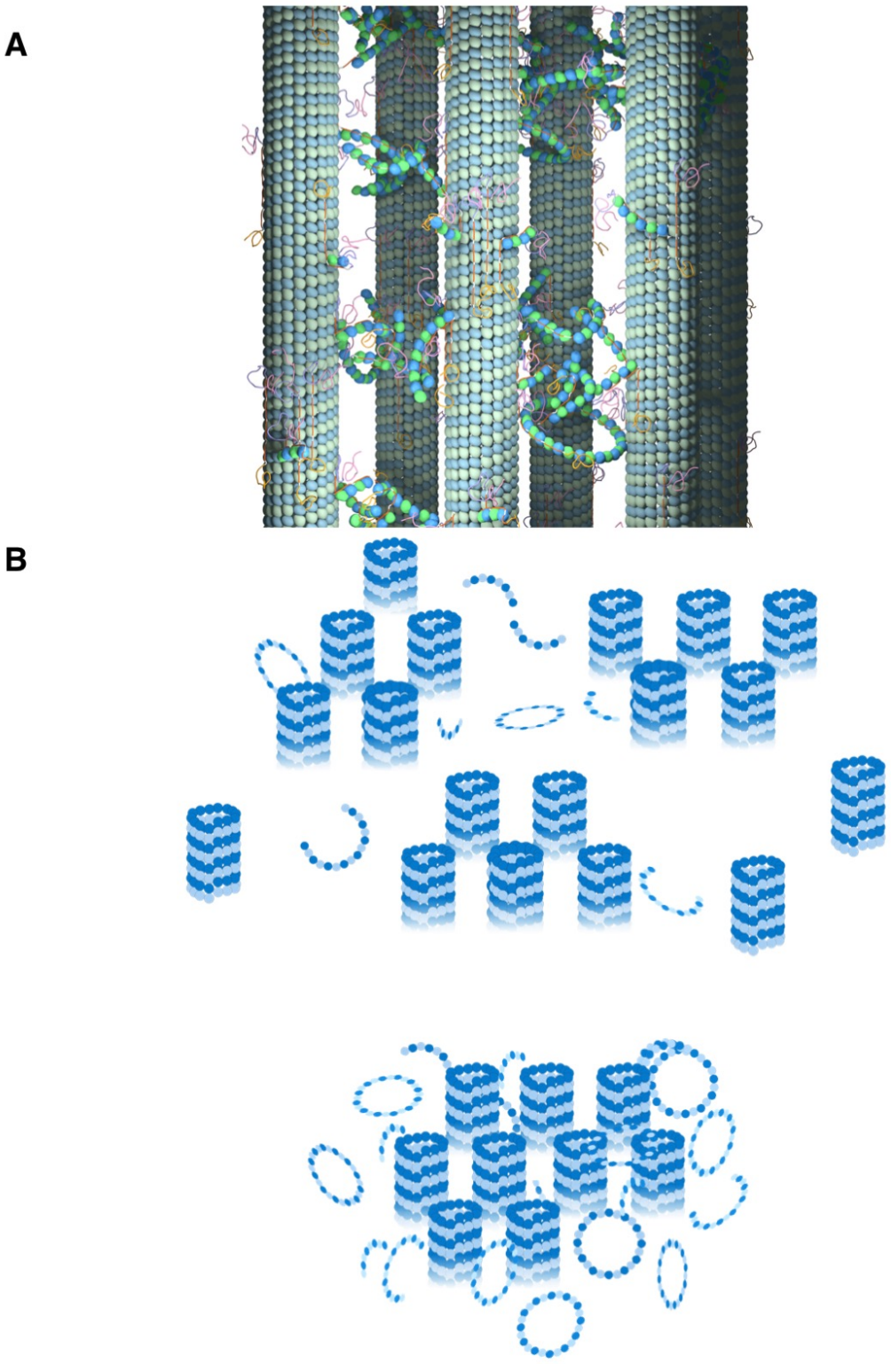

Figure 4.1

Figure 4.1: Network of cross-linked tubulin oligomers and tau dictates microtubule bundle configuration (**A**) Tau forms a gel-like network between bundled MTs by mediating interactions between tubulin in solution and tubulin incorporated into the MT lattice. This intervening network of proteins stabilizes hexagonally packed bundles of MTs. (**B**) Rapid MT depolymerization decreases the mass fraction of tubulin incorporated into MTs, increasing the content of tubulin oligomers and rings incorporated in the intervening network. The increased density of proteins within the network causes a phase transition in the remaining microtubules by strengthening interactions between MTs, resulting in fewer bundles of more tightly packed MTs. This intermediate bundling state precedes the complete depolymerization of MTs in favor of depolymerized rings and oligomers.

4.2. Reduced temperature induces phase transition from B_{ws} to tubulin rings, mediated by B_{int}

Time-dependent synchrotron SAXS measurements were performed on dynamic tubulin reaction mixtures containing 2 mM GTP and full-length (4RL) tau at tau/tubulin-heterodimer ratio of 1:20. Reaction mixtures were prepared by combining all components on ice and then incubating at 37 °C for 30 minutes for polymerization to reach a steady sate. Subsequently, reaction mixtures were transferred to quartz capillaries and centrifuged at 37 °C for 30 minutes to maximize scattering intensity for SAXS measurements. Capillaries were sealed with epoxy and loaded into a custom-made, temperature-controlled sample holder for SAXS measurements. Data was taken every 15 minutes, while the temperature of the sample holder was gradually reduced from 37 °C at initial timepoints (referred to as t_0, which is the first time point at which data is collected, approximately 10 minutes after centrifugation) to 5 °C after 5 hours. The apparent temperature of the reaction mixtures was estimated at each time-point by measuring the water temperature in a control capillary within the sample holder. Scattering profiles were generated by exposing the centrifuged reaction mixture pellets to the x-ray beam for 1 second and recording the resulting pattern with a 2D detector. These 2D images were azimuthally averaged to produce 1D scattering profiles.

At initial timepoints, scattering from microtubule reaction mixtures prepared with up to 2.0 mM $MgCl_2$ added to standard buffer indicated strong MT polymerization and 2D hexagonal packing of MTs, similar to the previously reported

wide-spacing bundled state (B_{ws}). Line-shape analysis revealed wall-to-wall distances (D_{w-w}) between MTs in the B_{ws} state that were consistent with previous reports and increased gradually over time due to relaxation from centrifugation. Above threshold temperatures all samples reproduce the time-dependent characteristics of the B_{ws} state previously reported. Namely, scattering from MT form factor gradually decreased over time, indicating gradual MT depolymerization over time in favor of soluble "free" tubulin oligomers of various size and curvature. However, below critical temperatures (T_c = 25 °C), changes to the scattering profiles indicated a sudden phase transition from the B_{ws} state to the more tightly packed intermediate bundled state (B_{int}), signified by the simultaneous and rapid increase in MT depolymerization and tubulin ring formation, with the sharp drop in D_{w-w}.

These structural changes are revealed by a reduced Bragg peak width and a shift in all hexagonal lattice peaks to lower q values, indicating that the coherent domain size of the bundle lattice is larger and that D_{w-w} is significantly lowered, respectively. Another key feature of the B_{int} state is the stability of D_{w-w} over time, in contrast to the slow expansion of MT bundles in the B_{ws} state. Despite the reduced lifetime of the B_{ws} and B_{int} due to temperature changes in these experiments, the wall-to-wall distance of B_{int} remains relatively stable until scattering from the tubulin ring state dominates at low temperatures.

For each $MgCl_2$ concentration tested, all three structural phases were observed, starting with wide-spacing MT bundles at initial time points (high temperatures), the intermediate bundled state at intermediate timepoints (below T_c), and the tubulin ring state at late timepoints (5 °C).

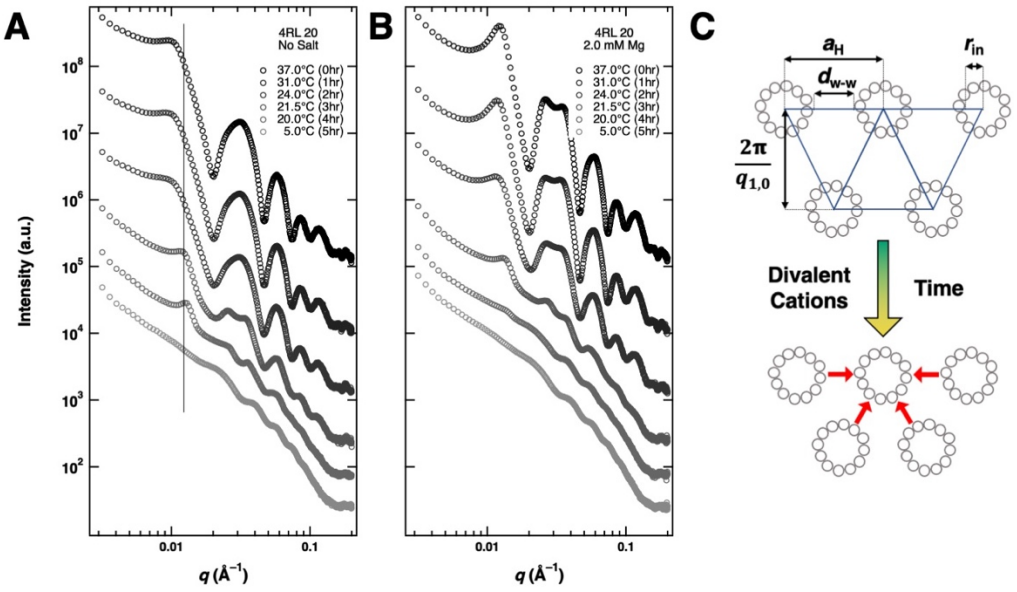

Figure 4.2: Time-dependent synchrotron SAXS data reveals that the temperature for MT bundle phase transition is not strongly dependent on Mg concentration (**A**) Time-dependent SAXS data for one sample prepared in standard polymerization buffer (left) and one in standard polymerization buffer plus 1.2 mM $MgCl_2$ (right). At early time points (0, 1, and 2 hours), MT remain in the previously reported wide-spacing bundled state, despite gradually decreasing the temperature over time. Below critical temperatures, the location of the 1,0 hexagonal lattice peak shifts to higher q and scattering intensity rapidly increases at all local minima produced from the MT form factor. These changes to the scattering profiles are indicative of the previously described phase transition to the intermediate bundling state and occur at 24, 21, 23, and 24 °C for 0.0, 0.4, 1.2, and 2.0 mM $MgCl_2$ added to the polymerization buffer, respectively. Scattering from tubulin rings dominates at lower temperatures.

While the critical temperature for transitioning from the wide-spacing state to the intermediate state was not strongly dependent on the concentration of added $MgCl_2$, reaction mixtures prepared in parallel but with added $CaCl_2$ instead of $MgCl_2$ exhibited higher T_c with increasing $CaCl_2$ content. Figure 3 shows time dependent SAXS profiles of samples with 0.4 mM $CaCl_2$ (a) and 1.6 mM $CaCl_2$ (b), where at t_0, both samples are in the B_{ws} state but the transition to the B_{int} state occurs above 31 °C in the latter, only an hour into the experiment. A phase diagram showing divalent cation content vs transition temperature was generated by plotting the first data point at which the onset of transition was observed via SAXS.

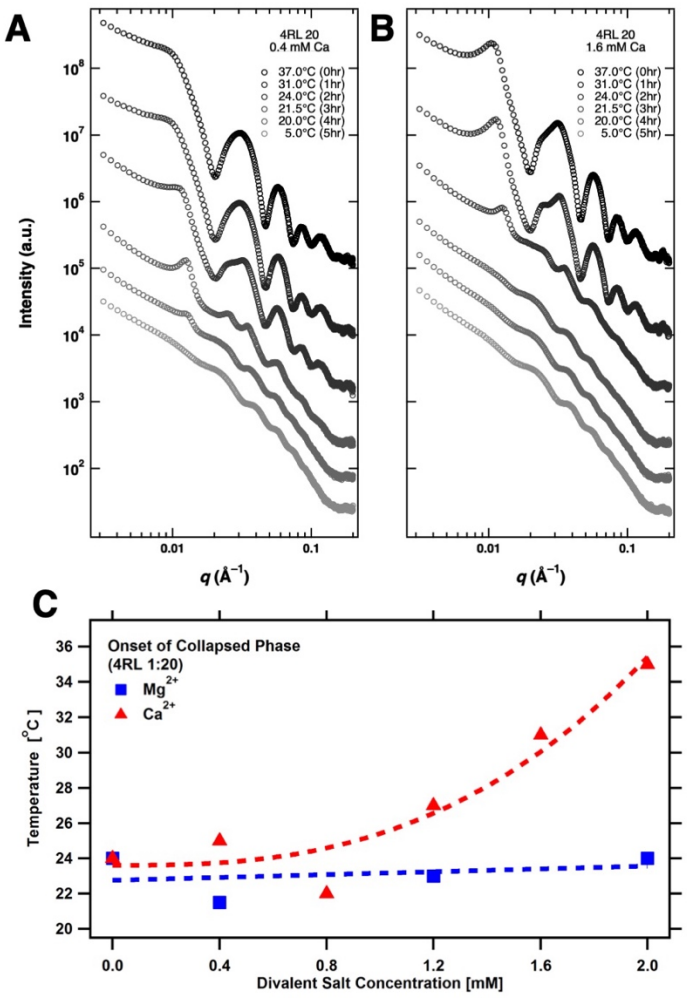

Figure 4.3: Calcium increases the critical temperature for Bws to Bint phase transition (**A**) Time-dependent SAXS data reveals that the critical temperature for phase transition increases with increased $CaCl_2$ in reaction mixtures. (**B**) Phase diagram for Mg^{2+} and Ca^{2+} SAXS data plotted in Figure 2 and in part (A), respectively.

Following the 5-hour temperature drop and data collection, the temperature of the sample holder was then increased back to 37 °C, with scattering measurements taken at the same time- and temperature-steps used during cooling. Re-polymerization of MTs was only observed for one sample (0.8 mM $CaCl_2$), while scattering profiles from all other reaction mixtures gradually changed from soluble to aggregated tubulin rings.

4.3. Reversibility of temperature-induced phase transition

While the phase diagram generated from the experiments above provide a baseline for understanding the critical temperature for inducing the bundled phase transition, we sought to eliminate the effects of time and GTP hydrolysis by dropping the sample temperature as quickly as possible. To do this, time-dependent SAXS experiments were performed on tau-tubulin reaction mixtures prepared as described above. X-ray data was collected at the earliest timepoint (t_0) following sample preparation and every ten minutes following t_0. The sample temperature was cycled from 37 °C to 21 °C (the lowest T_c observed above) at t_0 + 30 minutes, and then back up to 37 °C at t_0 + 70 minutes (plotted in Figure 4C, bottom). Using the phase diagram in Figure 1 as a guide, 21 °C was chosen to maximize the possibility of observing the transition while it was occurring.

Figure 4A shows a time sequence of SAXS profiles (open circles), corresponding fits to the total scattering (solid colored lines), background (dashed line), and background + scattering from tubulin rings (dotted lines) for a sample prepared with 4RL tau and no $MgCl_2$ added to standard PIPES buffer (total $[Mg^{2+}]$ =

1 mM). The scattering features of these profiles at each stage of the experiment are representative of all of the data collected for samples prepared with 4RL tau and added $MgCl_2$, and separating the fit lines highlights changes to the tubulin structural states that occur as the temperature is cycled on a short time-scale. Before the change in temperature, samples reproduced the scattering features of the B_{ws} state. Namely, Bragg peaks indicate strong MT polymerization, widely-spaced hexagonal bundles of MTs, and minimal scattering from tubulin rings. However, immediately following the change in temperature from 37 °C to 21 °C (t_0 + 40 minutes), the 1,0-scattering peak abruptly shifted to higher q, and scattering from tubulin rings sharply increased, indicating that the temperature-induced phase transition from the B_{ws} state to the B_{int} state is reproduced even on short timescales. Upon increasing the temperature back to 37 °C, scattering from tubulin rings is reduced, and the 1,0 hexagonal lattice peak shifts back to lower q, indicating a reversal of the phase transition between B_{ws} and B_{int}.

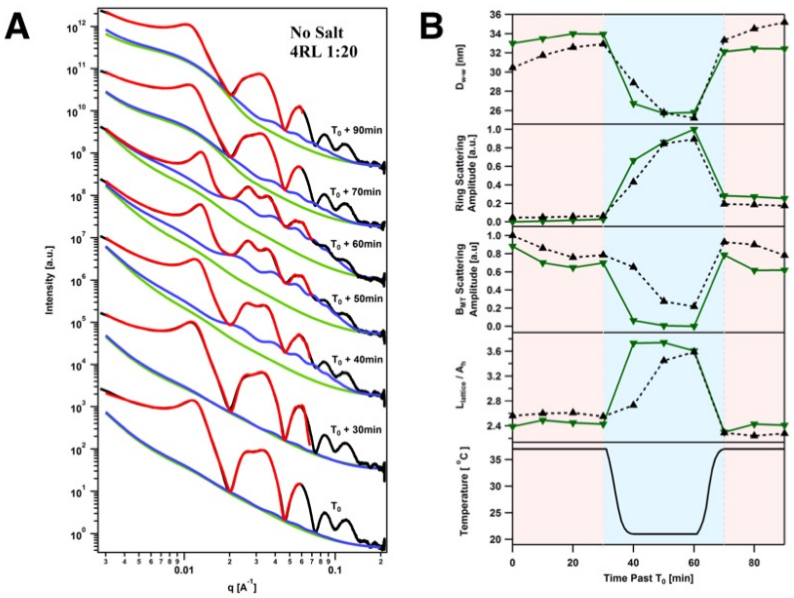

Figure 4.4: Temperature-induced phase transitions between the wide-spacing and intermediate bundle states are reversible (**A**) Fit parameters plotted as a function of time demonstrate the correlation between the temperature (bottom), the mass fraction of bundled MTs and tubulin rings (middle), and the wall-to-wall spacing (top) of bundled MTs for 0 (black triangles) and 1.2 mM $MgCl_2$ (green triangles). (**B**) Time-dependent SAXS data (open circles, offset for clarity) and corresponding fits to the data (solid lines) for 0 mM $MgCl_2$ added to the standard polymerization buffer shown for selected time points from the plotted fit parameters in (A). The full scattering profile fits (red) include fits to the background scattering (green) and fits to the scattering from tubulin rings (shown as background + ring scattering, blue). Separating the fit lines for each SAXS exposure shows that the reversibility of the phase transition includes both the re-organization of the bundled MTs back to larger Dw-w and a reduction in scattering from tubulin rings. FIGURE IS UNFINISHED AND INACCURATE. DATA SHOWN IS WITH CaCl2 AND NOT MgCl2. UPDATE COMING SOON

Detailed line-shape analysis of the scattering profiles from all samples prepared with 4RL tau and $MgCl_2$ added to buffer reveals that the phase transition from the B_{ws} to the B_{int} state always occurred before the first low-temperature data point could be collected (t_0 + 40 always shows B_{int}) and is reversible for all $MgCl_2$ concentrations tested, up to 2.0 mM $MgCl_2$. Fitting parameters produced from scattering profiles of these reaction mixtures are shown as a function of time in Figure 4B and highlight the strong correlation between the change in temperature (bottom) and the simultaneous changes in D_{w-w}, microtubule bundle lattice parameter, and the scattering contributions from bundled MTs and tubulin rings.

These experiments were repeated with the 4RS isoform tau, which lacks the N-1 and N-2 inserts encoded by exons 2 and 3 of the MAPT gene and has a more positive overall electrostatic charge than 4RL tau. In contrast to the samples prepared with 4RL tau, samples prepared with 4RS responded to temperature changes slowly. Figure 5 shows the time-dependent sequence of SAXS profiles for samples prepared with 4RL tau and either no added $MgCl_2$ (A) or 2.0 mM $MgCl_2$ added (B), as well as a reaction mixture prepared with 4RS tau and 1.2 mM $MgCl_2$ added (C). Scattering profiles of all three samples at initial timepoints are consistent with the B_{ws} state, whereas only the 4RL samples have transitioned to the B_{int} state at t_0 + 40 minutes. Transition to the B_{int} state appeared to be delayed in samples prepared with 4RS tau and up to 1.2 mM added $MgCl_2$, but the reversibility of the phase transition upon increasing the temperature back up to 37 °C occurred as quickly for samples prepared with 4RS as those prepared with 4RL tau. For reaction mixtures prepared with either tau isoform in the presence of added $MgCl_2$, complete MT

depolymerization (tubulin ring state) was never observed within the 40 minute low-temperature incubation, despite significant MT depolymerization and tubulin ring formation, and all samples experienced a reversal of the phase transition upon re-introduction to higher temperature, as indicated by the expansion of $D_{w\text{-}w}$ back to pre-transition spacings, the drop in scattering from tubulin rings, and the increased scattering from bundled MTs at later timepoints.

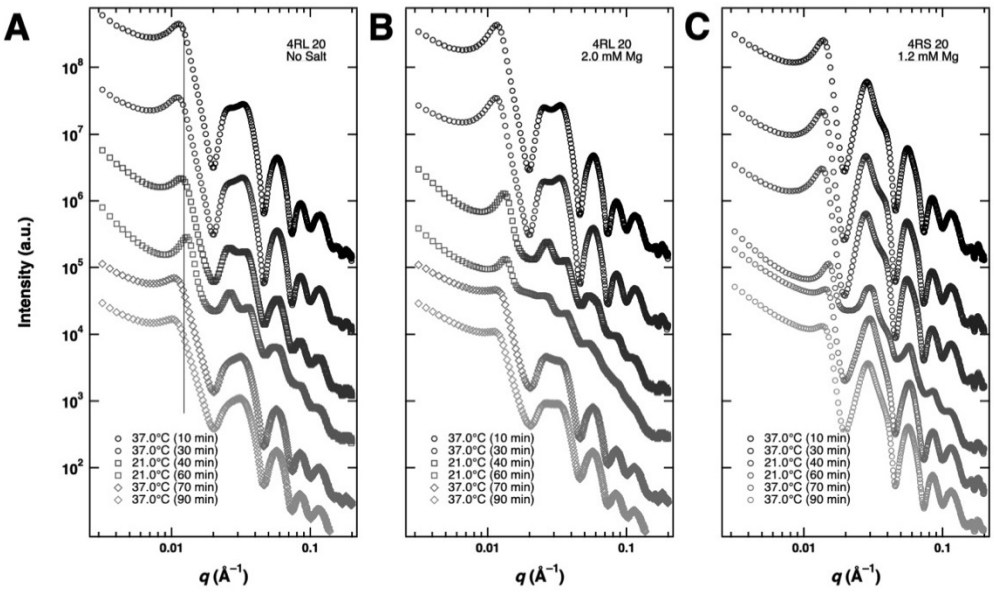

Figure 4.5: Temperature-induced bundle phase transitions are reversible for 4RL and 4RS tau Time-dependent SAXS data for samples prepared in the presence of increasing $MgCl_2$ added to the buffer with either 4RL or 4RS tau. The phase transition from the wide-spacing to intermediate bundled states, as well as the reversibility of this phase transition, was observed for both isoforms of tau at all Mg concentrations tested (up to 1.2 mM $MgCl_2$ for 4RS and up to 2.0 mM $MgCl_2$ added for 4RL).

These short-timescale, temperature cycling experiments were repeated with samples prepared with and without $CaCl_2$ added to the standard PIPES buffer ($[Mg^{2+}]_{total}$ = 1 mM). Figure 6 shows the scattering profiles for reaction mixtures prepared with 4RL tau and 1.2 mM $CaCl_2$ (A) and 2.0 mM $CaCl_2$ (B) added as well as 4RS tau with 1.2 mM $CaCl_2$ added. High $CaCl_2$ content appears to suppress reversibility of the phase transition, as is seen in the plots of 2.0 mM $CaCl_2$ with 4RL and 1.2 mM $CaCl_2$ with 4RS tau.

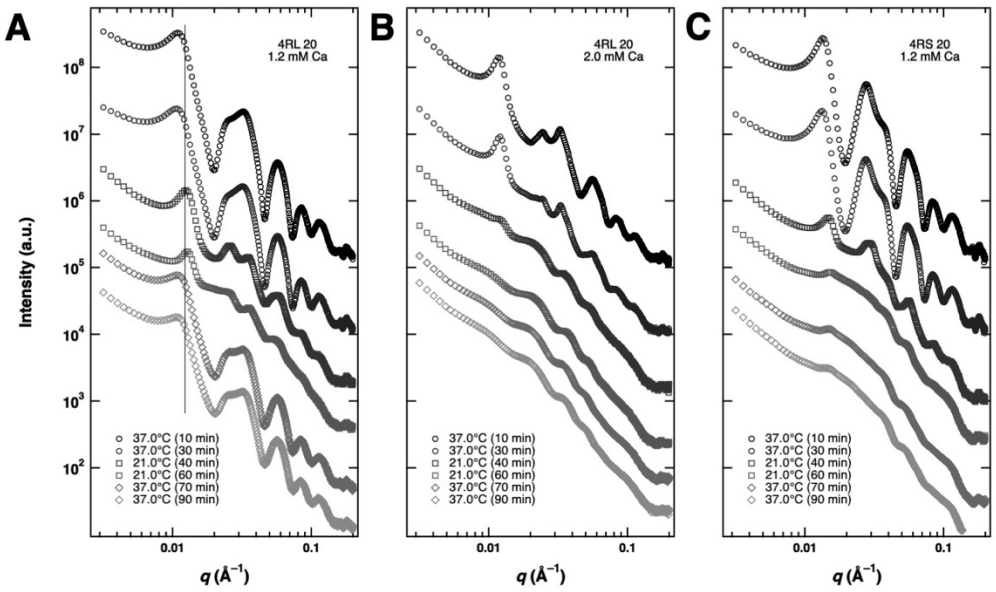

Figure 4.6: Ca inhibits the reversibility of temperature-induced bundle phase transitions for 4RL and 4RS tau Time-dependent SAXS data for samples prepared in the presence of increasing $CaCl_2$ added to the buffer with either 4RL or 4RS tau. The phase transition from the wide-spacing to intermediate bundled states was observed for both isoforms of tau at all $CaCl_2$ concentrations tested (up to 1.2 mM $MgCl_2$ for 4RS and up to 2.0 mM $MgCl_2$ added for 4RL). Reversibility of the phase transition was not observed at 2.0 mM Ca^{2+} and 1.2 mM $CaCl_2$ for 4RL and 4RS, respectively.

4.4. Methods

Tubulin and Tau Purification Following standard procedures, tubulin was purified from bovine brain and filtered into PEM 50 buffer containing 50 mM PIPES, 1 mM $MgSO_4$, 1 mM EGTA, and 0.1 mM GTP, pH 6.8 with ≈ 75 mM NaOH, and drop frozen into liquid nitrogen. Crude brain extract (CBE) was twice cycled through the following polymerization and wash steps. First, CBE was polymerized at 30 °C in glycerol-free PIPES buffer (2.5 mM GTP, 1 mM DTT, 100 mM sodium glutamate, 20 mM sodium phosphate, 1 mM EGTA, and 0.5 mM MgCl2, pH 6.85), then centrifuged at 45,000 x *g*, and separated from the supernatant. Pelleted protein mixtures were resuspended in PIPES buffer and homogenized on ice. Following two polymerization and wash cycles, resultant MAP-rich microtubule mixtures were resuspended in PEM50 and separated into MAPs and tubulin through a phosphocellulose cationic exchange column, with final tubulin concentration between 7 and 14 mg/mL as measured by Braford assay using BSA as a standard.

As previously reported, tau was expressed in BL21(DE3) pLacI cells (Invitrogen) with 18 hour incubation in 250 mL of LB media (10 g of tryptone, 5 g of yeast extract, and 10 g of NaCl per liter of DI water) and subsequently incubated for 24 hours in 6 L of auto-induction media (10 g of tryptone, 5 g of yeast extract, 0.5 g of dextrose, 2 g of α-D-lactose and 5 mL of glycerol per liter of 25mM $NaHPO_4$, 25 mM KH_2PO_4, 50 mM NH_4Cl, 5 mM Na_2SO_4 in DI water). Bacteria were harvested by centrifugation in a Sorvall RC-5B Plus centrifuge at 5000 RPM for 10 minutes maintained between 4 °C and 10 °C. Bacteria were resuspended in BRB80 buffer (80 mM PIPES, 1 mM EGTA and 1 mM $MgSO_4$) pH 6.8 with ≈ 120 mM NaOH, total 1:1

ion equivalent of 160 mM, Debye length, $\lambda_D \approx 7.6$ Å) and passed through a French pressure cell three times at >900 PSI for lysing. Lysates were then boiled for 10 min and subsequently centrifuged at 10,000 RPM for 10 minutes. Supernatants were fractionated via phosphocellulose anionic exchange column and eluted with increasing concentration of $(NH_4)_2SO_4$ (up to 1 M) in BRB80. Fractions containing tau were pooled, and dry $(NH_4)_2SO_4$ was added to 1.25M. Further purification was achieved using hydrophobic interaction column chromatography (HisTrap Phenyl HP, GE Healthcare), eluting with decreasing concentration of $(NH_4)_2SO_4$ in BRB80. Pure tau fractions were pooled, then concentrated and buffer-exchanged into BRB80 by successive centrifugation cycles using Amicon Ultra-15 Centrifugal Units with MWCO = 10,000 (EMD Millipore, Darmstadt, Germany). Purified tau were stored at -80 °C until needed for experiments. Concentration was determined by SDS-PAGE comparison with a tau mass standard, the concentration of which had been established by protein mass spectrometry and stored at – 80 °C in BRB80 (80 mM PIPES, 1 mM EGTA, 1 mM $MgCl_2$, pH 6.8 with ≈ 120 mM NaOH, total 1:1 ion equivalent of 160 mM, Debye length, $\lambda_D \approx 7.6$ Å).

Sample Preparation Reaction mixtures were prepared on ice in PEM50 buffer (50 mM PIPES, 1 mM EGTA, 1 mM $MgCl_2$, pH 6.8 with ≈ 75 mM NaOH, $\lambda_D \approx 9.6$ Å), by sequentially adding the following components to PEM50 and mixing between each step: purified tubulin (92 uM stock), GTP in PEM50 (100 mM stock), tau (37 uM stock in BRB80), and < 10uL of PEM50 buffer containing additional $MgCl_2$ or $CaCl_2$ content (5 – 50 mM stocks). Final reaction mixture volume was held at 50 uL and

contained 4.0 mg/mL tubulin. Reaction mixtures were polymerized at 37 °C for 30 minutes, then prepared for experiments as follows.

Immediately following polymerization, total reaction mixture volumes were loaded directly into 1.5-mm diameter quartz capillaries (Hilgenberg GmbH, Malsfeld, Germany) and subsequently centrifuged in a capillary rotor in a Universal 320R centrifuge (Hettich, Kirchlengern, Germany) at 9,500 x *g* and 37 °C for 30 minutes to form protein-dense pellets suitable for SAXS. Following centrifugation, pelleted capillaries were sealed with epoxy and transferred to a custom-made, temperature-controlled sample holder for data acquisition.

X-Ray Scattering and Analysis SAXS experiments were performed at beamline 4-2 of the Stanford Synchrotron Radiation Lightsource at 9 keV using a custom-made temperature-controlled sample holder. Experiments were performed at 37 °C unless otherwise noted. For the temperature ramp down experiment, initial data was taken at 37 °C. Then the temperature controller was set to 5 °C, which was reached over the course of <7 minutes. A needle temperature probe was inserted into a water-filled quartz capillary placed in the sample holder for instantaneous temperature recordings during the ramp down, approximating the apparent temperature for the samples.

Data from 2D scattering images was obtained with a Pilatus3 X 1M 2D-detector and azimuthally averaged to create 1D scattering profiles. Quantitative line-shape analysis was performed by fitting 1D scattering data to a model profile, I(q):

$$I(q) = \iint S(q_r)|F_{MT}(q_r, q_z)|^2 + \iint |F_{Ring}(q_r, q_z)|^2 + BG(q) \quad (\mathbf{1})$$

The first term in $I(q)$ consists of the structure factor $S(q_r)$ of the bundled MT lattice multiplied by the form factor of a MT ($|F_{MT}(q_z,q_r)|^2$) and is averaged over all orientations in q-space (q_r, q_z are wavevectors perpendicular and parallel to the MT cylinder axis). The structure factor of the bundled MT state was modeled as the sum of square Lorentzians at every 2D reciprocal lattice vector $q_{hk} = q_{10}(h^2+k^2+hk)^{1/2}$ with amplitude A_{hk} and peak width κ_{hk}:

$$S(q_r) = \sum_{h,k}[A_{hk}/(\kappa_{hk} + (q_r - q_{10}\sqrt{h^2+k^2+hk})^2)]^2 \quad (2)$$

The first three Bragg peaks (q_{10}, $q_{11}=3^{1/2}q_{10}$, $q_{20}=2q_{10}$) were individually fit, while all other peaks were thereafter fit simultaneously. To limit the number of fitting parameters, all simultaneously fit peaks were assumed to have the same peak width as κ_{20} (the highest-order peak that was individually fit). The center-to-center distance between microtubules is given by $a_h = 4\pi/(q_{10}\sqrt{3})$, and the coherent domain size of the MT lattice (i.e. the hexagonal bundle width) is inversely related to the width of the structure factor peaks and is given by $L_{domain} = 2(\pi \ln 4)^{1/2}/\kappa_{10}$).

The form factors (F) of both MTs and tubulin rings were calculated by modeling them each as hollow cylinders with uniform electron density, wall width set to w = 49 Å, and lengths fixed at L_{MT} = 20,000 Å (larger than the resolution of our wavevector) and L_{ring} = 49 Å (consistent with electron microscopy data for single tubulin rings).

$$|F_{MT}|^2 \propto |[(\sin(q_z L_{MT}/2)/q_r q_z)]\left[(r_{in}+w)J_1\left(q_r(r_{in}+w)\right) - r_{in}J_1(q_r r_{in})\right]|^2 \quad (3)$$

$$\left|F_{Ring}\right|^2 = |A_{ring}[(\sin(q_z L_{Ring}/2)/q_r q_z)]\left[(r_{in}+w)J_1\left(q_r(r_{in}+w)\right) - r_{in}J_1(q_r r_{in})\right]|^2 \quad (4)$$

Here, J_1 is the Bessel function of order 1, r_{in} is the ensemble-averaged inner radius of the MT, in Eq. (3), or the ring, in Eq. (4), and A_{ring} is the scattering amplitude of the ring state. The MT cylinder's inner radius, r_{in}, was the only fit parameter in the MT form factor. The tubulin ring inner radius and the scattering amplitude from the tubulin ring state were the only two fit parameters for the tubulin ring form factor.

Since the first order Bessel functions of the MT form factor (J_1 terms in Eq. (3)) equal 0 for distinct values of q_r (given r_{in}), the scattering contribution from MTs (both bundled and unbundled) to the total raw scattering profile will also approach zero at these points, resulting in the deep local minima observed in the theoretical scattering from a single MT (Fig. 6A, bottom blue curve). Therefore, since scattering from all tubulin within the MT lattice is suppressed at these distinct values of q_r, the measured intensity at these points within the raw data must be almost entirely due to the scattering from unpolymerized tubulin oligomers plus the q-independent background ($|F_{Ring}|^2$ and BG(q), Eq. 1).

The third term in Eq. (1), BG(q), was modeled simply as a two layer, unified fit function at the Bessel function minima for samples at initial timepoints (t_0):

$$BG(q) = G\exp\left(\frac{-q^2R_g^2}{3}\right) + B_1\left[\frac{erf\left(\frac{qR_g}{\sqrt{6}}\right)^3}{q}\right]^{-P_1} + \exp\left(\frac{-q^2R_g^2}{3}\right)B_2q^{-P_2} + BG_0 \qquad (\mathbf{5})$$

The first term, G, is Guiner's law, the second and third terms, B_1 and B_2, are power-law scattering terms which describe the scattering at lengths where $qR_g >> 1$ and $qR_g << 1$, respectively, and the fourth term, BG_0, is a flat scattering term independent of q. Scattering from the third and fourth term in the equation above dominate the total scattering profile (I(q), Eq. 1) at very low-q (<0.005 Å $^{-1}$) and high-q (>0.15 Å $^{-1}$)

respectively, and thus were individually fit within these two domains. Fitting bounds for R_g were determined by fits of the unified scattering function to unpolymerized tau tubulin samples (with scattering contributions from minimal tubulin rings) and were fit simultaneously with the first Bragg peak, as its scattering was most prominent at this length scale (R_g = 15-20 nm). Lastly, the fitting parameters of the second term dominate the BG scattering signal for our samples between q = 0.03 - 0.09 $Å^{-1}$, and were thus determined by fitting it to the set of points measured at time t_0 where the scattering contribution of the bundled MT state to the raw data was approximately zero (i.e. at the Bessel function minima).

A Supplementary information for Chapter 3

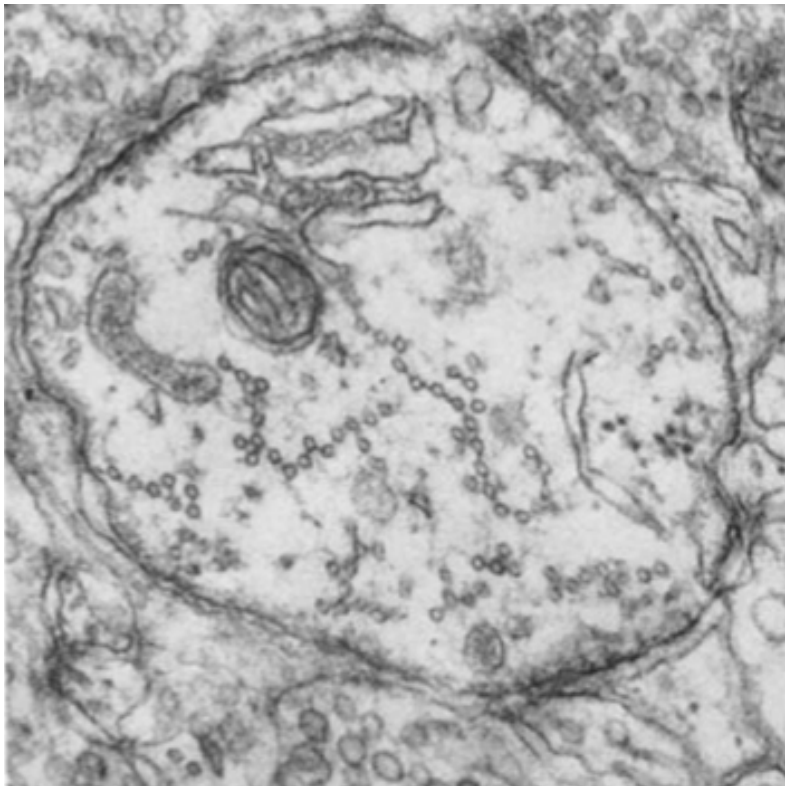

Supplemental Figure 3.1: Prior electron microscopy revealed linear microtubule bundles (microtubule fascicles) in vivo in the axon initial segment Linear microtubule bundles in the axon initial segment viewed in a transverse section of rat cerebral cortex. X 50,000. Adapted from (1), Fig. 6.

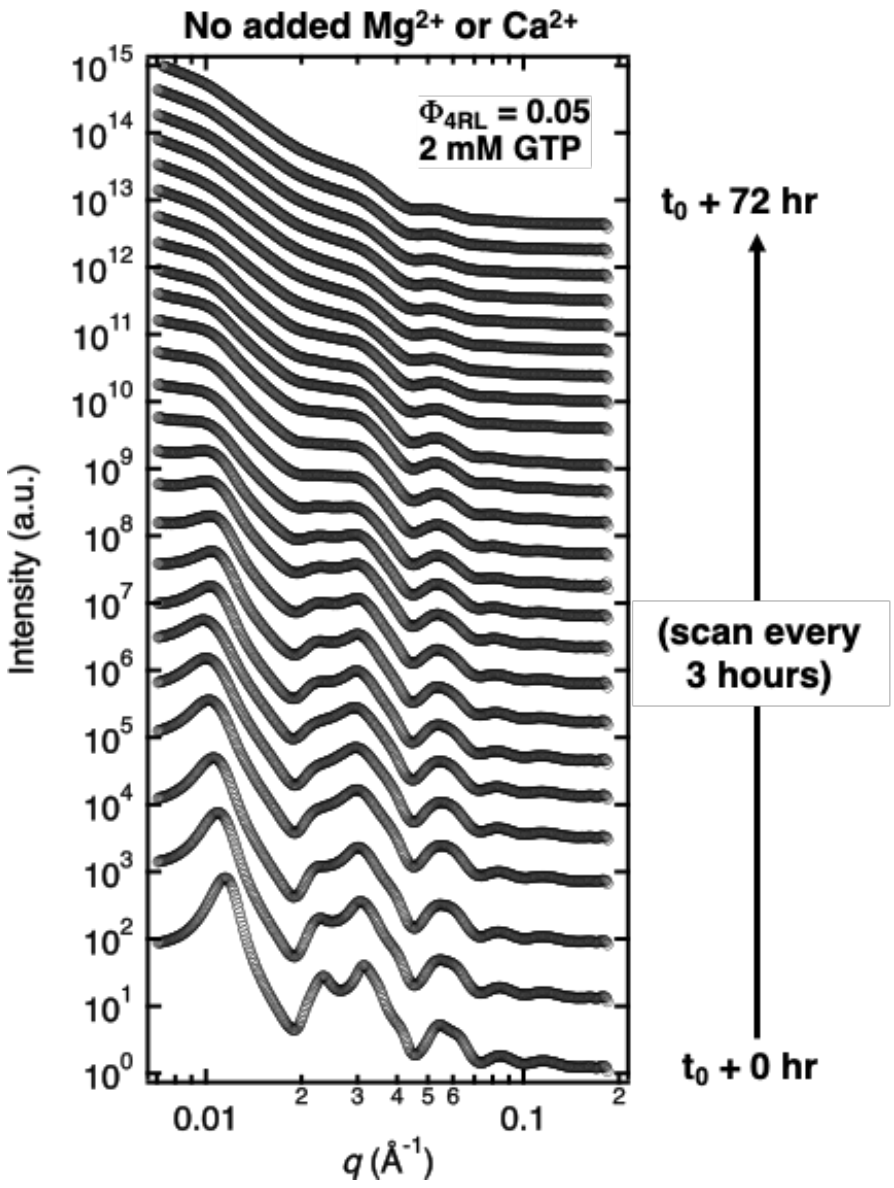

Supplemental Figure 3.2: Time- dependent synchrotron SAXS data reveals the stability of the wide-spacing (B_{ws}) microtubule bundle state in the absence of added divalent cations SAXS profiles are of tubulin/tau/GTP mixtures at 37°C and 4RL-tau to tubulin-dimer molar ratio Φ_{4RL} = 0.05. t_0 corresponds to the short time point after sample preparation when the initial SAXS measurement was performed. Azimuthally averaged synchrotron SAXS data (open circles) with increasing time. SAXS scans are offset for clarity. The B_{ws} was stable over the duration of the experiment (72 hours) and only shows a slow broadening and decrease in intensity of the peaks with increasing time due to ongoing suppressed MT dynamic instability in the presence of tau. Despite gradual MT depolymerization over time, scattering from tubulin rings is absent at all time points.

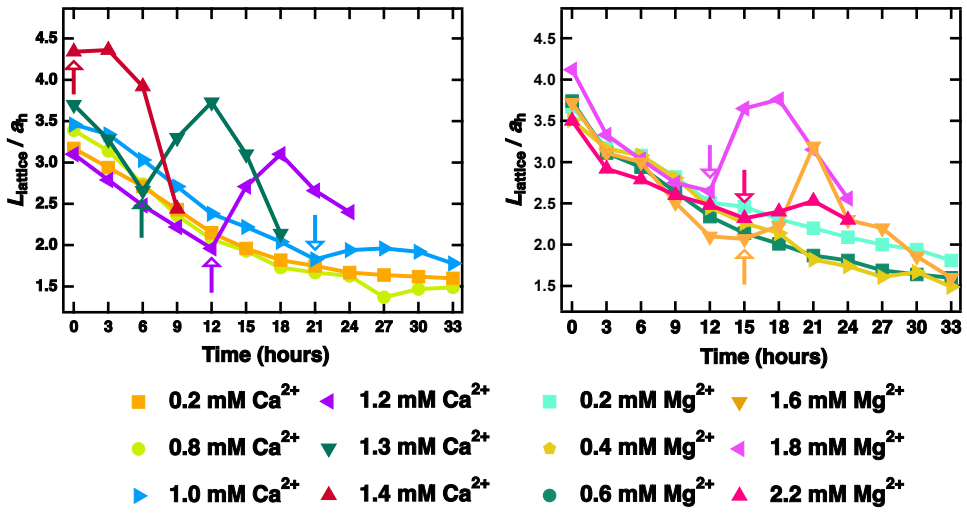

Supplemental Figure 3.3: Change in the average domain size of the hexagonal lattice, upon transitioning from the wide-spacing (B_{ws}) to the intermediate (B_{int}) MT bundle state Time "0" on the x-axis corresponds to the short time point before SAXS data was taken right after sample preparation (referred to as t_0 in figures 2,3). Plots of fitted domain size (L_{domain}) normalized by the lattice parameter (a_h) as a function of time for the SAXS data shown in figures 2 and 3 for the Ca^{2+} (left) and Mg^{2+} (right) series, respectively. Some data points omitted for clarity. Arrows indicate the latest time point the wide-spacing (B_{ws}) state is observed as the sample transitions to the intermediate B_{int} state and domain sizes increase.

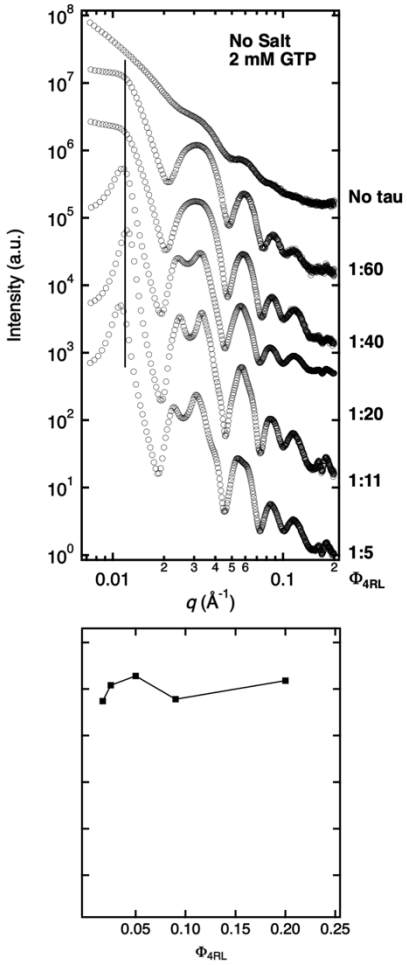

Supplemental Figure 3.4: Synchrotron SAXS data reveal the wall-to-wall distance of bundled microtubules is not dependent on 4RL-Tau to tubulin-dimer molar ratio SAXS profiles are of tubulin/tau/GTP mixtures at 37°C at standard buffer conditions with increasing Φ_{4RL} at t_0. Plots of fitted wall-to-wall distance ($d_{w\text{-}w}$) for the corresponding SAXS data highlight the lack of change in $d_{w\text{-}w}$ with increasing Φ_{4RL}. (Top) Azimuthally averaged synchrotron SAXS data (open circles) with decreasing Φ_{4RL}. SAXS scans are offset for clarity. The location of the (1,0) peak, $q_{1,0}$, which is used to measure the center-to-center distance between microtubules is not dependent on Φ_{4RL}. (Bottom) Plots of fitted wall-to-wall spacings ($d_{w\text{-}w}$) as a function of Φ_{4RL} of the SAXS data shown above.

References

1. S. L. Palay, C. Sotelo, A. Peters, P. M. Orkand, The axon hillock and the initial segment. *J Cell Biol* **38**, 193-201 (1968).

1 Desai, A. & Mitchison, T. J. Microtubule polymerization dynamics. *Annu Rev Cell Dev Biol* **13**, 83-117 (1997).
2 Chretien, D., Fuller, S. D. & Karsenti, E. Structure of growing microtubule ends: two-dimensional sheets close into tubes at variable rates. *J Cell Biol* **129**, 1311-1328 (1995).
3 Hyman, A. A., Chretien, D., Arnal, I. & Wade, R. H. Structural changes accompanying GTP hydrolysis in microtubules: information from a slowly hydrolyzable analogue guanylyl-(alpha,beta)-methylene-diphosphonate. *J Cell Biol* **128**, 117-125 (1995).
4 Muller-Reichert, T., Chretien, D., Severin, F. & Hyman, A. A. Structural changes at microtubule ends accompanying GTP hydrolysis: information from a slowly hydrolyzable analogue of GTP, guanylyl (alpha,beta)methylenediphosphonate. *Proc Natl Acad Sci U S A* **95**, 3661-3666 (1998).
5 Alushin, G. M. *et al.* High-resolution microtubule structures reveal the structural transitions in alphabeta-tubulin upon GTP hydrolysis. *Cell* **157**, 1117-1129 (2014). https://doi.org:10.1016/j.cell.2014.03.053
6 Best, R. L. *Mechanistic insights into the regulation of microtubule assembly and dynamic instability by tau and MMAE*, UC Santa Barbara, (2020).
7 Conde, C. & Caceres, A. Microtubule assembly, organization and dynamics in axons and dendrites. *Nat Rev Neurosci* **10**, 319-332 (2009). https://doi.org:10.1038/nrn2631
8 Melki, R., Carlier, M. F. & Pantaloni, D. Oscillations in microtubule polymerization: the rate of GTP regeneration on tubulin controls the period. *EMBO J* **7**, 2653-2659 (1988).
9 O'Brien, E. T., Voter, W. A. & Erickson, H. P. GTP hydrolysis during microtubule assembly. *Biochemistry* **26**, 4148-4156 (1987). https://doi.org:10.1021/bi00387a061
10 Jameson, L. & Caplow, M. Effect of guanosine diphosphate on microtubule assembly and stability. *J Biol Chem* **255**, 2284-2292 (1980).
11 Weisenberg, R. C., Borisy, G. G. & Taylor, E. W. The colchicine-binding protein of mammalian brain and its relation to microtubules. *Biochemistry* **7**, 4466-4479 (1968).
12 Nogales, E., Wolf, S. G. & Downing, K. H. Structure of the alpha beta tubulin dimer by electron crystallography. *Nature* **391**, 199-203 (1998).
13 Carlier, M. F., Didry, D. & Pantaloni, D. Hydrolysis of GTP associated with the formation of tubulin oligomers is involved in microtubule nucleation. *Biophys J* **73**, 418-427 (1997). https://doi.org:10.1016/S0006-3495(97)78081-0
14 Brouhard, G. J. & Rice, L. M. Microtubule dynamics: an interplay of biochemistry and mechanics. *Nature Reviews Molecular Cell Biology* **19**, 451-463 (2018). https://doi.org:10.1038/s41580-018-0009-y
15 Zeeberg, B. & Caplow, M. Determination of free and bound microtubular protein and guanine nucleotide under equilibrium conditions. *Biochemistry* **18**, 3880-3886 (1979). https://doi.org:10.1021/bi00585a007

16 Correia, J. J., Baty, L. T. & Williams, R. C. Mg2+ dependence of guanine nucleotide binding to tubulin. *J Biol Chem* **262**, 17278-17284 (1987).
17 Coombes, C. E., Yamamoto, A., Kenzie, M. R., Odde, D. J. & Gardner, M. K. Evolving tip structures can explain age-dependent microtubule catastrophe. *Curr Biol* **23**, 1342-1348 (2013). https://doi.org:10.1016/j.cub.2013.05.059
18 VanBuren, V., Cassimeris, L. & Odde, D. J. Mechanochemical model of microtubule structure and self-assembly kinetics. *Biophys J* **89**, 2911-2926 (2005). https://doi.org:10.1529/biophysj.105.060913
19 Zhang, R., Alushin, G. M., Brown, A. & Nogales, E. Mechanistic Origin of Microtubule Dynamic Instability and Its Modulation by EB Proteins. *Cell* **162**, 849-859 (2015). https://doi.org:10.1016/j.cell.2015.07.012
20 Ayukawa, R. *et al.* GTP-dependent formation of straight tubulin oligomers leads to microtubule nucleation. *J Cell Biol* **220** (2021). https://doi.org:10.1083/jcb.202007033
21 Zhang, R., LaFrance, B. & Nogales, E. Separating the effects of nucleotide and EB binding on microtubule structure. *Proc Natl Acad Sci U S A* **115**, E6191-e6200 (2018). https://doi.org:10.1073/pnas.1802637115
22 Mandelkow, E. M., Mandelkow, E. & Milligan, R. A. Microtubule dynamics and microtubule caps: a time-resolved cryo-electron microscopy study. *J Cell Biol* **114**, 977-991 (1991).
23 Simon, J. R. & Salmon, E. D. The structure of microtubule ends during the elongation and shortening phases of dynamic instability examined by negative-stain electron microscopy. *Journal of Cell Science* **96**, 571-582 (1990).
24 Shemesh, A. *et al.* Mechanism of the Initial Tubulin Nucleation Phase. *J Phys Chem Lett* **13**, 9725-9735 (2022). https://doi.org:10.1021/acs.jpclett.2c02619
25 Campanacci, V. *et al.* Insight into microtubule nucleation from tubulin-capping proteins. *Proc Natl Acad Sci U S A* **116**, 9859-9864 (2019). https://doi.org:10.1073/pnas.1813559116
26 Brugués, J., Nuzzo, V., Mazur, E. & Needleman, D. J. Nucleation and transport organize microtubules in metaphase spindles. *Cell* **149**, 554-564 (2012). https://doi.org:10.1016/j.cell.2012.03.027
27 Voter, W. A. & Erickson, H. P. The kinetics of microtubule assembly. Evidence for a two-stage nucleation mechanism. *J Biol Chem* **259**, 10430-10438 (1984).
28 Shemesh, A., Ginsburg, A., Levi-Kalisman, Y., Ringel, I. & Raviv, U. Structure, Assembly, and Disassembly of Tubulin Single Rings. *Biochemistry* **57**, 6153-6165 (2018). https://doi.org:10.1021/acs.biochem.8b00560
29 Shemesh, A. *et al.* Structure and Energetics of GTP- and GDP-Tubulin Isodesmic Self-Association. *ACS Chem Biol* **16**, 2212-2227 (2021). https://doi.org:10.1021/acschembio.1c00369
30 Fygenson, D. K., Braun, E. & Libchaber, A. Phase diagram of microtubules. *Phys Rev E Stat Phys Plasmas Fluids Relat Interdiscip Topics* **50**, 1579-1588 (1994).

31 Atherton, J. *et al.* A structural model for microtubule minus-end recognition and protection by CAMSAP proteins. *Nature Structural & Molecular Biology* **24**, 931-943 (2017). https://doi.org:10.1038/nsmb.3483
32 Erickson, H. P. Assembly of microtubules from preformed, ring-shaped protofilaments and 6-S tubulin. *J Supramol Struct* **2**, 393-411 (1974). https://doi.org:10.1002/jss.400020228
33 Janosi, I. M., Chretien, D. & Flyvbjerg, H. Modeling elastic properties of microtubule tips and walls. *Eur Biophys J* **27**, 501-513 (1998). https://doi.org:10.1007/s002490050160
34 Guesdon, A. *et al.* EB1 interacts with outwardly curved and straight regions of the microtubule lattice. *Nat Cell Biol* **18**, 1102-1108 (2016). https://doi.org:10.1038/ncb3412
35 Wang, H. W., Long, S., Finley, K. R. & Nogales, E. Assembly of GMPCPP-bound tubulin into helical ribbons and tubes and effect of colchicine. *Cell Cycle* **4**, 1157-1160 (2005). https://doi.org:10.4161/cc.4.9.2042
36 Gardner, M. K. *et al.* Rapid microtubule self-assembly kinetics. *Cell* **146**, 582-592 (2011). https://doi.org:10.1016/j.cell.2011.06.053
37 McIntosh, J. R. *et al.* Microtubules grow by the addition of bent guanosine triphosphate tubulin to the tips of curved protofilaments. *Journal of Cell Biology* **217**, 2691-2708 (2018). https://doi.org:10.1083/jcb.201802138
38 Diaz, J. F., Andreu, J. M., Diakun, G., Towns-Andrews, E. & Bordas, J. Structural intermediates in the assembly of taxoid-induced microtubules and GDP-tubulin double rings: time-resolved X-ray scattering. *Biophys J* **70**, 2408-2420 (1996). https://doi.org:10.1016/S0006-3495(96)79809-0
39 Spann, U., Renner, W., Mandelkow, E. M., Bordas, J. & Mandelkow, E. Tubulin oligomers and microtubule assembly studied by time-resolved X-ray scattering: separation of prenucleation and nucleation events. *Biochemistry* **26**, 1123-1132 (1987). https://doi.org:10.1021/bi00378a021
40 Nogales, E., Wang, H.-W. & Niederstrasser, H. Tubulin rings: which way do they curve? *Current Opinion in Structural Biology* **13**, 256-261 (2003). https://doi.org:https://doi.org/10.1016/S0959-440X(03)00029-0
41 Howard, W. D. & Timasheff, S. N. GDP state of tubulin: stabilization of double rings. *Biochemistry* **25**, 8292-8300 (1986). https://doi.org:10.1021/bi00373a025
42 Weisenberg, R. C., Deery, W. J. & Dickinson, P. J. Tubulin-nucleotide interactions during the polymerization and depolymerization of microtubules. *Biochemistry* **15**, 4248-4254 (1976). https://doi.org:10.1021/bi00664a018
43 Nicholson, W. V., Lee, M., Downing, K. H. & Nogales, E. Cryo-electron microscopy of GDP-tubulin rings. *Cell Biochem Biophys* **31**, 175-183 (1999). https://doi.org:10.1007/bf02738171
44 Borisy, G. G. & Olmsted, J. B. Nucleated assembly of microtubules in porcine brain extracts. *Science* **177**, 1196-1197 (1972). https://doi.org:10.1126/science.177.4055.1196

45 Weisenberg, R. C. Microtubule formation in vitro in solutions containing low calcium concentrations. *Science* **177**, 1104-1105 (1972). https://doi.org:10.1126/science.177.4054.1104
46 Gal, V., Martin, S. & Bayley, P. Fast disassembly of microtubules induced by Mg2+ or Ca2+. *Biochem Biophys Res Commun* **155**, 1464-1470 (1988). https://doi.org:10.1016/s0006-291x(88)81306-8
47 O'Brien, E. T., Salmon, E. D., Walker, R. A. & Erickson, H. P. Effects of magnesium on the dynamic instability of individual microtubules. *Biochemistry* **29**, 6648-6656 (1990). https://doi.org:10.1021/bi00480a014
48 Frigon, R. P. & Timasheff, S. N. Magnesium-induced self-association of calf brain tubulin. I. Stoichiometry. *Biochemistry* **14**, 4559-4566 (1975). https://doi.org:10.1021/bi00692a001
49 Nogales, E., Wolf, S. G., Khan, I. A., Luduena, R. F. & Downing, K. H. Structure of tubulin at 6.5 A and location of the taxol-binding site. *Nature* **375**, 424-427 (1995).
50 Jordan, M. A. & Wilson, L. Microtubules as a target for anticancer drugs. *Nat Rev Cancer* **4**, 253-265 (2004).
51 Elie-Caille, C. *et al.* Straight GDP-Tubulin Protofilaments Form in the Presence of Taxol. *Current Biology* **17**, 1765-1770 (2007). https://doi.org:10.1016/j.cub.2007.08.063
52 Choi, M. C. *et al.* Human microtubule-associated-protein tau regulates the number of protofilaments in microtubules: a synchrotron x-ray scattering study. *Biophys J* **97**, 519-527 (2009). https://doi.org:S0006-3495(09)00953-9 [pii] 10.1016/j.bpj.2009.04.047
53 Goedert, M., Spillantini, M. G., Jakes, R., Rutherford, D. & Crowther, R. A. Multiple isoforms of human microtubule-associated protein tau: sequences and localization in neurofibrillary tangles of Alzheimer's disease. *Neuron* **3**, 519-526 (1989).
54 Himmler, A. Structure of the bovine tau gene: alternatively spliced transcripts generate a protein family. *Mol Cell Biol* **9**, 1389-1396 (1989).
55 Goedert, M. & Jakes, R. Expression of separate isoforms of human tau protein: correlation with the tau pattern in brain and effects on tubulin polymerization. *Embo J* **9**, 4225-4230 (1990).
56 Panda, D., Samuel, J. C., Massie, M., Feinstein, S. C. & Wilson, L. Differential regulation of microtubule dynamics by three- and four-repeat tau: implications for the onset of neurodegenerative disease. *Proc Natl Acad Sci U S A* **100**, 9548-9553 (2003). https://doi.org:10.1073/pnas.1633508100
57 Drechsel, D. N., Hyman, A. A., Cobb, M. H. & Kirschner, M. W. Modulation of the dynamic instability of tubulin assembly by the microtubule-associated protein tau. *Mol Biol Cell* **3**, 1141-1154 (1992).
58 Panda, D., Goode, B. L., Feinstein, S. C. & Wilson, L. Kinetic stabilization of microtubule dynamics at steady state by tau and microtubule-binding domains of tau. *Biochemistry* **34**, 11117-11127 (1995).

59 Bunker, J. M., Wilson, L., Jordan, M. A. & Feinstein, S. C. Modulation of microtubule dynamics by tau in living cells: implications for development and neurodegeneration. *Mol Biol Cell* **15**, 2720-2728 (2004).
60 Trinczek, B., Biernat, J., Baumann, K., Mandelkow, E. M. & Mandelkow, E. Domains of tau protein, differential phosphorylation, and dynamic instability of microtubules. *Mol Biol Cell* **6**, 1887-1902 (1995).
61 Qiang, L. *et al.* Tau Does Not Stabilize Axonal Microtubules but Rather Enables Them to Have Long Labile Domains. *Current Biology* **28**, 2181-2189.e2184 (2018). https://doi.org:https://doi.org/10.1016/j.cub.2018.05.045
62 Best, R. L. *et al.* Tau isoform-specific stabilization of intermediate states during microtubule assembly and disassembly. *J Biol Chem* **294**, 12265-12280 (2019). https://doi.org:10.1074/jbc.RA119.009124
63 Samsonov. Tau interaction with microtubules in vivo. *Journal of Cell Science* (2004).
64 Breuzard, G. *et al.* Molecular mechanisms of Tau binding to microtubules and its role in microtubule dynamics in live cells. *J Cell Sci* **126**, 2810-2819 (2013). https://doi.org:10.1242/jcs.120832
65 Tan, R. *et al.* Microtubules gate tau condensation to spatially regulate microtubule functions. *Nat Cell Biol* **21**, 1078-1085 (2019). https://doi.org:10.1038/s41556-019-0375-5
66 Duan, A. R. *et al.* Interactions between Tau and Different Conformations of Tubulin: Implications for Tau Function and Mechanism. *J Mol Biol* **429**, 1424-1438 (2017). https://doi.org:10.1016/j.jmb.2017.03.018
67 Kirschner, M. W., Williams, R. C., Weingarten, M. & Gerhart, J. C. Microtubules from mammalian brain: some properties of their depolymerization products and a proposed mechanism of assembly and disassembly. *Proc Natl Acad Sci U S A* **71**, 1159-1163 (1974).
68 Castle, B. T., McKibben, K. M., Rhoades, E. & Odde, D. J. Tau avoids the GTP cap at growing microtubule plus ends. *bioRxiv*, 2019.2012.2031.891234 (2020). https://doi.org:10.1101/2019.12.31.891234
69 Drubin, D. G., Feinstein, S. C., Shooter, E. M. & Kirschner, M. W. Nerve growth factor-induced neurite outgrowth in PC12 cells involves the coordinate induction of microtubule assembly and assembly-promoting factors. *J Cell Biol* **101**, 1799-1807 (1985).
70 Drubin, D., Kobayashi, S. & Kirschner, M. Association of tau protein with microtubules in living cells. *Ann N Y Acad Sci* **466**, 257-268 (1986).
71 Sato-Harada, R., Okabe, S., Umeyama, T., Kanai, Y. & Hirokawa, N. Microtubule-associated proteins regulate microtubule function as the track for intracellular membrane organelle transports. *Cell Struct Funct* **21**, 283-295 (1996).
72 Caceres, A. & Kosik, K. S. Inhibition of neurite polarity by tau antisense oligonucleotides in primary cerebellar neurons. *Nature* **343**, 461-463 (1990).

73 Caceres, A., Potrebic, S. & Kosik, K. S. The effect of tau antisense oligonucleotides on neurite formation of cultured cerebellar macroneurons. *J Neurosci* **11**, 1515-1523 (1991).
74 Li, X. *et al.* Novel diffusion barrier for axonal retention of Tau in neurons and its failure in neurodegeneration. *EMBO J* **30**, 4825-4837 (2011). https://doi.org:10.1038/emboj.2011.376
75 Kempf, M., Clement, A., Faissner, A., Lee, G. & Brandt, R. Tau binds to the distal axon early in development of polarity in a microtubule- and microfilament-dependent manner. *J Neurosci* **16**, 5583-5592 (1996).
76 Xia, D., Gutmann, J. M. & Götz, J. Mobility and subcellular localization of endogenous, gene-edited Tau differs from that of over-expressed human wild-type and P301L mutant Tau. *Sci Rep* **6**, 29074 (2016). https://doi.org:10.1038/srep29074
77 Palay, S. L., Sotelo, C., Peters, A. & Orkand, P. M. The axon hillock and the initial segment. *J Cell Biol* **38**, 193-201 (1968). https://doi.org:10.1083/jcb.38.1.193
78 Peters, A., Palay, S. L. & Webster, H. d. F. (Oxford University Press, 1991).
79 Rasband, M. N. The axon initial segment and the maintenance of neuronal polarity. *Nat Rev Neurosci* **11**, 552-562 (2010). https://doi.org:10.1038/nrn2852
80 Frappier, T. F., Georgieff, I. S., Brown, K. & Shelanski, M. L. tau Regulation of microtubule-microtubule spacing and bundling. *J Neurochem* **63**, 2288-2294 (1994).
81 Chen, J., Kanai, Y., Cowan, N. J. & Hirokawa, N. Projection domains of MAP2 and tau determine spacings between microtubules in dendrites and axons. *Nature* **360**, 674-677 (1992). https://doi.org:10.1038/360674a0
82 Chung, P. J. *et al.* Tau mediates microtubule bundle architectures mimicking fascicles of microtubules found in the axon initial segment. *Nat Commun* **7**, 12278 (2016). https://doi.org:10.1038/ncomms12278
83 Gustke, N., Trinczek, B., Biernat, J., Mandelkow, E. M. & Mandelkow, E. Domains of Tau-Protein and Interactions with Microtubules. *Biochemistry* **33**, 9511-9522 (1994).
84 Brandt, R. & Lee, G. Orientation, assembly, and stability of microtubule bundles induced by a fragment of tau protein. *Cell Motil Cytoskeleton* **28**, 143-154 (1994).
85 Hirokawa, N., Hisanaga, S. & Shiomura, Y. MAP2 is a component of crossbridges between microtubules and neurofilaments in the neuronal cytoskeleton: quick-freeze, deep-etch immunoelectron microscopy and reconstitution studies. *J Neurosci* **8**, 2769-2779 (1988).
86 Rosenberg, K. J., Ross, J. L., Feinstein, H. E., Feinstein, S. C. & Israelachvili, J. Complementary dimerization of microtubule-associated tau protein: Implications for microtubule bundling and tau-mediated pathogenesis. *Proc Natl Acad Sci U S A* **105**, 7445-7450 (2008). https://doi.org:10.1073/pnas.0802036105

87 Harada, A. *et al.* Altered microtubule organization in small-calibre axons of mice lacking tau protein. *Nature* **369**, 488-491 (1994).
88 Kanai, Y., Chen, J. & Hirokawa, N. Microtubule bundling by tau proteins in vivo: analysis of functional domains. *Embo J* **11**, 3953-3961 (1992).
89 Rubinstein, M. & Colby, R. H. *Polymer physics*. Vol. 23 (Oxford university press New York, 2003).
90 Mylonas, E. *et al.* Domain conformation of tau protein studied by solution small-angle X-ray scattering. *Biochemistry* **47**, 10345-10353 (2008). https://doi.org:10.1021/bi800900d
91 Chung, P. J. *et al.* Direct force measurements reveal that protein Tau confers short-range attractions and isoform-dependent steric stabilization to microtubules. *Proc Natl Acad Sci U S A* **112**, E6416-6425 (2015). https://doi.org:10.1073/pnas.1513172112
92 Choi, M. C. *et al.* Paclitaxel suppresses Tau-mediated microtubule bundling in a concentration-dependent manner. *Biochim Biophys Acta Gen Subj* **1861**, 3456-3463 (2017). https://doi.org:10.1016/j.bbagen.2016.09.011
93 Lee, V. M., Goedert, M. & Trojanowski, J. Q. Neurodegenerative tauopathies. *Annual Review of Neuroscience* **24**, 1121-1159 (2001).
94 Brunden, K. R., Trojanowski, J. Q. & Lee, V. M. Advances in tau-focused drug discovery for Alzheimer's disease and related tauopathies. *Nature Reviews Drug Discovery* **8**, 783-793 (2009). https://doi.org:nrd2959 [pii] 10.1038/nrd2959
95 Brunden, K. R. *et al.* Epothilone D improves microtubule density, axonal integrity, and cognition in a transgenic mouse model of tauopathy. *J Neurosci* **30**, 13861-13866 (2010). https://doi.org:10.1523/jneurosci.3059-10.2010
96 Vossel, K. A. *et al.* Tau reduction prevents Abeta-induced defects in axonal transport. *Science* **330**, 198 (2010). https://doi.org:10.1126/science.1194653
97 Vossel, K. A. *et al.* Tau reduction prevents Abeta-induced axonal transport deficits by blocking activation of GSK3beta. *J Cell Biol* **209**, 419-433 (2015). https://doi.org:10.1083/jcb.201407065
98 Zempel, H. & Mandelkow, E. Mechanisms of Axonal Sorting of Tau and Influence of the Axon Initial Segment on Tau Cell Polarity. *Adv Exp Med Biol* **1184**, 69-77 (2019). https://doi.org:10.1007/978-981-32-9358-8_6
99 Zempel, H. & Mandelkow, E. Lost after translation: missorting of Tau protein and consequences for Alzheimer disease. *Trends Neurosci* **37**, 721-732 (2014). https://doi.org:10.1016/j.tins.2014.08.004
100 Best, R. L. *et al.* Expression and isolation of recombinant tau. *Methods Cell Biol* **141**, 3-26 (2017). https://doi.org:10.1016/bs.mcb.2017.06.001
101 Needleman, D. J. *et al.* Synchrotron X-ray diffraction study of microtubules buckling and bundling under osmotic stress: a probe of interprotofilament interactions. *Phys Rev Lett* **93**, 198104 (2004).

102 Raviv, U. *et al.* Microtubule protofilament number is modulated in a stepwise fashion by the charge density of an enveloping layer. *Biophys J* **92**, 278-287 (2007). https://doi.org:10.1529/biophysj.106.087478
103 Raviv, U. *et al.* Cationic liposome-microtubule complexes: pathways to the formation of two-state lipid-protein nanotubes with open or closed ends. *Proc Natl Acad Sci U S A* **102**, 11167-11172 (2005). https://doi.org:10.1073/pnas.0502183102
104 Inoue, S. & Salmon, E. D. Force generation by microtubule assembly/disassembly in mitosis and related movements. *Mol Biol Cell* **6**, 1619-1640 (1995).
105 Tanaka, E. M. & Kirschner, M. W. Microtubule behavior in the growth cones of living neurons during axon elongation. *J Cell Biol* **115**, 345-363 (1991).
106 Tanaka, E., Ho, T. & Kirschner, M. W. The role of microtubule dynamics in growth cone motility and axonal growth. *J Cell Biol* **128**, 139-155 (1995).
107 Nakata, T. & Hirokawa, N. Microtubules provide directional cues for polarized axonal transport through interaction with kinesin motor head. *J Cell Biol* **162**, 1045-1055 (2003).